

# Frozen-RANS Turbulence Model Corrections for Wind Turbine Wakes in Stable, Neutral and Unstable Atmospheric Boundary Layers

Master of Science Thesis

L.M. Kokee



# Frozen-RANS Turbulence Model Corrections for Wind Turbine Wakes in Stable, Neutral and Unstable Atmospheric Boundary Layers

Master of Science Thesis

by

L.M. Koike

to obtain the degree of Master of Science in Aerospace Engineering at the Delft University of Technology and Master of Science in Engineering (European Wind Energy) at the Technical University of Denmark, to be defended publicly on Thursday, August 30, 2021 at 10:00 AM.

Student number: 4466268  
Project duration: November, 2020 - July, 2021  
Supervisors: Dr. H. Sarlak, DTU  
Dr. R.P. Dwight, TU Delft  
Ir. J. Steiner, TU Delft

An electronic version of this thesis is available at <http://repository.tudelft.nl/>.



# Abstract

Computational Fluid Dynamics (CFD) based on RANS models remain the standard but suffer from high errors in complex flows. In particular, turbulent kinetic energy is over-produced in high strain rate regions, such as the near-wake of wind turbine flows. Data-driven turbulence modelling methods aim to derive novel turbulence models with lower uncertainties, which generalize well to a certain class of flows. The state-of-the-art constitutes to first derive model-form corrections of a selected baseline model from high fidelity reference data, followed by regressing the corrections in terms of RANS-known flow features. For data-driven wind turbine wake modelling, industrial-scale wind turbines and non-neutral atmospheric boundary layers have yet to be considered. In this thesis, the first steps are made to address this research gap.

First, Large-Eddy Simulation (LES) data is generated and validated against literature. The considered cases are under neutral, convective and stable atmospheric conditions. The frozen-RANS methodology, a technique used to derive turbulence model corrections given the high fidelity data, is then extended to non-neutral conditions. The new framework now provides corrections to both the Boussinesq eddy viscosity hypothesis for the Reynolds stress and the gradient-diffusion hypothesis for the turbulent heat flux.

By injecting the obtained corrections into dynamic Reynolds-Averaged Navier-Stokes (RANS) simulations, the baseline turbulence model deficiencies are corrected. In particular, high rate-of-strain regions now no longer show an overproduction of mechanical turbulence. Similarly, the lack of buoyant turbulence production in the free-stream atmosphere under convective conditions is solved. In the stable case, too large values of buoyant destruction in the free-stream and buoyant production in the wake are adequately corrected for. For the neutral and stable case, the corrected models produce wake velocity profiles that show excellent agreement with the LES reference data. Issues in the wall stress solution of the convective LES propagate to issues in the corrected RANS solutions, proving the necessity of high-quality data. Furthermore, it is shown that for most cases a single scalar correction to the turbulent heat flux, as opposed to the full vector correction, is sufficient for improving the error introduced by the gradient-diffusion hypothesis. This result is considerable since the simpler correction would be much easier to regress in terms of mean RANS-known quantities. The computational cost of the corrected RANS models is around the same as that of baseline RANS models; only 2%-5% of the LES computational cost.

# Preface

This thesis is the final deliverable that marks the completion of the European Wind Energy Master. The past two years have been incredibly eventful: moving to Denmark to start a new adventure, moving house during the midst of a pandemic and, of course diving deep into the subject matter in this thesis. Although I am excited to tackle new challenges, I will cherish the memories I have gained during this master and during this thesis.

I would like to thank my supervisors Richard, Julia and Hamid, for their support. Their guidance has helped me navigate, for the first time, the scientific landscape. Additionally, they have provided me with invaluable support in solving the many technical problems I encountered throughout the entire period of the thesis. I would also like to thank my family, friends and the ones close to me for continually providing me support and helping me become who I am today.

*L.M. Kokee  
Copenhagen, July 2021*

# Contents

<b>List of Figures</b>	<b>vii</b>
<b>List of Tables</b>	<b>x</b>
<b>Nomenclature</b>	<b>xi</b>
<b>1 Introduction</b>	<b>1</b>
1.1 Background . . . . .	1
1.2 Research Questions . . . . .	2
1.3 Research Objectives . . . . .	2
1.4 Report Structure . . . . .	3
<b>2 The Atmospheric Boundary Layer and Wind Turbine Flows</b>	<b>4</b>
2.1 Driving Forces in the Atmosphere . . . . .	4
2.2 Atmospheric Stability . . . . .	5
2.3 Monin-Obukhov Similarity . . . . .	6
2.4 Wind Turbines and Wakes . . . . .	7
<b>3 Computational Fluid Dynamics and Turbulence Modelling</b>	<b>10</b>
3.1 Direct Numerical Simulation . . . . .	10
3.2 Large Eddy Simulation . . . . .	11
3.3 Reynolds-Averaged Navier-Stokes . . . . .	11
3.3.1 $k - \epsilon$ Model . . . . .	12
3.3.2 Improvements to the $k - \epsilon$ and $k - \omega$ Models . . . . .	13
3.3.3 Non-Linear Eddy-Viscosity Models . . . . .	14
3.3.4 Reynolds Stress Models . . . . .	14
3.3.5 Scalar Flux Models . . . . .	14
3.3.6 Non-Neutral Atmospheres . . . . .	15
3.4 Turbine Modelling in CFD . . . . .	15
3.5 Data-Driven Turbulence Modelling . . . . .	16
3.5.1 Statistical Inference and Uncertainty Quantification . . . . .	16
3.5.2 Machine Learning . . . . .	17
<b>4 Methodology</b>	<b>21</b>
4.1 Large-Eddy Simulations . . . . .	21
4.1.1 Case Definitions . . . . .	21
4.1.2 Governing Equations . . . . .	21
4.1.3 Numerical Schemes . . . . .	22
4.1.4 Precursor-Successor Approach . . . . .	22
4.1.5 Initial Conditions . . . . .	23
4.1.6 Boundary Conditions . . . . .	24
4.1.7 Turbine Representation . . . . .	27
4.1.8 Domain and Mesh . . . . .	27
4.2 Frozen-RANS . . . . .	27
4.2.1 Baseline $k - \epsilon$ model . . . . .	27
4.2.2 Postulation of model-form error . . . . .	28
4.2.3 Algorithm Description . . . . .	29
4.2.4 Numerical Schemes . . . . .	29
4.2.5 Boundary Conditions . . . . .	29

4.2.6	Consistency with LES System . . . . .	30
4.3	Corrected RANS . . . . .	31
4.3.1	Governing and Model Equations . . . . .	31
4.3.2	Momentum Forcing . . . . .	32
4.3.3	Initial and Boundary Conditions . . . . .	32
<b>5</b>	<b>Large-Eddy Simulation Results</b>	<b>34</b>
5.1	Validation Case 1: GABLS . . . . .	34
5.2	Validation Case 2: Abkar & Moin Convective Planetary Boundary Layer . . . . .	37
5.3	Validation Case 3: Rough Wall Atmospheric Log-Law . . . . .	39
5.4	Main Case Results . . . . .	40
5.4.1	Neutral Boundary Layer . . . . .	40
5.4.2	Stable Boundary Layer . . . . .	41
5.4.3	Convective Boundary Layer . . . . .	43
5.5	Averaging Period Sensitivity Study . . . . .	44
<b>6</b>	<b>Frozen-RANS Results</b>	<b>49</b>
6.1	Neutral Boundary Layer . . . . .	49
6.2	Stable Boundary Layer . . . . .	50
6.2.1	$k - \epsilon$ Model-Form Errors . . . . .	50
6.2.2	Gradient-Diffusion Hypothesis Error . . . . .	50
6.3	Convective Boundary Layer . . . . .	52
6.3.1	$k - \epsilon$ Model-Form Errors . . . . .	52
6.3.2	Gradient-Diffusion Hypothesis Error . . . . .	53
<b>7</b>	<b>Corrected RANS</b>	<b>57</b>
7.1	Neutral Boundary Layer . . . . .	57
7.1.1	Free-Stream Flow . . . . .	57
7.1.2	Wind Turbine Flow . . . . .	57
7.2	Stable Boundary Layer . . . . .	60
7.2.1	Free-Stream Flow . . . . .	60
7.2.2	Wind Turbine Flow . . . . .	61
7.3	Convective Boundary Layer . . . . .	63
7.3.1	Free-Stream Flow . . . . .	64
7.3.2	Wind Turbine Flow . . . . .	64
7.4	Averaging Period Effect . . . . .	70
7.5	Computational Cost . . . . .	72
7.6	Discussion . . . . .	73
<b>8</b>	<b>Conclusions and Recommendation</b>	<b>75</b>
8.1	Conclusions . . . . .	75
8.2	Recommendations . . . . .	77
	<b>Appendices</b>	<b>84</b>
<b>A</b>	<b>LES Successor Results</b>	<b>85</b>
A.1	Neutral Boundary Layer Case . . . . .	85
A.2	Stable Boundary Layer Case . . . . .	86
A.3	Convective Boundary Layer Case . . . . .	87
A.3.1	Averaging Period 1 Hour . . . . .	87
A.3.2	Averaging Period 5 Hours . . . . .	87



# List of Figures

2.1	Idealized weather maps for the northern hemisphere showing theoretical steady-state winds. Figure taken from Stull [20]. . . . .	5
2.2	Thermo-diagram for a simplified unstable atmosphere. The rising parcel is compared to its environment in temperature (left) and potential temperature (right). Figure from [20]. . . . .	6
2.3	Typical velocity profiles for the unstable, stable and neutral boundary layer. The figure is taken and adapted from Stull [20]. . . . .	7
2.4	Schematic of the resultant force acting on the blade element and the decomposed forces. Figure obtained from Porté-Agel, Wu, Lu, <i>et al.</i> [26]. . . . .	8
2.5	Schematic of the wake and its distinct regions. Figure obtained from Porté-Agel, Bastankhah, and Shamsoddin [28]. . . . .	9
2.6	Velocity and potential temperature contours from LES for very stable conditions (left plots) and unstable conditions (right plots). Figure obtained from Machefaux, Larsen, Koblitz, <i>et al.</i> [17]. . . . .	9
3.1	Technical flowchart of the SpaRTA (Sparse Regression of Turbulent Stress Anisotropy) methodology. Figure taken from Schmelzer, Dwight, and Cinnella [13]. . . . .	18
3.2	Two numerical solutions . . . . .	19
4.1	Schematic of the precursor-successor approach to providing inflow conditions for wind turbine flows. The figure is obtained from Matthew J. Churchfield, Lee, Michalakes, <i>et al.</i> [83]. . . . .	23
4.2	Initial conditions for the potential temperature $\theta$ for the CBL case (left) and the SBL case (right) . . . . .	24
4.3	Flowchart for the Frozen-RANS method to computing model-form errors . . . . .	30
5.1	Stable boundary layer case validation results. Left: $U$ (solid) and $V$ (dashed) components of velocity. Right: temperature distribution. Thin black lines represent the GABLS data. . . . .	34
5.2	Stable boundary layer case validation results for the Resolved Reynolds stress components. Thin black lines represent the GABLS data. . . . .	35
5.3	Stable boundary layer case validation results for the Resolved heat flux components. Thin black lines represent the GABLS data. . . . .	35
5.4	Stable boundary layer case validation results for the Vertical momentum flux decomposed into the Resolved and SGS components. Thin black lines represent the GABLS data. . . . .	36
5.5	Convective boundary layer case validation result. Left: Planar averages of mean $U$ (solid) and $V$ (dashed) components of velocity. Right: Planar average of mean potential temperature distribution. . . . .	37
5.6	Convective boundary layer case validation results for the planar averages of the horizontal (left) and vertical (right) resolved stresses, compared to field aircraft observations. . . . .	37
5.7	Convective boundary layer case validation results for the planar averages of the vertical momentum flux decomposed into the Resolved and SGS components. . . . .	38
5.8	Convective boundary layer case validation results for planar averages of the vertical heat flux decomposed into the Resolved and SGS components. . . . .	38
5.9	Neutral boundary layer case horizontal velocity planar averages compared to the rough wall ABL log-law . . . . .	39
5.10	Neutral boundary layer case convergence based on friction velocity $u_*$ time series . . . . .	40
5.11	Neutral boundary layer velocity profiles in the induction region . . . . .	41
5.12	Neutral boundary layer velocity and velocity deficit profiles in the wake . . . . .	41
5.13	Stable boundary layer case convergence based on friction velocity $u_*$ time series . . . . .	42
5.14	Stable boundary layer case wall heat flux $q_w$ time series . . . . .	42
5.15	Stable boundary layer induction region velocity profiles . . . . .	42
5.16	Stable boundary layer velocity and velocity deficit profiles in the wake . . . . .	43
5.17	Convective boundary layer case convergence based on friction velocity $u_*$ time series . . . . .	43
5.18	Convective boundary layer precursor Reynolds stress components . . . . .	44

5.19	CBL case precursor turbulent kinetic energy . . . . .	44
5.20	Convective boundary layer induction region velocity profiles . . . . .	44
5.21	Convective boundary layer velocity and velocity deficit profiles in the wake . . . . .	45
5.22	Sensitivity of wake velocity deficit profiles to the time averaging period for the CBL case . . . . .	45
5.23	Sensitivity of wake turbulent kinetic energy profiles to the time averaging period for the CBL case . . . . .	46
5.24	Sensitivity of wake potential temperature profiles to the time averaging period for the CBL case . . . . .	46
5.25	Sensitivity of wake wall-normal turbulent heat-flux profiles to the time averaging period for the CBL case . . . . .	47
5.26	Monin-Obukhov length time series for the convective boundary layer case with $T_{avg} = 5 h$ . . . . .	47
6.1	Frozen-RANS results for the NBL precursor case showing the normalized anisotropy error . . . . .	50
6.2	Frozen-RANS results for the NBL precursor case . . . . .	51
6.3	Contours of frozen-RANS corrections for NBL wind turbine flow, plotted at $-1 \leq x/D \leq 9$ relative to the turbine . . . . .	51
6.4	Frozen-RANS results for the SBL precursor case showing the normalized anisotropy error . . . . .	52
6.5	Frozen-RANS results for the CBL precursor case . . . . .	52
6.6	Contours of frozen-RANS corrections for SBL wind turbine flow, plotted at $-1 \leq x/D \leq 9$ relative to the turbine . . . . .	53
6.7	Frozen-RANS results for the SBL free-stream flow showing the turbulent heat flux error . . . . .	53
6.8	Frozen-RANS results for the SBL free-stream flow showing various effects of the turbulence heat flux error . . . . .	54
6.9	Frozen-RANS results for the SBL wind turbine flow showing buoyant turbulence production error, plotted at $-1 \leq x/D \leq 9$ relative to the turbine . . . . .	54
6.10	Frozen-RANS results for the CBL precursor case showing the normalized anisotropy error . . . . .	54
6.11	Frozen-RANS results for the CBL precursor case . . . . .	55
6.12	Contours of frozen-RANS corrections for CBL wind turbine flow, plotted at $-1 \leq x/D \leq 9$ relative to the turbine . . . . .	55
6.13	Frozen-RANS results for the CBL precursor case showing the turbulent heat flux error . . . . .	56
6.14	Frozen-RANS results showing various effects of the turbulence heat flux error, plotted at $-1 \leq x/D \leq 9$ relative to the turbine . . . . .	56
6.15	Frozen-RANS results for the CBL successor case showing buoyant turbulence production error . . . . .	56
7.1	Free-stream CBL corrected RANS profiles compared to the baseline and to LES . . . . .	57
7.2	Corrected RANS Reynolds stress results for the free-stream NBL case . . . . .	58
7.3	Corrected RANS wake velocity deficit profiles for the NBL case . . . . .	58
7.4	Corrected RANS horizontal wake turbulent kinetic energy profiles for the NBL case . . . . .	59
7.5	Corrected RANS velocity results for the free-stream SBL case . . . . .	60
7.6	Free-stream SBL corrected RANS profiles compared to the baseline and to LES . . . . .	60
7.7	Corrected RANS Reynolds stress results for the free-stream SBL case . . . . .	61
7.8	Corrected RANS turbulent heat flux results for the free-stream SBL case . . . . .	61
7.9	Corrected RANS wake velocity deficit profiles for the SBL case . . . . .	62
7.10	Corrected RANS wake turbulent kinetic energy profiles for the SBL case . . . . .	62
7.11	Corrected RANS wake Reynolds stress $xz$ -component profiles for the SBL case . . . . .	63
7.12	Corrected RANS wake potential temperature profiles for the SBL case . . . . .	63
7.13	Corrected RANS wake wall-normal heat flux profiles for the SBL case . . . . .	64
7.14	Corrected RANS velocity results for the free-stream CBL case . . . . .	65
7.15	Free-stream CBL corrected RANS profiles compared to the baseline and to LES . . . . .	65
7.16	Corrected RANS Reynolds stress results for the free-stream CBL case . . . . .	66
7.17	Corrected RANS turbulent heat flux results for the free-stream CBL case . . . . .	66
7.18	Corrected RANS wake velocity deficit profiles for the CBL case . . . . .	67
7.19	Corrected RANS wake turbulent kinetic energy profiles for the CBL case . . . . .	67
7.20	Corrected RANS wake Reynolds stress $xz$ -component profiles for the CBL case . . . . .	68
7.21	Corrected RANS wake wall-normal turbulent heat flux profiles for the CBL case . . . . .	68
7.22	Corrected RANS wake potential temperature profiles for the CBL case . . . . .	69
7.23	Corrected RANS wake eddy viscosity for the CBL case, compared to the frozen case eddy viscosity . . . . .	69
7.24	Corrected RANS wake velocity deficit profiles for the CBL case using a five-hour averaging period . . . . .	70
7.25	Corrected RANS wake turbulent kinetic energy profiles for the CBL case using a five-hour averaging period . . . . .	71
7.26	Corrected RANS wake wall-normal turbulent heat flux profiles for the CBL case using a five-hour averaging period . . . . .	71
7.27	NBL case RANS residuals for the corrections applied right from simulation start (instant), gradually over 100 iterations (100 It) and for the baseline $k - \epsilon$ model (baseline) . . . . .	72

A.1	Neutral boundary layer velocity and velocity deficit profiles in the wake . . . . .	85
A.2	Neutral boundary layer wake TKE profiles . . . . .	85
A.3	Stable boundary layer velocity and velocity deficit profiles in the wake . . . . .	86
A.4	Stable boundary layer wake TKE profiles . . . . .	86
A.5	Stable boundary layer vertical wake heat-flux profiles . . . . .	86
A.6	Stable boundary layer horizontal wake heat-flux profiles . . . . .	87
A.7	Convective boundary layer velocity and velocity deficit profiles in the wake obtained with $T_{avg} = 1 h$ .	87
A.8	Convective boundary layer wake TKE profiles obtained with $T_{avg} = 1 h$ . . . . .	88
A.9	Convective boundary layer vertical wake heat-flux profiles . . . . .	88
A.10	Convective boundary layer horizontal wake heat-flux profiles obtained with $T_{avg} = 1 h$ . . . . .	88
A.11	Convective boundary layer velocity and velocity deficit profiles in the wake obtained with $T_{avg} = 5 h$ .	89
A.12	Convective boundary layer wake TKE profiles obtained with $T_{avg} = 5 h$ . . . . .	89
A.13	Convective boundary layer vertical wake heat-flux profiles obtained with $T_{avg} = 5 h$ . . . . .	89
A.14	Convective boundary layer horizontal wake heat-flux profiles obtained with $T_{avg} = 5 h$ . . . . .	90

# List of Tables

2.1	Atmospheric stability classes, as defined by the Monin-Obukhov Length. Table obtained from Peña, Gryning, and Mann [21]. . . . .	6
2.2	Empirically determined coefficients of the Monin-Obukhov functions . . . . .	8
4.1	General parameters and conditions used in the LES cases . . . . .	21
4.2	Finite volume schemes for LES solver . . . . .	22
4.3	Boundary conditions of the LES precursor cases under neutral (N), stable (S) and unstable (U) conditions	25
4.4	Boundary conditions of the LES successor cases under neutral (N), stable (S) and unstable (U) conditions	26
4.5	Domain size $L_x \cdot L_y \cdot L_z$ for the LES precursor and successor stages . . . . .	27
4.6	Mesh resolution and refinement zones for the CBL precursor case . . . . .	27
4.7	Standard model coefficients for the selected $k - \epsilon$ ABL model, under neutral, stable and unstable conditions . . . . .	28
4.8	Finite volume schemes for RANS and frozen-RANS solvers . . . . .	29
4.9	Boundary conditions for the Frozen-RANS cases . . . . .	31
4.10	LES friction velocity and wall turbulent kinetic energy . . . . .	31
4.11	$k - \epsilon$ model coefficients that ensure consistency with the LES reference for the NBL case, SBL and CBL case . . . . .	31
4.12	Mean LES rotor revolutions per minute (RPM) and pitch angle, used as input settings for the RANS cases . . . . .	32
4.13	Boundary conditions for the RANS cases under neutral (N), stable (S) and unstable (U) conditions .	33
5.1	General time-averaged LES results . . . . .	40
6.1	Shear and buoyancy production based normalization metrics for the frozen correction figures. $D = 126 \text{ m}$ and $z_i = 1070 \text{ m}$ . . . . .	49
7.1	Computational cost for the various models, measured by wall-clock time and core-time . . . . .	72

# Nomenclature

## Acronyms

ABL	Atmospheric boundary layer
ADM	Actuator disc model
ALM	Actuator line model
CAD	Computer aided design
CBL	Convective boundary layer
CFD	Computational fluid dynamics
CFL	Courant-Friedrichs-Lewy
DNS	Direct Numerical Simulation
FS	Free-stream
GDH	Gradient diffusion hypothesis
LES	Large-Eddy Simulation
LEVM	Linear eddy-viscosity model
LiDAR	Light detection and ranging
M-O	Monin-Obukhov
MAP	Maximum a posteriori estimate
MOST	Monin-Obukhov similarity theory
NLEVM	Non-linear eddy viscosity model
RANS	Reynolds Averaged Navier-Stokes
RSM	Reynolds stress model
SBL	Stable boundary layer
SOWFA	Simulator for Offshore Wind Farm Applications
SpaRTA	Sparse Regression of Turbulent Stress Anisotropy
SST	Shear stress transport
TKE	Turbulent kinetic energy

## Greek Symbols

$\delta$	Discrepancy or error	
$\delta_{ij}$	Kronecker delta	—
$\epsilon$	Dissipation rate	$m^2/s^3$
$\epsilon$	Gaussian mapping width parameter	—

$\eta$	Kolmogorov scale	$m$
$\Gamma_d$	Dry adiabatic lapse rate	$K/m$
$\kappa$	Von Kármán constant	–
$\nu$	Kinematic viscosity	$m^2/s$
$\omega$	Earth's rotation rate	$rad/s$
$\omega$	Specific dissipation rate	$1/s$
$\phi$	Latitude	$rad$
$\Phi_h$	Monin-Obukhov function for temperature	–
$\Phi_m$	Monin-Obukhov function for velocity	–
$\Psi_h$	Integrated Monin-Obukhov function for temperature	
$\Psi_m$	Integrated Monin-Obukhov function for velocity	
$\rho$	Density	$kg/m^3$
$\rho_k$	Buoyant density	–
$\tau_{ij}^{SGS}$	Sub-grid (sub-filter) stress tensor	$m^2/s^2$
$\theta$	Measurement (or reference) data	
$\theta$	Potential temperature	$K$
$\theta_*$	Surface layer temperature scale	$K$

### Roman Symbols

$L$	Characteristic length	$m$
$U$	Mean stream-wise flow velocity	$m/s$
$\Delta U$	Mean stream-wise velocity deficit	$m/s$
$\mathbb{P}$	Probability	
$\mathcal{M}$	Model	
$\overline{u'_i u'_j}$	Reynolds stress tensor	$m^2/s^2$
$\overline{u'_j \theta'}$	Turbulent heat-flux	$Km/s$
$\tilde{u}$	Filtered velocity	$m/s$
$B$	Buoyant turbulent production	$m^2/s^3$
$b_{ij}$	Normalized Reynolds stress anisotropy tensor	–
$b_{ij}^{\Delta}$	Model-form error of Reynolds stress anisotropy	
$c$	Model coefficients	
$D$	Drag force	$N$
$F$	Force	$N$
$G$	Geostrophic wind speed	$m/s$
$g_i$	Gravitational acceleration	$m/s^2$
$k$	Turbulent kinetic energy	$m^2/s^2$
$k_{SGS}$	Sub-grid scale turbulent kinetic energy	$m^2/s^2$
$L$	Lift force	$N$

$L$	Monin-Obukhov length	$m$
$M$	Theoretical steady state ABL wind speed	$m/s$
$m$	Fluid parcel or object mass	$kg$
$p$	Static pressure	$N/m^2$
$P$	Mean static pressure	$N/m^2$
$P_k$	Mechanical turbulent production	$m^2/s^3$
$Pr$	Prandtl number	—
$Pr_t$	Turbulent Prandtl number	—
$q_j^{\Delta}$	Turbulent heat-flux error	$Km/s$
$q_j^{SGS}$	Sub-grid (sub-filter) scale heat flux	$Km/s$
$q_s$	Surface heat flux	$Km/s$
$R$	$k$ transport equation residual (error)	
$Re$	Reynolds Number	—
$Ri_b$	Bulk Richardson number	—
$S_{ij}$	The mean strain-rate tensor	$1/s$
$t$	Time	$s$
$T$	Temperature	$K$
$u'$	Fluctuating velocity	$m/s$
$u''$	Sub-filter velocity	$m/s$
$u_*$	Friction velocity	$m/s$
$U_0$	Free-stream velocity	$m/s$
$u_i$	Velocity	$m/s$
$U_i$	Mean velocity	$m/s$
$x$	Stream-wise coordinate	$m$
$y$	Lateral coordinate	$m$
$z$	Wall-normal coordinate	$m$
$z_0$	Roughness length	$m$

# Introduction

## 1.1 Background

It is projected that wind energy will cover 22%-30% of Europe's energy demand by 2030. A significant increase from the 15% wind energy share in 2015 [1]. Off-shore wind energy will likely increase in share due to the ever-increasing project scales. To meet these targets, the levelized cost of energy of offshore wind needs to be further reduced. In order to do so, turbine manufacturers and operators require detailed knowledge about the conditions in which turbines will operate.

The design and optimization of wind turbines and wind farms is a complex process. The turbine wakes are turbulent regions of a velocity deficit with the free-stream. Any turbine immersed in a wake will have lower power production and higher fatigue loading. Designers must therefore understand the structure and dynamics of wind turbine wakes, as well as the interaction of multiple wakes in a farm. The relationship of wake dynamics with atmospheric stability is also important. On-shore, the atmospheric boundary layer (ABL) is stable or unstable most periods of the day, only being neutral during a short period in the morning and the evening [2]. Field experiments [3], [4] show that non-neutral conditions also occur for most periods of time throughout the year in off-shore locations.

Currently, Large-Eddy Simulation (LES) is the most appropriate method of simulating wind farm flows. The most significant scales of turbulent motion are fully resolved, leading to accurate solutions that include most of the physical phenomena in real wind farms. Reynolds-Averaged Navier-Stokes (RANS) simulations have a computation cost of about two orders of magnitude lower compared to LES [5], making them the tool of choice in industry. RANS models come in a multiplicity of flavours, with linear-eddy viscosity models (LEVM) the most popular and common ones [6]. The reduced computational cost of these models, however, comes at a price. The assumptions made in the turbulence models fail in a several complex, but common, flow cases [7], [8], including wind turbine flows [9]. The main problems include an over-prediction of turbulent kinetic energy in the edges of the near wake, resulting in increased turbulent mixing and an under-prediction of the wake velocity deficit. Numerous attempts have been made to construct engineering fixes to the turbulence models to improve the velocity predictions in the wake, with varying success. Most fixes do not generalize well beyond training cases and fail to account for atmospheric stability, leaving room for improvement.

Data-driven turbulence models aim to improve the limitations of turbulence models by assimilating higher-fidelity reference data. Various machine learning algorithms have been applied to turbulence modelling. Deep neural networks emerged first, as these have become massively popular in numerous other fields of science [10]. The drawback of 'black-box' methods, such as neural nets and random forests, is the lack of interpretability. The modeller is unable to evaluate the relation that is learned by the algorithm or manually tweak the model to match physical needs or improve stability. Symbolic data-driven techniques, on the other hand, output explicit algebraic relations. Gene expression programming has been successfully demonstrated by Weatheritt and Sandberg [11] and Weatheritt and Sandberg [12], and Schmelzer, Dwight, and Cinnella [13] demonstrated a novel framework for symbolic data-driven turbulence modelling; Sparse Regression of Turbulent Stress Anisotropy (SpaRTA). An additional benefit of a symbolic approach is that the resulting models are easily implemented in RANS solvers. Instead of applying machine learning directly to generalize the Reynolds stress tensor, it is more effective to first assess the error an existing turbulence model has with respect to the reference data, and then generalize that error with machine learning [14]. The two approaches commonly used for evaluating the turbulence model error are (i) Bayesian statistical inference, and (ii) frozen-RANS. With Bayesian inference, full-field data is not required. Frozen-RANS based approaches, on the other hand, do require full-field reference data but do not require an expensive inversion process [13]. It was shown for  $k$ -corrective-frozen-RANS (a development from the basic version) that a near-perfect match with the reference data is obtained when the derived error is injected into RANS as a correction [5], [13].

Steiner, Dwight, and Viré [5] applied the SpaRTA methodology to moderate Reynolds number wind turbine flows and significantly improved the baseline turbulence model. This study constituted an intermediate step between

canonical flows and industrial-scale flows. Future work in this research avenue is to apply SpaRTA to such full-scale flows and to improve numerical stability on various mesh resolutions. In most literature on data-driven turbulence modelling, the energy or temperature equation was not included. Some studies attempt to discover new scalar flux models using machine learning [15], [16], but these did not test the derived models in coupled RANS solvers. They only considered a priori determination of the heat flux on mean LES fields. This is likely due to the limitations of the underlying RANS turbulence model. To the best of the author's knowledge, simultaneous data-driven turbulence model improvements for the Reynolds stress and scalar-flux in heated flows have not yet been considered.

In this thesis, the research gap of simultaneous data-driven Reynolds stress and scalar-flux modelling improvements will be addressed while considering wind turbine wake flows under neutral, stable and unstable atmospheric conditions. Several LES studies for wind turbine flows in non-neutral conditions have already been conducted in literature [17]–[19] [19]. Unfortunately, for some of these studies, the time-averaged field data is no longer saved, while for others the specific data required for the present study was never saved at all. For this reason, and to ensure a certain quality, in-house large-eddy simulations are developed and validated within this thesis. Afterwards, the existing frozen-RANS framework is extended to obtain the model-form error of the turbulent heat flux. This framework will be applied to several non-neutral cases. The novel frozen-RANS framework is then validated by injecting the obtained model-form errors, now as corrections, into the RANS turbulence model during simulation run time. The performance of the corrected RANS model is then evaluated by comparison against the baseline RANS model and the LES reference data. This thesis aims to pave the way for further research on machine learning of turbulence models for industrial-scale wind turbines for non-neutral atmospheric conditions.

## 1.2 Research Questions

The project can be deemed finished when the research questions (RQ) and their sub-questions (SQ) have been answered. The various research questions are:

- (RQ1): What are the model-form errors of the  $k - \epsilon$  and GDH model in stable and unstable wind turbine flows, and how do they differ from neutral wind turbine flows?
- (RQ2): What are the considerations injecting the model-form corrections into the RANS equations during simulation?
- (RQ3): What is the accuracy of the corrected RANS models compared to the baseline RANS model and the LES model?
- (RQ4): How does the computational cost of the corrected RANS model compare to the baseline and LES models?
- (RQ5): How is the frozen-RANS framework best extended to stable and unstable conditions?

## 1.3 Research Objectives

To answer the research questions, the main research objective, and the sub-objectives must be achieved.

*"To contribute to algebraic data-driven turbulence model development, and the understanding of turbulence for industrial-scale wind turbine flows in neutral and non-neutral atmospheric conditions, by inferring the model form error of the benchmark  $k - \epsilon$  turbulence model and the gradient-diffusion scalar-flux model from high fidelity data."*

The following sub-objectives (SO) are formulated in support of the main objective.

- (SO1): To generate ground-truth reference data by running Large-Eddy Simulations with the open-source CFD package OpenFOAM-SOWFA.
- (SO2): To determine the model form corrections of the  $k - \epsilon$  and Gradient-Diffusion Hypothesis models by formulating a novel frozen-RANS framework in OpenFOAM-SOWFA.
- (SO3): To validate the model form corrections by injecting them into the OpenFOAM-SOWFA solvers and comparing against the ground truth.
- (SO4): To determine the regions and mechanisms of baseline turbulence model failure by assessing the validated model form corrections.

## 1.4 Report Structure

Firstly, the thesis contains a summary of the relevant literature on the atmospheric boundary layer, atmospheric stability and wind turbine flows in chapter 2. Chapter 3 contains a summary of the relevant literature on CFD, turbulence modelling and data-driven turbulence model improvements. The complete methodology of LES data generation, frozen-RANS framework and the corrected RANS simulations are presented in chapter 4. The LES results and validation are shown in chapter 5, after which the frozen-RANS model-form errors are discussed in chapter 6. The corrected RANS models are tested against the baseline and the LES model in chapter 7. Finally, the conclusions and recommendations to future work are discussed in chapter 8.

# The Atmospheric Boundary Layer and Wind Turbine Flows

When a solid object is immersed in a fluid flow, a boundary layer forms over the surface of the object. Adhesion causes the fluid to have the same velocity as the object on the surface of the object, and diffusive effects smooth the velocity profile, which becomes the free stream velocity outside of the boundary layer. Laminar boundary layers are characterized by the fluid moving in orderly parallel shear layers, whereas turbulent boundary layers are characterized by chaotic motions in the fluid, higher degrees of mixing and higher skin friction. The Reynolds number of the flow, defined as the ratio between the inertial and viscous forces, is used to determine or indicate whether a flow is laminar, turbulent or in a state of transition between the two. The Reynolds number is defined based on a characteristic length of the flow  $L$ .

$$Re = \frac{UL}{\nu} \quad (2.1)$$

$U$  and  $\nu$  are the free stream velocity and the kinematic viscosity, respectively. The bottom 300  $m-3 km$  of the troposphere is known as the atmospheric boundary layer (ABL). Just as with any other boundary layer, the flow velocity is zero at the surface and equal to the free-stream outside of the boundary layer, which is the geostrophic wind speed in case of the atmospheric boundary layer. The ABL is the only part of the atmosphere that is directly affected by the presence of the Earth's surface. Besides the drag due to surface roughness, these effects are the heating of air during the day, cooling of air during the night, and changes in humidity and pollutant concentration [20].

The geostrophic wind speed and driving forces in the ABL are discussed in section 2.1. Atmospheric stability and Monin-Obukhov similarity theory are discussed in section 2.2 and section 2.3, respectively. Finally, a brief summary of wind turbine flows is presented in section 2.4.

## 2.1 Driving Forces in the Atmosphere

The winds in Earth's atmosphere are driven by a multiplicity of forces. Generally speaking, these wind driving forces are time-varying and depend on heat and moisture, which are convected with the air. This results in a complicated coupling that we refer to as weather [20]. The geostrophic wind speed is defined as the wind speed in which the free atmosphere (the part of the troposphere above the atmospheric boundary layer) is in geostrophic balance. In other words, the geostrophic wind speed is the theoretical steady-state wind speed above the ABL [20]. Two forces are important for the determination of the geostrophic wind speed: the horizontal pressure gradient force and the Coriolis force. The pressure gradient force and the Coriolis force are by eq. (2.2) and eq. (2.3), respectively.

$$\frac{\mathbf{F}_{PG}}{m} = -\frac{1}{\rho}\nabla P \quad (2.2)$$

$$\frac{\mathbf{F}_C}{m} = -2\boldsymbol{\Omega} \times \mathbf{U} \quad , \quad \boldsymbol{\Omega} = \omega \begin{bmatrix} 0 \\ \cos(\phi) \\ \sin(\phi) \end{bmatrix} \quad (2.3)$$

Here,  $\omega$  is Earth's rotation rate and  $\phi$  is the latitude. Since the pressure gradient force and the Coriolis force are the only acting forces, and the Coriolis force acts normal to the velocity vector per definition, both forces cancel out and the geostrophic wind blows parallel to the isobars in weather maps. This is illustrated in fig. 2.1a, taken from Stull [20]. When considering the theoretical steady-state wind speed inside the ABL, the surface drag force needs to be considered as well. This drag not only slows the wind but also rotates it with respect to the geostrophic wind speed. In fig. 2.1b, also taken from Stull [20], it is seen that the vector sum of the drag and the Coriolis force cancel the pressure gradient force. The theoretical steady-state forces vary as a function of depth in the ABL due to the local

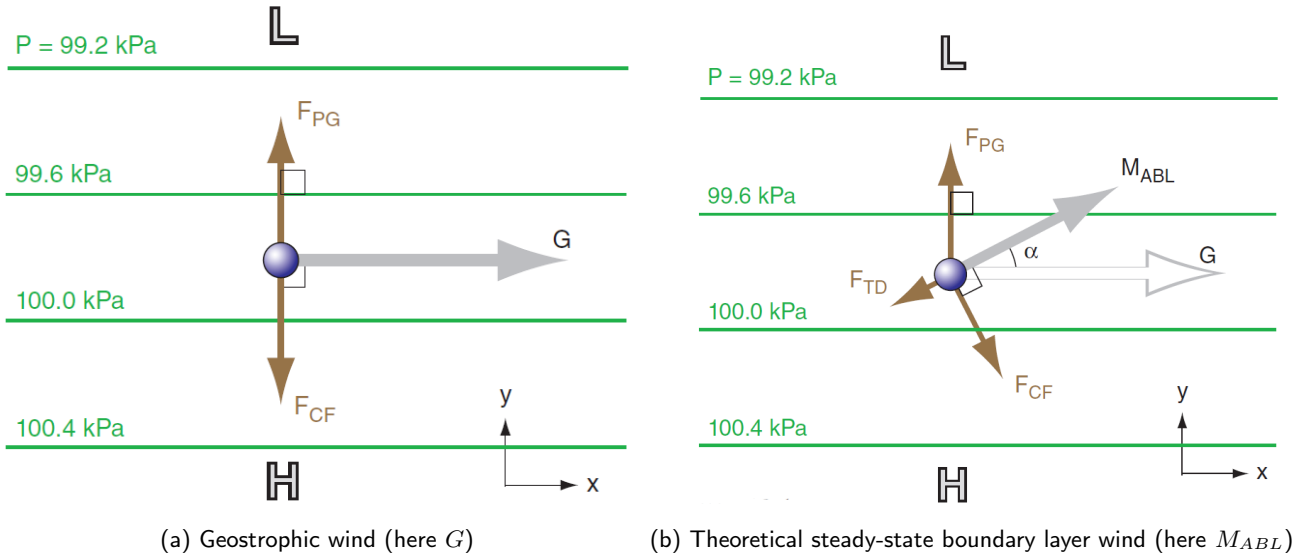


Figure 2.1: Idealized weather maps for the northern hemisphere showing theoretical steady-state winds. Figure taken from Stull [20].

gradients. Consequently, the angle between the local steady-state wind and the geostrophic wind changes as well, forming a so-called Ekman spiral [20].

## 2.2 Atmospheric Stability

The ABL is generally turbulent to some degree. However, rather than using the Reynolds number as a metric for turbulence, it is informative to assess the degree of atmospheric stability, which depends on buoyancy. In the ABL, a buoyant force  $\mathbf{F}_b$  acts on a parcel of air when there is a difference in density  $\rho$  between the parcel (subscript  $p$ ) and its environment (subscript  $e$ ). The value of the buoyant force is given by the following expression.

$$\frac{\mathbf{F}_b}{m} = \frac{\rho_p - \rho_e}{\rho_p} \cdot \mathbf{g} \quad (2.4)$$

Buoyant forces arise naturally in the ABL under various vertical temperature gradients or atmospheric lapse rates. Consider a parcel of air that is displaced away from the Earth's surface. It expands due to the lower pressure. The work done during this expansion is adiabatic (without any heat exchange) and causes the parcel to drop in temperature, at a rate  $\Gamma_d$ ; the dry adiabatic lapse rate. When the lapse rate of the air in the ABL is larger than the dry adiabatic lapse rate, the vertically displaced air parcel is warmer than its environment. Consequently, it has a lower density, resulting in a buoyant force acting upwards. The air parcel thus travels upwards even further in a so-called thermal. The atmosphere, in this case, is referred to as unstable, or convective. The atmosphere is stable when the lapse rate is lower than the dry adiabatic lapse rate. In this case, an upwards displacement of an air parcel results in it being colder than its direct environment, causing a downwards buoyant force. Figure 2.2 (from Stull [20]) shows a thermo-diagram for a simplified unstable atmosphere. This diagram allows for an easy comparison between the parcel temperature and the environment temperature. Note that the potential temperature is defined simply as  $\theta = T + \Gamma_d z$ .

The unstable ABL or convective boundary layer (CBL) is, due to positive buoyancy, associated with higher degrees of ambient turbulence. Higher turbulence in boundary layers is associated with enhanced momentum transport towards the surface, resulting in nearly constant velocity profile with low shear. Right by the surface, the mean velocity profile decreases rapidly until it is zero at the wall. This state is in stark contrast with the stable boundary layer (SBL), where negative buoyancy suppresses atmospheric turbulence. As shown in fig. 2.3, taken from Stull [20], the relative lack of turbulence in the SBL results in lower vertical momentum transport and much larger wind shear. In the figure,  $z_{SL}$  is the height of the surface layer (the bottom 5% of the ABL [20]), and  $M$  is the mean wind speed.

A strong diurnal cycle occurs in the atmospheric boundary layer over land due to the periodic heating of the sun [20]. During the day, the surface is hotter than the atmosphere, resulting in unstable conditions. During the night conditions are stable. In fact, the ABL is non-neutral during most periods of the day, only being neutral during a short period in the morning and the evening [2]. As shown in field experiments [3], [4], non-neutral conditions also occur for most periods of time throughout the year in off-shore locations, highlighting the importance of considering atmospheric stability in the analysis of wind turbine wakes.

The Monin-Obukhov (M-O) length  $L = -u_*^3 \theta_0 / (\kappa g q_s)$  is often used as a quantitative measure for atmospheric stability. It is defined through the friction velocity  $u_*$ , the von Kármán constant  $\kappa = 0.4$ , gravitation acceleration  $g$ ,

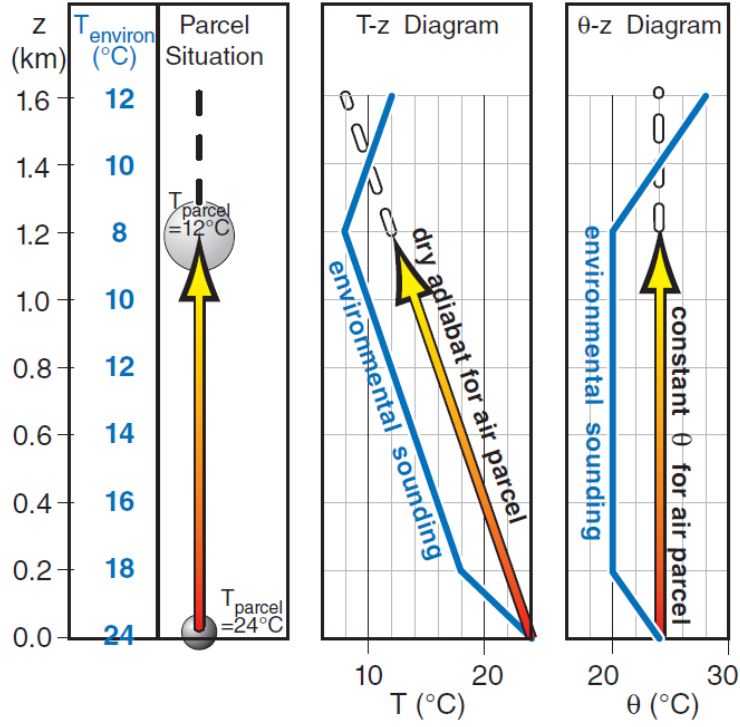


Figure 2.2: Thermo-diagram for a simplified unstable atmosphere. The rising parcel is compared to its environment in temperature (left) and potential temperature (right). Figure from [20].

the surface heat flux  $q_s$  and the reference potential temperature  $\theta_0$ . Peña, Gryning, and Mann [21] distinguished between several stability classifications based on the Monin-Obukhov Length. These classifications are shown in table 2.1. Another common method for quantifying atmospheric stability in field measurements is the Bulk-Richardson approach, based on  $Ri_b$ , the Bulk-Richardson number [17]. Pandolfo [22] derived simple empirical relationships that relate the Bulk-Richardson number to the Monin-Obukhov length.

Table 2.1: Atmospheric stability classes, as defined by the Monin-Obukhov Length. Table obtained from Peña, Gryning, and Mann [21].

Monin-Obukhov length	Stability class
$-100 \leq L \leq -50$	Very unstable
$-200 \leq L \leq -100$	Unstable
$-500 \leq L \leq -200$	Near unstable
$ L  > 500$	Neutral
$200 \leq L \leq 500$	Near stable
$50 \leq L \leq 200$	Stable
$10 \leq L \leq 50$	Very stable

## 2.3 Monin-Obukhov Similarity

Monin-Obukhov similarity theory describes the structure of the surface layer, the lowest part of the ABL. Using dimensional analysis and the Buckingham-Pi theorem, two non-dimensional independent variables are said to be functionally related, making one a dependant variable. The formulation is such that the dependant variable is a function only of the  $z/L$ ,  $L$  being the Monin-Obukhov (M-O) length. The resulting expression for the constant surface layer wind speed gradient is given by eq. (2.5). The surface layer potential temperature gradient is given by eq. (2.6).

$$\frac{\kappa z}{u_*} \frac{\partial U}{\partial z} = \Phi_m \left( \frac{z}{L} \right) \quad (2.5)$$

$$\frac{\kappa z}{\theta_*} \frac{\partial \theta}{\partial z} = \Phi_h \left( \frac{z}{L} \right) \quad (2.6)$$

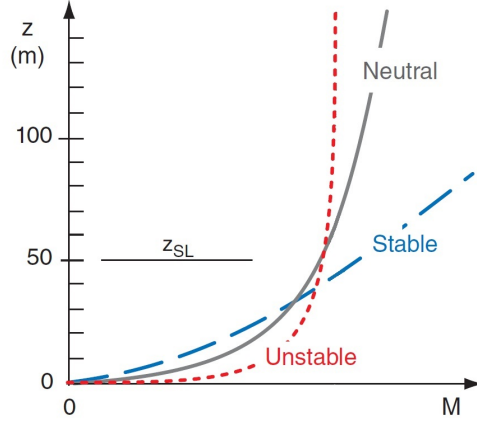


Figure 2.3: Typical velocity profiles for the unstable, stable and neutral boundary layer. The figure is taken and adapted from Stull [20].

The functions  $\Phi_m$  and  $\Phi_h$  are called the M-O functions. They are said to be universal, meaning they are identical for all surface layers that are locally homogeneous and quasi-steady. The surface layer temperature scale is defined as  $\theta_* = \frac{\theta_0 u_*^2}{g\kappa L}$ . The M-O functions are linear in the stable region but have a more complex form in the unstable region. Using an analytical formulation for the functions allows for integration of eq. (2.5) and eq. (2.6), resulting in expressions for the mean velocity profile eq. (2.7), and mean potential temperature profile eq. (2.8). These expressions are, however, only valid in the surface layer, which roughly constitutes the bottom 5% of the ABL [20].

$$U(z) = \frac{u_*}{\kappa} \left[ \ln\left(\frac{z}{z_0}\right) - \Psi_m\left(\frac{z}{L}\right) \right] \quad (2.7)$$

$$\Theta(z) = \theta_0 + \frac{\theta_*}{\kappa} \left[ \ln\left(\frac{z}{z_0}\right) - \Psi_h\left(\frac{z}{L}\right) \right] \quad (2.8)$$

The roughness length  $z_0$  a parameter which characterizes the surface roughness. It is reported in Laan, Kelly, and Sørensen [23] that the most commonly used functions for  $\Phi_m$  and  $\Phi_h$ , and the resulting  $\Psi_m$  and  $\Psi_h$  are those of the field measurements of Dyer [24] and Businger, Wyngaard, Izumi, *et al.* [25]. They are shown in eq. (2.9) and eq. (2.10), with the corresponding coefficients shown in table 2.2.

$$\begin{aligned} \Psi_m &= \ln \left[ \frac{1}{8} (1 + \Phi_m^{-2})(1 + \Phi_m^{-1})^2 \right] - 2\arctan(\Phi_m^{-1}) + \frac{\pi}{2} \\ \text{Unstable conditions} \quad \Psi_h &= (1 + \sigma_\theta) \ln \left[ \frac{1}{2} (1 + \Phi_h^{-1}) \right] + (1 - \sigma_\theta) \ln \left[ \frac{1}{2} (-1 + \Phi_h^{-1}) \right] \end{aligned} \quad (2.9)$$

$$\begin{aligned} \Phi_m &= \left( 1 - \gamma_1 \frac{z}{L} \right)^{-1/4} \\ \Phi_h &= \sigma_\theta \left( 1 - \gamma_2 \frac{z}{L} \right)^{-1/2} \end{aligned}$$

$$\begin{aligned} \text{Stable conditions} \quad \Psi_m &= -\beta \frac{z}{L} \\ \Psi_h &= (1 - \sigma_\theta) \ln \left( \frac{z}{L} \right) - \beta \frac{z}{L} \\ \Phi_m &= 1 + \beta \frac{z}{L} \\ \Phi_h &= \sigma_\theta + \beta \frac{z}{L} \end{aligned} \quad (2.10)$$

## 2.4 Wind Turbines and Wakes

Wind turbines are energy conversion devices that extract momentum from the air. At the level of the blade cross-section (or blade-element), the flow around the blade-element induces a result force  $F$ , as shown in fig. 2.4, obtained from

Table 2.2: Empirically determined coefficients of the Monin-Obukhov functions

	$\sigma_\theta$	$\beta$	$\gamma_1$	$\gamma_2$
Businger, Wyngaard, Izumi, <i>et al.</i> [25]	0.74	4.7	15	9
Dyer [24]	1	5	16	16

Porté-Agel, Wu, Lu, *et al.* [26]. The sum, over all three blades, of the normal component  $F_x$  results in a thrust force on the turbine. The tangential components  $F_\theta$  contribute towards the torque that drives the generator.

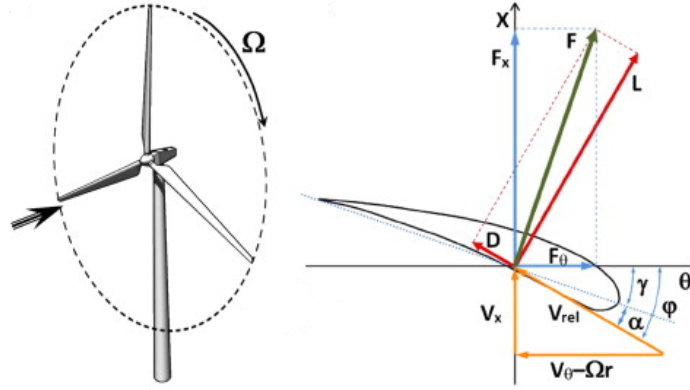


Figure 2.4: Schematic of the resultant force acting on the blade element and the decomposed forces. Figure obtained from Porté-Agel, Wu, Lu, *et al.* [26].

By Newton's third law, the wind turbine blades produce a stream-wise and tangential force that acts upon the air, affecting the flow field. Distinct regions are often distinguished when discussing wind turbine flows. Upwind of the turbine, there is the induction region, which is characterised by decelerated air. Downwind of the turbine, there is the wake region, which is characterised by a velocity deficit (due to the momentum extraction) and by increased turbulence. The wake is further divided into the near wake and the far wake. The near wake stretches until 2-4 rotor diameters downwind of the turbine. In this region, one will find coherent helical vortical structures that originate from the blade tips and from the turbine hub. The flow field in the near wake is directly affected by the blade, hub and nacelle geometry [27]. The far wake, however, is independent of the specific geometry and can be characterised by the global operating parameters, such as the tip-speed ratio and thrust coefficient. Large scale meandering is observed in turbine wakes in the atmospheric boundary layer. These motions are associated with very large turbulent fluctuations in the atmosphere. Figure 2.5 shows a schematic of the flow around wind turbines. The figure is taken from Porté-Agel, Bastankhah, and Shamsoddin [28].

Understanding the behaviour of the far wake is crucial because wind turbines in large wind farms usually operate in the far wake of upstream turbines. The mean stream-wise velocity deficit  $\Delta U = U_0 - U$ ,  $U_0$  being the mean stream-wise incoming velocity, is shown to closely match the axisymmetric Gaussian distribution in wind tunnel experiments of a wind turbine in boundary layer flow [29]. Since the Gaussian profile is self-similar, the normalized (by magnitude and width) velocity deficit profile is independent of stream-wise position in the far wake. This has facilitated the development of several analytical models. It should be noted that the Gaussian profile is only observed for standalone turbines, not for turbines that operate in the wakes of other turbines. As the distance from the turbine increases, the wake expands and the velocity recovers due to turbulent mixing with the undisturbed air outside of the wake.

It was shown in field measurements [17], [30], [31] that The wake deficit and rate of recovery depend strongly on atmospheric stability. The quicker wake recovery for unstable cases is associated with wake meandering caused by large convective motions [17], as well as an earlier breakdown of tip vortices, resulting in higher entrainment with the flow outside of the wake [28]. Figure 2.6 shows contour plots of instantaneous and time-averaged velocity for a very stable atmosphere (left) and an unstable atmosphere (right), obtained from Macheaux, Larsen, Koblitiz, *et al.* [17]. The authors show a higher meandering amplitude for the unstable case, but also mention that these LES results still under-predict the unstable meandering magnitude compared to their field experiments. Consequently, their LES slightly under-predicts wake recovery.

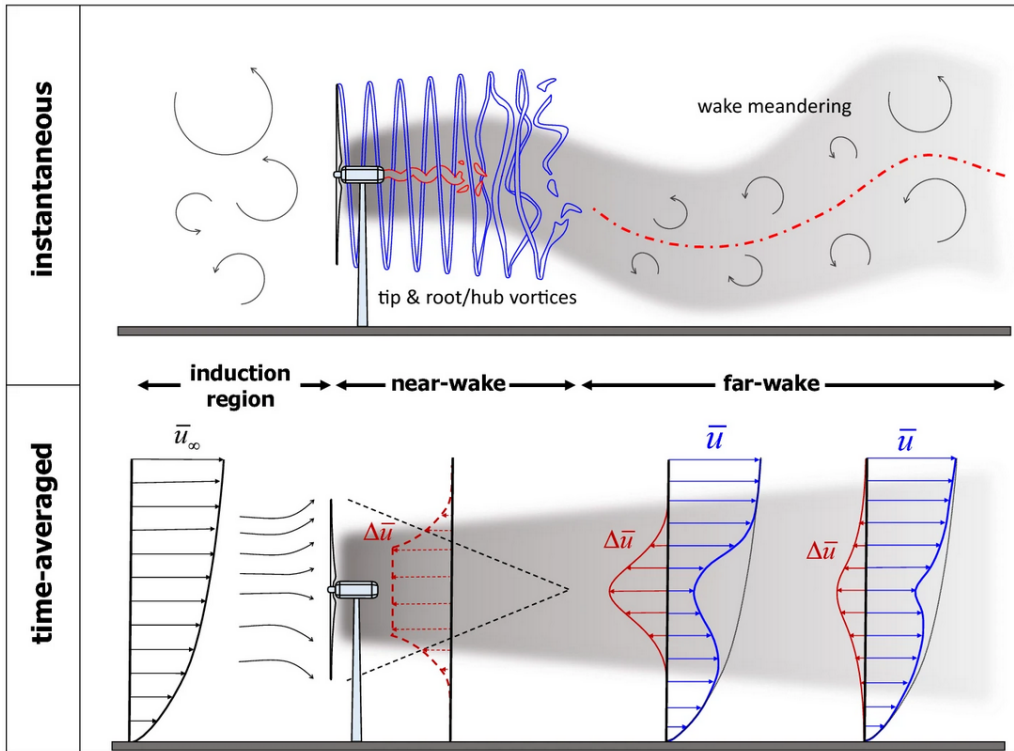


Figure 2.5: Schematic of the wake and its distinct regions. Figure obtained from Porté-Agel, Bastankhah, and Shamsoddin [28].

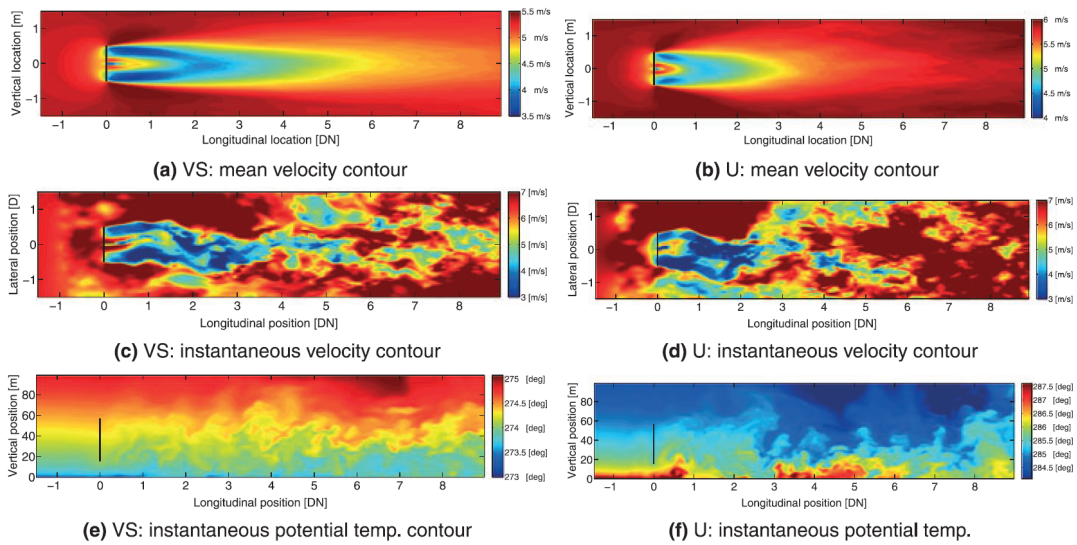


Figure 2.6: Velocity and potential temperature contours from LES for very stable conditions (left plots) and unstable conditions (right plots). Figure obtained from Macheaux, Larsen, Koblitz, *et al.* [17].

# Computational Fluid Dynamics and Turbulence Modelling

Computational Fluid Dynamics (CFD) is the field of science that involves methods for finding numerical solutions to the governing equations of fluid flow. These equations are the conservation of mass, momentum and energy, and are often referred to as the Navier-Stokes equations. There are various methods to solve these equations, each with a different level of fidelity and computational cost. The three main methods are Direct Numerical Simulation, Large-Eddy Simulation and Reynolds-Averaged Simulation. These are discussed in section 3.1, section 3.2 and section 3.3, respectively. A short discussion on buoyancy is included in section 3.1. Section 3.4 presents various methods of handling turbines in CFD and, finally, data-driven turbulence modelling approaches are discussed in section 3.5.

## 3.1 Direct Numerical Simulation

Direct Numerical Simulation (DNS) is the CFD type in which the governing equations are solved as is, without any turbulence model. All turbulent scales are fully resolved. Excluding the energy equation, and assuming constant density, the Navier-Stokes equations are as follows.

$$\frac{\partial u_i}{\partial x_i} = 0 \quad (3.1)$$

$$\frac{\partial u_i}{\partial t} + \frac{\partial u_i u_j}{\partial x_j} = -\frac{1}{\rho} \frac{\partial p}{\partial x_i} + \nu \frac{\partial^2 u_i}{\partial x_j \partial x_j} + g_i \quad (3.2)$$

With  $u_i$  the fluid velocity,  $p$  the static pressure,  $\nu$  the kinematic viscosity and  $g_i$  the gravitational acceleration vector. A requirement when doing DNS is that the mesh needs to be sufficiently fine in order to resolve any turbulent eddy between the largest scales in the flow, of size  $L$ , and the smallest Kolmogorov scales, of size  $\eta$ . The size ratio between the Kolmogorov scale and the largest scale is known given by the following equation [7].

$$\frac{\eta}{L} = Re^{-3/4} \quad (3.3)$$

Most fluid flows in nature and engineering are of very large Reynolds number. As such, a very fine mesh is required in order to resolve the Kolmogorov scales. The computational cost of DNS is therefore prohibitive for most practical cases.

Strictly speaking, the full compressible governing equations are required in the CFD formulation for atmospheric boundary layers, since temperature variations result in density variations. However, using the Boussinesq buoyancy approximation for the buoyant force term allows for the use of the incompressible flow equations. The approximation is obtained by expanding the gravitational force term in the momentum equation,  $\rho g_i$  into a constant reference term, indicated by subscript 0, and a term that constitutes the difference with the constant.

$$\rho g_i = \rho_0 g_i + (\rho - \rho_0) g_i \quad (3.4)$$

Here,  $\rho$  is the density which varies with temperature  $T$  and  $\rho_0$  is the constant reference density. A first-order Taylor expansion for  $\rho(T)$ , with  $\beta = -\frac{\partial \rho}{\partial T}|_{T=T_0}$  the coefficient of thermal expansion, is then introduced. The expression for the Boussinesq approximation is given below in terms of temperature  $T$  and potential temperature  $\theta = T + \Gamma_d z$ , with  $\Gamma_d$  the dry adiabatic lapse rate.

$$\frac{\rho}{\rho_0} g_i = \rho_k g_i = g_i (1 - \beta(T - T_0)) = g_i (1 - \beta(\theta - \theta_0)) \quad (3.5)$$

In the momentum equation, eq. (3.2), the gravitational acceleration vector  $g_i$  is then replaced by  $\rho_k g_i$ , and the buoyant density  $\rho_k$  is found by solving the scalar transport equation for the potential temperature  $\theta$ .

$$\frac{\partial \theta}{\partial t} + \frac{\partial \theta u_j}{\partial x_j} = \frac{\nu}{Pr} \frac{\partial^2 \theta}{\partial x_j \partial x_j} \quad (3.6)$$

## 3.2 Large Eddy Simulation

In Large Eddy Simulations (LES), the problem of having to resolve the up to the Kolmogorov scales is solved by separating the scales using a filter  $(\widetilde{\dots})$ . This filter is applied to the full solution  $u(\mathbf{x}, t)$ , letting through a resolved component and filtering out a sub-filter component.

$$u(\mathbf{x}, t) = \widetilde{u}(\mathbf{x}, t) + u''(\mathbf{x}, t) \quad (3.7)$$

The LES equations are derived by applying the filtering operation to the Navier-Stokes equations, eq. (3.1) and eq. (3.2). This yields the LES equations, eq. (3.8) and eq. (3.9), and the LES scalar transport equation eq. (3.10).

$$\frac{\partial u_i}{\partial x_i} = 0 \quad (3.8)$$

$$\frac{\partial \widetilde{u}_i}{\partial t} + \frac{\partial \widetilde{u}_i \widetilde{u}_j}{\partial x_j} = -\frac{1}{\rho} \frac{\partial \widetilde{p}}{\partial x_i} + \frac{\partial}{\partial x_j} \left( \nu \frac{\partial \widetilde{u}_i}{\partial x_j} - \tau_{ij}^{SFS} \right) + \widetilde{\rho}_k g_i, \quad \tau_{ij}^{SFS} = \widetilde{u_i u_j} - \widetilde{u}_i \widetilde{u}_j \quad (3.9)$$

$$\frac{\partial \widetilde{\theta}}{\partial t} + \frac{\partial \widetilde{\theta} \widetilde{u}_j}{\partial x_j} = \frac{\partial}{\partial x_j} \left( \frac{\nu}{Pr} \frac{\partial \widetilde{\theta}}{\partial x_j} - q_j^{SFS} \right), \quad q_j^{SFS} = \widetilde{\theta u_j} - \widetilde{\theta} \widetilde{u}_j \quad (3.10)$$

With  $\delta_{ij}$  the Kronecker delta. The quantity  $\tau_{ij}^{SFS}$  is the sub-filter stress tensor and  $q_j^{SFS}$  the sub-filter scale heat flux. These quantities account for the effect of the sub-filter turbulent fluctuations on the resolved (or filtered) flow. Both quantities require modelling, since, in the simulations, filtered products such as  $\widetilde{u_i u_j}$  are unknown. It is important to note that, in most Large Eddy Simulations, the filter  $(\widetilde{\dots})$  is not explicitly defined. Rather, it is defined implicitly by the local mesh, since no turbulent fluctuations of size smaller than the local mesh can be resolved in the simulation. In such LES, the term sub-filter is often exchanged with sub-grid, and  $\tau_{ij}^{SFS}$  is exchanged with  $\tau_{ij}^{SGS}$ .

The simplest closure model for the deviatoric part of the SGS stress tensor is the model of Smagorinsky [32].

$$\tau_{ij}^{SGS} - \frac{2}{3} k^{SGS} \delta_{ij} = -2\nu_{SGS} \widetilde{S}_{ij} = -2\Delta^2 C_s^2 |\widetilde{S}| \widetilde{S}_{ij} \quad (3.11)$$

Here,  $k^{SGS} = \frac{1}{2} \tau_{kk}^{SGS}$  is the SGS turbulent kinetic energy,  $\nu_{SGS}$  is the SGS viscosity,  $\widetilde{S}_{ij}$  is the resolved strain rate tensor with magnitude  $|\widetilde{S}|$ ,  $\Delta$  is the local filter width, often taken as the cube root volume of the cell, and  $C_s$  is a model constant. The isotropic part of the stress tensor is absorbed into the pressure term, forming a modified pressure  $\widetilde{p}^M = \widetilde{p} + \frac{2}{3} k^{SGS}$ . In the basic Smagorinsky model  $C_s$  is set as a constant. More sophisticated models, such as the Dynamic Smagorinsky model [33] use an explicitly defined filter to locally optimize the value of the model coefficient. Another noteworthy LES closure is the WALE model [34], which was specifically designed to have correct cubic near wall scaling of the SGS viscosity without a dynamic procedure. The choice of sub-grid scale model does, however, not have a significant impact on the time averaged wake structure if the mesh is sufficiently fine [35].

## 3.3 Reynolds-Averaged Navier-Stokes

In LES, the largest turbulent scales are resolved, and the effect of the smaller scales are modelled. Another approach is to resolve no turbulence and represent all turbulence by models. This approach is referred to as Reynolds-Averaged Navier-Stokes (RANS). RANS allows much coarser meshes resulting in much lower associated computational costs. The RANS equations are derived by first decomposing all relevant quantities in the governing equations into a mean part (indicated by capital letters or symbols) and a fluctuating part with zero mean (indicated by a prime).

$$u(\mathbf{x}, t) = U(\mathbf{x}) + u'(\mathbf{x}, t) \quad (3.12)$$

The governing equations are then ensemble averaged  $(\overline{\dots})$ . This results in the RANS equations eq. (3.13) and eq. (3.14), and the RANS scalar transport equation eq. (3.15).

$$\frac{\partial U_i}{\partial x_i} = 0 \quad (3.13)$$

$$\frac{\partial U_i U_j}{\partial x_j} = -\frac{1}{\rho} \frac{\partial P}{\partial x_i} + \frac{\partial}{\partial x_j} \left( \nu \frac{\partial U_i}{\partial x_j} - \overline{u'_i u'_j} \right) + \overline{\rho_k} g_i \quad (3.14)$$

$$\frac{\partial \Theta U_j}{\partial x_j} = \frac{\partial}{\partial x_j} \left( \frac{\nu}{Pr} \frac{\partial \Theta}{\partial x_j} - \overline{u'_j \theta'} \right) \quad (3.15)$$

The Reynolds decomposition and ensemble averaging introduce the Reynolds stress tensor (or the turbulent momentum flux)  $\overline{u'_i u'_j}$  in the momentum equation and the turbulent heat flux  $\overline{u'_j \theta'}$  in the potential temperature conservation equation. Similarly, as with LES, these fluxes depend on quantities that are unknown and, thus, require modelling.

Due to the modelling of the turbulent fluxes, uncertainty is introduced in the RANS equations at several levels. These levels are described in [14] from level L1 to level L4. L1 is the uncertainty due to the averaging operation combined with the nonlinear advection term. It is fundamentally impossible for the closure model to exactly reconstruct the turbulent fluxes, since information is lost in the averaging process, regardless of the choice of model. L2 is the uncertainty due to the model form error of the closure model selected or developed. L3 is the uncertainty due to the choice of functional form within the model. Finally, L4 is the uncertainty due to the calibration of model coefficients. Perfect turbulence models will inherently still be subject to L1 uncertainty. Uncertainty is also introduced into the LES solution due to modelling. However, this uncertainty is much lower since the largest, energy-containing, turbulent scales are resolved, and not subject to modelling errors.

The most common turbulence models for the Reynolds stress are based upon the Boussinesq eddy-viscosity hypothesis [36]. This theory relates the deviatoric part of the Reynolds stress to the hypothetical 'eddy viscosity' and the mean rate of strain tensor  $S_{ij}$ .

$$\overline{u'_i u'_j} - \frac{2}{3} k \delta_{ij} = -2\nu_t S_{ij} \quad (3.16)$$

Since this expression for the Reynolds stress is linear with the mean rate of strain, these models are referred to as linear eddy-viscosity models (LEVM). The adequacy of this assumption is questionable for a large number of flows. Even though the eddy-viscosity is analogous to the molecular viscosity, it is not a real physical quantity, so the hypothesis is not informed by real physics [6]. It has also been shown, using multiple DNS data-sets, that there is poor alignment between the Reynolds stress tensor and the mean rate of strain [37]. This results in the hypothesis failing for flows with sudden changes in rate of strain, flows with strong streamline curvatures and three-dimensional flows [6], as well as flows with anisotropic turbulence [7].

### 3.3.1 $k - \epsilon$ Model

Despite their shortcomings, LEVMs have always been the most popular turbulence model type. One of the first and most popular LEVM is the  $k - \epsilon$  model of Launder and Spalding [38]. This model calculates the eddy viscosity  $\nu_t$  from the turbulent kinetic energy (TKE)  $k$  and the dissipation rate  $\epsilon$ .

$$\nu_t = C_\mu \frac{k^2}{\epsilon} \quad (3.17)$$

The TKE and the dissipation rate are given by their respective transport equations. The  $k$  transport equation is derived by manipulation of the momentum equation. The  $\epsilon$  transport equation is, however, mostly empirical in its nature, further introducing errors in the model [6].

$$\frac{Dk}{Dt} = P_k + B - \epsilon + \frac{\partial}{\partial x_j} \left[ \left( \nu + \frac{\nu_t}{\sigma_k} \right) \frac{\partial k}{\partial x_j} \right] \quad (3.18)$$

$$\frac{D\epsilon}{Dt} = \frac{\epsilon}{k} (C_{1\epsilon} P_k - C_{2\epsilon} \epsilon + C_{3\epsilon} B) + \frac{\partial}{\partial x_j} \left[ \left( \nu + \frac{\nu_t}{\sigma_\epsilon} \right) \frac{\partial \epsilon}{\partial x_j} \right] \quad (3.19)$$

$\sigma_k$  and  $\sigma_\epsilon$  are known as the Schmidt numbers. And  $C_{1\epsilon}$ ,  $C_{2\epsilon}$  and  $C_{3\epsilon}$  are model coefficients.  $P_k$  is the shear (mechanical) production of turbulence and  $B$  is the buoyant production of turbulence, with  $\theta_0$  being the reference potential temperature.

$$P_k = -\overline{u'_i u'_j} \frac{\partial U_i}{\partial x_j}$$

$$B = -\frac{g_i}{\theta_0} \overline{u'_i \theta'}$$

The  $k - \epsilon$  model is a simple, complete and robust turbulence model. It is implemented in most RANS solvers and is applicable to a wide range of simple flows. Nevertheless, its accuracy is limited. The standard model is unable to correctly predict the atmospheric boundary layer turbulence due to its incapability of predicting anisotropic turbulence

[7]. Additionally, the standard  $k - \epsilon$ , as well as the  $k - \omega$  model, fails in the region of high strain in the near wake of a wind turbine. In these regions, an overproduction of turbulent kinetic energy results in high mixing and an under-predicted wake velocity deficit [9], [39]–[42]. Réthoré [40] found that two assumptions, made in the Boussinesq hypothesis, are violated in wind turbine wake flows. The first assumption is that the flow particles remain constant in their velocity over the turbulent time scale. This assumption is violated around the rotor, in the region of large adverse pressure gradients. The main contribution to the TKE build-up, due to this violation, is due to the over-predicted axial normal Reynolds stress  $-\overline{u_1' u_1'}$ . The second violated assumption is that the fluid velocity is linear over a local length scale. These assumptions do not seem to hold at the interface between the wake and the free-stream.

### 3.3.2 Improvements to the $k - \epsilon$ and $k - \omega$ Models

Numerous attempts have been made to overcome the wake deficit under-prediction issue, observed when using the  $k - \epsilon$  or  $k - \omega$  turbulence model. El Kasmi and Masson [39] tested the addition of a source term in the  $\epsilon$  model equation. This source term activates in the near wake, suppressing local TKE overproduction. In a study by Prospathopoulos, Politis, Rados, *et al.* [41], several changes were proposed and tested to overcome the wake deficit issue. Firstly, a source term, similar to the one tested by El Kasmi and Masson, was added to the dissipation equation, now instead for the  $k - \omega$  model. Additionally, the authors attempted to modify the value of the model coefficients in order to change the turbulence decay ratio. Both changes resulted in better wake deficit predictions. However, the changes did not generalize well to other test cases. Furthermore, the authors tested a method that adds a realizability limit to the turbulence timescale. This method was originally developed by Durbin [43] with the objective of improving stagnation point flows. Since similarly high turbulent time scale values are observed in some regions in the near wake, the Durbin method is also applicable in the current context. Although physics informed and without the need for calibration, no desired results were obtained. Finally, model constants were adjusted in order to enforce consistency with Monin-Obukhov similarity theory for stable atmospheric boundary layers. The results, however, showed a considerable underestimation of turbulence in the near wake.

Réthoré [40] constructed additional eddy viscosity limiters based on the local pressure gradient and on Realizability by the Schwartz inequalities. The limiters essentially attempt to correct the identified violations to the assumptions of the Boussinesq hypothesis. The adverse pressure gradient based limiter is shown to have better agreement with LES close to the rotor, where the adverse pressure gradient is large, but poor further away from the rotor. The Realizability limiter showed some improvements at the wake interface but was overall not consistent enough with LES.

Laan, Sørensen, Réthoré, *et al.* [9] developed a  $k - \epsilon$  extension with a variable  $C_\mu$  (the model constant in eq. (3.17)), through a limiter function called  $f_p$ . The limiter function is a simplified version of the cubic non-linear eddy viscosity model of Apsley and Leschziner [44], with all non-linear terms omitted from the formulation. The stress-strain relationship is still linear, so only isotropic turbulence is predicted meaning that the Reynolds stress predictions are not improved, only wake deficit predictions. The proposed model is tested against the baseline model for several LES data sets and experiments. The  $k - \epsilon - f_p$  model shows improvements for close to all cases. Only in the case of high total turbulence intensity did the the baseline  $k - \epsilon$  model agree better with LES. In further work van der Laan and Andersen [45] the  $k - \epsilon - f_p$  was compared against the the Realizable  $k - \epsilon$  of Shih, Liou, Shabbir, *et al.* [46], and  $k - \epsilon$  with limiter function based on Durbin's model [43] by testing against LES reference data for low and high ambient turbulence intensity. It was found that all models were able to predict the turbulent time scale well, but only the  $k - \epsilon - f_p$  model and the Shih model predicted the correct turbulent length scale. The  $k - \epsilon - f_p$  model was tested further on wind farm scale [47]. In particular, power output was obtained from the RANS simulations and compared to field measurements from the Wieringermeer, Lillegrund and Horns Rev wind farms. The  $k - \epsilon - f_p$  showed good agreement with measurements, implying that correct wake deficit profiles translate reasonably to wind farm power output. It was, however, also observed by the authors that the model was not able to predict correct power outputs for measurements obtained in non-neutral atmospheric stability. This highlights the need for a turbulence model that is able to correctly, and generally, predict wind turbine wake profiles for stratified atmospheres.

It is known that the standard  $k - \omega$  turbulence model suffers from the same shortcomings in wind turbine wakes as the standard  $k - \epsilon$  model [41]. However, the most common extension to this model, Menter's  $k - \omega$  shear-stress transport (SST) model [48], has proven to produce satisfactory results in numerous aeronautics application [49]. The  $k - \omega$  SST model has improved performance in adverse pressure gradient boundary layer over the baseline model, since an upper limit is placed on the stress intensity ratio, which would normally overshoot in adverse pressure gradients. Furthermore, a blending function is employed which switches to the  $k - \epsilon$  model outside of the boundary layer. The  $k - \omega$  SST model is compared by Antonini, Romero, and Amon [50] with the standard  $k - \omega$  and  $k - \epsilon$  models, as well as the Reynolds stress model. Comparisons with two experimental data set show that the  $k - \omega$  SST model has comparable performance to the more complex Reynolds stress model, unlike the standard  $k - \epsilon$  and  $k - \omega$  models. In other work, Antonini, Romero, and Amon [51] showed that wind direction uncertainty needs to be taken into account in order to make fair comparisons between RANS flow field predictions and experimental data.

Shives and Crawford [52] also tested the  $k - \omega$  SST model, as well as an extension to the model, against several cases from two experimental sites. It was found that the  $k - \omega$  SST model, although it provides satisfactory results for velocity profiles, under-predicts turbulent kinetic energy. This TKE deficit is related to the fact that tip vortices,

and the turbulence due to their breakdown in the wake, are not resolved or accounted for in actuator disc RANS simulations. The proposed  $k - \omega$  SST model extension intends to solve this issue by including a source term in the  $k$  equation. The source term only adds TKE in a specific region in the near wake, and was tuned for the test cases. The proposed model extension compares excellent to the experimental data, both in velocity deficit and in turbulence levels. The authors note, however, that tip vortex breakdown depends on the ambient turbulence intensity, and that currently the model does not account for this. Furthermore, ad hoc corrections like these likely do not generalize well.

### 3.3.3 Non-Linear Eddy-Viscosity Models

Non-linear eddy viscosity models (NLEVM) provide a more appropriate and realistic description of the Reynolds stress tensor by assuming a non-linear stress-strain relationship [53]. The Boussinesq hypothesis, eq. (3.16) can, within this framework, be seen as a leading term in a larger expansion for the Reynolds stress [6]. Pope [54] laid the foundation for NLEV modelling by generalising the eddy-viscosity hypothesis. The anisotropy tensor  $b_{ij} = \overline{u'_i u'_j} / k - \frac{2}{3} \delta_{ij}$  can be expressed as a tensor polynomial based on products of the strain rate tensor  $S_{ij}$  and the rotation rate tensor  $\Omega_{ij}$ . The complete set of ten bases tensors, expressed as  $T_{ij}^{(\lambda)}$ , is found by the generalised Cayleigh-Hamilton theorem. The tensor polynomial expression for the anisotropy tensor is given in eq. (3.20).

$$b_{ij} = \sum_{\lambda=1}^{10} c^{(\lambda)}(\eta_i) T_{ij}^{(\lambda)}(s_{ij}, \omega_{ij}) \quad (3.20)$$

The tensor bases  $T_{ij}^{(\lambda)}$  are a function of the dimensionless strain rate tensor  $s_{ij}$  and the dimensionless rotation rate tensor  $\omega_{ij}$ , and  $c^{(\lambda)}$  are the corresponding coefficients.

$$s_{ij} = \frac{1}{2} \frac{k}{\epsilon} \left( \frac{\partial U_i}{\partial x_j} + \frac{\partial U_j}{\partial x_i} \right), \quad \omega_{ij} = \frac{1}{2} \frac{k}{\epsilon} \left( \frac{\partial U_i}{\partial x_j} - \frac{\partial U_j}{\partial x_i} \right) \quad (3.21)$$

For an exact expression of the tensor bases, the reader is referred to the work of Laan, Sørensen, Réthoré, *et al.* [55].

Laan, Sørensen, Réthoré, *et al.* [55] tested two NLEVMs for several cases from an experimental site. The models tested were modified versions of the cubic NLEVM of Apsley and Leschziner [44], and the quartic NLEVM of Taulbee [56]. The non-linear stress-strain relationship allows for the formulation of anisotropic stresses. This improves the performance of non-linear models compared to linear eddy viscosity models, both in terms of stress and velocity profiles. The main drawback of the tested NLEVMs were numerical instabilities for high levels of ambient turbulence intensity and for finer grid resolutions.

### 3.3.4 Reynolds Stress Models

Reynolds stress models (RSM) circumvent the deficiencies of the Boussinesq eddy-viscosity hypothesis in a natural way and thus offer potential benefits in numerous complex flows [6], [53]. Instead of finding a relationship between the Reynolds stress and mean flow quantities, mediated by the hypothetical eddy-viscosity, RSM directly calculate the Reynolds stress from a transport equation. Cabezón, Migoya, and Crespo [42] tested such a RSM against models based on parabolic approximations to the governing equations, the standard  $k - \epsilon$  model and the Realizable  $k - \epsilon$  model of Shih, Liou, Shabbir, *et al.* [46]. All models are tested against LES data, obtained by Jimenez, Crespo, Migoya, *et al.* [57], and experimental data from the Sexbierum experiments. The tested RSM showed some improvements over the baseline in both the near wake and far wake. However, improvements were not consistent and only one case was used for testing, which brings to question generality. Besides the lack of significant improvement, RSM are rather complicated compared to LEVM, and require solving additional modelling challenges, such as that of the pressure strain correlation tensor [6].

### 3.3.5 Scalar Flux Models

The most common model for the scalar flux is the gradient diffusion hypothesis (GDH), which assumed the heat flux is aligned with the mean gradient.

$$-\overline{u'_i \theta'} = \frac{\nu_t}{Pr_t} \frac{\partial \bar{\theta}}{\partial x_i} \quad (3.22)$$

With  $Pr_t$  the turbulent Prandtl number. Other models include the generalised gradient diffusion hypothesis (GGDH) of Daly and Harlow [58], given in eq. (3.23), and the higher-order generalised gradient diffusion hypothesis (HOGGDH) of Abe and Suga [59], given in eq. (3.24).

$$-\overline{u'_i \theta'} = C'_\theta \frac{k}{\epsilon} \overline{u'_i u'_j} \frac{\partial \bar{\theta}}{\partial x_j} \quad (3.23)$$

$$-\overline{u'_i \theta'} = C''_{\theta} \frac{k}{\epsilon} \frac{\overline{u'_i u'_k u'_k u'_j}}{k} \frac{\partial \bar{\theta}}{\partial x_j} \quad (3.24)$$

With  $C'_{\theta}$  and  $C''_{\theta}$  being model constants and  $\frac{k}{\epsilon}$  an approximation to the turbulent time scale  $\tau$ . Ling, Ryan, Bodart, *et al.* [60] tested these three scalar flux models for a film cooling case. Reference LES velocity and pressure fields were used to ensure no Reynolds stress modelling errors were included in the scalar flux errors. It was found that the HOGGDG was the most accurate far from the wall, and that, generally speaking, all models had some errors close to the wall. As one would expect, the GDH was the least accurate. The errors observed close to the wall could be an indicator of similar errors occurring in the turbulent heat flux of atmospheric boundary layers.

### 3.3.6 Non-Neutral Atmospheres

Several efforts have been made to improve RANS predictions of non-neutral atmospheres. Alinot and Masson [61] made the  $C_{\epsilon,3}$ , the coefficient that governs buoyancy in the  $\epsilon$  equation, a function of the stability to enforce MOST profiles. Laan, Kelly, and Sørensen [23] recognized that the  $k$  equation is not in balance with MOST, resulting in the inlet profile changing slowly when distance is covered in the domain. To prevent this, they added a source term in the  $k$  equation. Together with a variable  $C_{\epsilon,3}$ , the modification ensures sustained MOST profiles up to 50 *km*.

Han, Liu, Xu, *et al.* [62] tested the MOST consistent turbulence model of Laan, Kelly, and Sørensen [23], as well as the turbulence models of Alinot and Masson [61] and of El-Askary, Sakr, AbdelSalam, *et al.* [63], by applying them to a wind turbine wake flow for neutral and stable conditions. The method of El Kasmi and Masson [39] is used, in addition, to overcome the issue of under-predicted wake velocity deficit. The gradient diffusion hypothesis heat flux turbulence model is used to close the energy equation in all cases, except for in the model of El-Askary, Sakr, AbdelSalam, *et al.* [63], in which the energy equation is not solved. It is found that, in stable conditions, the MOST consistency results in over-predicted surface normal velocity gradients compared to LiDAR (light detection and ranging) field measurements. Additionally, wake velocity profiles do not agree with the measurements presented from two experimental cases. The authors attribute this to the over-predicted velocity gradient. Based on these observations, the model of Laan, Kelly, and Sørensen [23] is adjusted to match the surface normal velocity gradient observed in measurements. The resulting model performs better in the near wake, but is equally inadequate in the far wake as the original models, for the first experimental case. Agreement is improved considerably in the second experimental case, but now instead for the far wake. The authors expect that these mixed results might be due to LiDAR measurement inaccuracies and the effects of complex terrain not being accounted for in the numerical simulations. This study highlights that two sets of modifications are required to the basic turbulence models in order to produce results that agree with measurements or higher fidelity data. Next to a correction aimed to improve wind turbine wake profiles, a correction is needed for ensuring turbulence model consistency with the non-neutral boundary layer profiles. Furthermore, further work is required to construct and test turbulence models that consistently match experimental and LES profiles in both the near- and far-wake under non-neutral conditions.

## 3.4 Turbine Modelling in CFD

In CFD, wind turbines can be represented with various degrees of fidelity [64]. The most physically sound representation is to directly model the rotor, nacelle and tower with a CAD model, and refine the surface mesh until sufficient resolution is obtained in the boundary layers. LES requires the mesh to be refined until the inertial sub-range. At the surfaces, this requirement results in extremely fine meshes, making this approach of direct modelling oftentimes infeasible.

Actuator line models (ALM)[65] constitute a lower fidelity method of representing wind turbines in CFD. In this method, the rotor blades are substituted by body forces which act along lines that coincide with the blades. The forces are found by assessing the local inflow velocity and direction, and by using airfoil lookup tables. Since the line coordinates generally do not coincide with the cell centre coordinates, the line body forces must be mapped to the surrounding cells. This is often done by a Gaussian function to avoid instabilities, in which  $r$  represents the distance between the line section center and the cell center, and  $\epsilon$  is a parameter which governs the width of the mapping [66].

$$\mathbf{f}_{mesh} = \frac{\mathbf{f}_{line}}{\epsilon^3 \pi^{3/2}} \exp[-(r/\epsilon)^2] \quad (3.25)$$

Actuator line models can only be used in unsteady CFD codes, since the applied body forces rotate with exactly the rotational speed of the turbine they represent. This puts an additional requirement on the maximum time-step size  $\Delta t$  besides the Courant-Friedrichs-Lewy (CFL) condition; the tip of the blade should not pass through more than a single cell over a time-step.

Actuator disc models (ADM) are a time averaged version of actuator line models in which turbines are represented by a disc that spans the swept area of the turbine blades [67]. This turbine representation is thus suitable for steady

CFD codes, such as RANS, as well as unsteady codes. The forces in ADM, which are also obtained from airfoil lookup tables, are scaled by a solidity factor  $\sigma = \frac{NA_b}{A_r}$  to account for the averaging. Here,  $N$  is the number of blades,  $A_b$  is the area of the disc section and  $A_r$  is the swept area of the turbine. The lift  $L$  and drag  $D$  of a disc section with chord  $c$  and width  $w$  is given below.

$$L = \sigma C_L(\alpha) \frac{1}{2} \rho V^2 cw \quad (3.26)$$

$$D = \sigma C_D(\alpha) \frac{1}{2} \rho v^2 cw \quad (3.27)$$

An actuator line model and actuator disc turbine model are compared in LES by Martínez Tossas, Leonardi, Churchfield, *et al.* [64]. The actuator line representation is the most physically complete, since tip and root vortices are resolved. The instantaneous flow field of the ADM matches the ALM flow field in the far wake, but not in the near wake. However, when results are time averaged, flow fields from both turbine representations agree with each other, also in the near wake. Furthermore, it is recommended to use a parameter  $\epsilon$  of twice the local grid size to avoid numerical instabilities in the solver. For the remainder of this research, Large-Eddy Simulations will be conducted with actuator disc turbine representations since (i) the computation cost is lower and (ii) the time averaged fields, which are needed for RANS model improvements, agree well with ALM.

## 3.5 Data-Driven Turbulence Modelling

Duraisamy, Iaccarino, and Xiao [14] explain that, historically, data has been used to improve turbulence models in several distinct methodologies. The first turbulence models were calibrated with experimental data in a simple manner. A set of model coefficients  $c$  were tuned until one or more outputs of the model  $\mathcal{M}(c)$  agreed sufficiently well with the measurement data  $\theta$ . Usually, measurement uncertainties were not included. Besides simple calibration, these methodologies are statistical inference and various machine learning approaches.

### 3.5.1 Statistical Inference and Uncertainty Quantification

Statistical inference, often referred to in literature as Bayesian inversion, is a more advanced method of improving models by assimilating data. This framework is entirely probabilistic, meaning that measurement uncertainties are included, and that the model coefficients are uncertain random variables. In this methodology, the modeller must first make a choice for a prior probability distribution of the model coefficients  $\mathbb{P}(c)$  based on previous studies, physical insight or on intuition. The likelihood  $\mathbb{P}(\theta|c)$  is defined as the conditional probability of the data given the prior model coefficients. The posterior  $\mathbb{P}(c|\theta)$ , defined as the probability distribution of the uncertain model coefficients given the data, is then found by Bayes' theorem.

$$\mathbb{P}(c|\theta) = \frac{\mathbb{P}(c) \cdot \mathbb{P}(\theta|c)}{\mathbb{P}(\theta)} \quad (3.28)$$

Since probability densities integrate to unity, the normalization factor  $\mathbb{P}(\theta)$  is not required. The knowledge that the posterior is proportional to the product of the prior and likelihood is sufficient. With the posterior distributions for the coefficients  $c$  inferred from the data, one can take the most likely values to obtain the *maximum a posteriori estimate* (MAP) of the coefficients [68]. If it is assumed that both the error distribution and the coefficient distribution are Gaussian of form, an explicit expressions for the MAP of the coefficients. Using the MAP coefficients in further simulations yields MAP values for the relevant output quantities. The full posterior distribution of the coefficients  $c$  can also be propagated through the model and the simulation to provide uncertainty estimations of relevant outputs.

The methods discussed thus far in this section only attempt to reduce (or quantify) uncertainty at level L4; at the level of model coefficients. Model form uncertainty thus remains unchanged, even after calibration. Emory, Pecnik, and Iaccarino [69] first introduced a method of structural uncertainty quantification which aimed to provide uncertainty bounds to output quantities directly from L2 and L3 uncertainty. In this method, the normalized anisotropy tensor is decomposed and perturbed towards various altered states but constrained under physical limits, such as the realizability constraint. Works on structural uncertainty quantification, such as these, demonstrate how basic RANS turbulence models fail in reference to experimental or higher-fidelity data.

An extended approach to statistical inference is to explicitly formulate a stochastic discrepancy function  $\delta$  as a part of the model, which represents the difference between the model output and the data. Just as with the coefficients  $c$ ,  $\delta$  needs a prior distribution and will, after the inference process, have a posterior distribution. The maximum a posteriori discrepancy function can be embedded to the calibrated model to obtain improved results. Although, this highly depends on the mathematical form of the discrepancy function the modeller chooses for the problem. Furthermore, the posterior discrepancy function is case specific and does not generalize to other cases, even if the geometry is similar.

### 3.5.2 Machine Learning

Supervised machine learning techniques have gained increasing attention in turbulence modelling literature recently. Ling, Kurzawski, and Templeton [10] first demonstrated its potential by formulating a deep neural network to model the Reynolds stress anisotropy tensor. This was achieved by utilizing the generalized eddy-viscosity hypothesis of Pope [54], who postulated a non-linear stress-strain relationship. As mentioned in section 3.3.3, the anisotropy tensor is expressed as a tensor polynomial, the basis tensors being products of the non-dimensional strain rate and rotation rate tensors. In the machine learning framework, the coefficients  $c$  in the polynomial are a layer in the neural network, and are functions of flow features  $\eta$  and the training data  $\theta$ . The five invariants of Pope's tensor bases are used as features (input) for the neural network.

$$b_{ij} = \sum_{\lambda=1}^{10} c^{(\lambda)}(\eta, \theta) T_{ij}^{(\lambda)} \quad (3.29)$$

Using Pope's Galilean invariant tensor bases  $T_{ij}^{(\lambda)}$  allows the modeller to directly embed this invariance into the resulting model. Ling et al. obtained improved Reynolds stress and mean flow predictions, as well as the prediction of secondary flow features that linear eddy viscosity models fails to predict, such as corner flow in a square duct. The authors acknowledged that the Reynolds stress tensor from DNS might not be the best choice for training for the purpose of matching RANS mean flow fields to the DNS fields.

Wu, Xiao, Sun, *et al.* [70] showed that explicit data-driven models for the Reynolds stress leads to an ill-conditioned system, especially at high Reynolds numbers. With their derived metric for conditioning, they showed that errors in ill-conditioned models are amplified to the mean flow field compared to well-conditioned models, even if the ill-conditioned models produce more accurate Reynolds stress tensors. This behaviour was observed in various data-driven turbulence modelling studies, amongst which the study of Wang, Wu, and Xiao [71], in which random forests were used to discover the model. Wu, Xiao, Sun, *et al.* [70] also report that data-driven corrections to turbulent transport equations, and machine learning of algebraic models are less affected by the issue of conditioning. Duraisamy, Iaccarino, and Xiao [14] also conclude that direct learning of DNS quantities could produce unexpected outcomes due to inconsistencies with the RANS system. They recommend, instead, to apply machine learning algorithms to learn generalized discrepancy functions with, or within, existing RANS models. The discrepancy functions can have multiple functional forms within the model. It is also possible that multiple discrepancy functions are used simultaneously. This was successfully demonstrated by Schmelzer, Dwight, and Cinnella [13], who learned algebraic corrections for the Reynolds stress anisotropy and the turbulence kinetic energy production using the  $k - \omega$  SST as baseline model.

Artificial neural networks, and deep learning in particular, have become massively popular tools in various fields of science [72]. It is no surprise that that neural networks have found their way into turbulence modelling research, as they offer great flexibility towards representing complex non-linear relations. However, flexible as they might be, they are a true black box. In the context of turbulence modelling, the model coefficients are replaced by the neural network itself. The same is true for random forest algorithms. This means it is practically impossible to extract insights out of the learned turbulence models. Symbolic data-driven models inherently overcome this limitation as they output an algebraic expressions. Weatheritt and Sandberg [11] and Weatheritt and Sandberg [12] use gene expression programming, an evolutionary algorithm, to model a new stress-strain relationship. The new learned explicit algebraic stress models are easily implemented in a solver for testing. Schmelzer, Dwight, and Cinnella [13] developed another framework for learning improved turbulence models; Sparse Regression of Turbulent Stress Anisotropy (SpaRTA). The model form error (or discrepancy) of the normalised anisotropy tensor  $b_{ij}^{\Delta}$  is defined as the difference between the reference data (DNS or LES) normalized anisotropy and the RANS model (baseline) normalized anisotropy  $b_{ij}^o = -\frac{\nu_t}{k} S_{ij}$ . This leads to a new stress-strain relationship, eq. (3.30).

$$\overline{u'_i u'_j} = 2k \left( b_{ij} + \frac{1}{3} \delta_{ij} \right) \quad (3.30)$$

$$b_{ij} = -\frac{\nu_t}{k} S_{ij} + b_{ij}^{\Delta} \quad (3.31)$$

The evaluation of the eddy-viscosity  $\nu_t$ , however, requires knowledge about the specific dissipation rate  $\omega$ . To make sure the dissipation rate is consistent with the RANS framework, the 'frozen approach' is used [73]. The dissipation equation of the baseline turbulence model is evaluated passively on the frozen LES fields, as was successfully done by Weatheritt and Sandberg [12]. Due to modelling approximations the  $k$  transport equation is not naturally consistent with the reference data. Furthermore, the inclusion of  $b_{ij}^{\Delta}$  changes the Reynolds stress, which changes the turbulent kinetic energy production  $P_k$ . An additional term  $R$  is defined as the residual of the  $k$  transport equation, to ensure full consistency with there reference data. The augmented system is solved iteratively on the frozen reference data fields until the value of  $\omega$  converges. The final value of  $b_{ij}^{\Delta}$  and  $R$  are then the model form error of the baseline  $k - \omega$  SST model. This methodology, named  $k$ -corrective-frozen-RANS, is an inexpensive alternative to the statistical inversion process described in Duraisamy, Iaccarino, and Xiao [14]. Although, unlike with statistical inversion full field reference data is required.

With the model form error known, the SpaRTA approach follows with the following four steps. (i) Building a library of candidate functions. (ii) Use logistic regression, together with sparsity promoting elastic net regularization, to find a set of unique abstract models given the candidate functions. (iii) Infer the model by least squares regression. Use additional L2-norm regularization so that the resulting models have small coefficients and convergence in CFD is better. (iv) Test inferred models by cross-validation; test the models on a case which was not used for training. In this final step, the modeller should try to find the right combination of elastic net weight and regularization type in step (ii), as well as the appropriate amount of L2-regularization in step (iii), to ensure the model does not over-fit the data and strikes the right balance between accuracy and convergence. Figure 3.1, taken from Schmelzer, Dwight, and Cinnella [13], shows a flowchart of the entire methodology. It is shown that insertion of the model form error, as optimal corrections, into the turbulence model result in a near perfect match with the mean DNS flow. Furthermore, the SpaRTA learned turbulence models show good agreement with the learning data and significant improvements over the baseline  $k - \omega$  SST model, demonstrating the potential of the method.

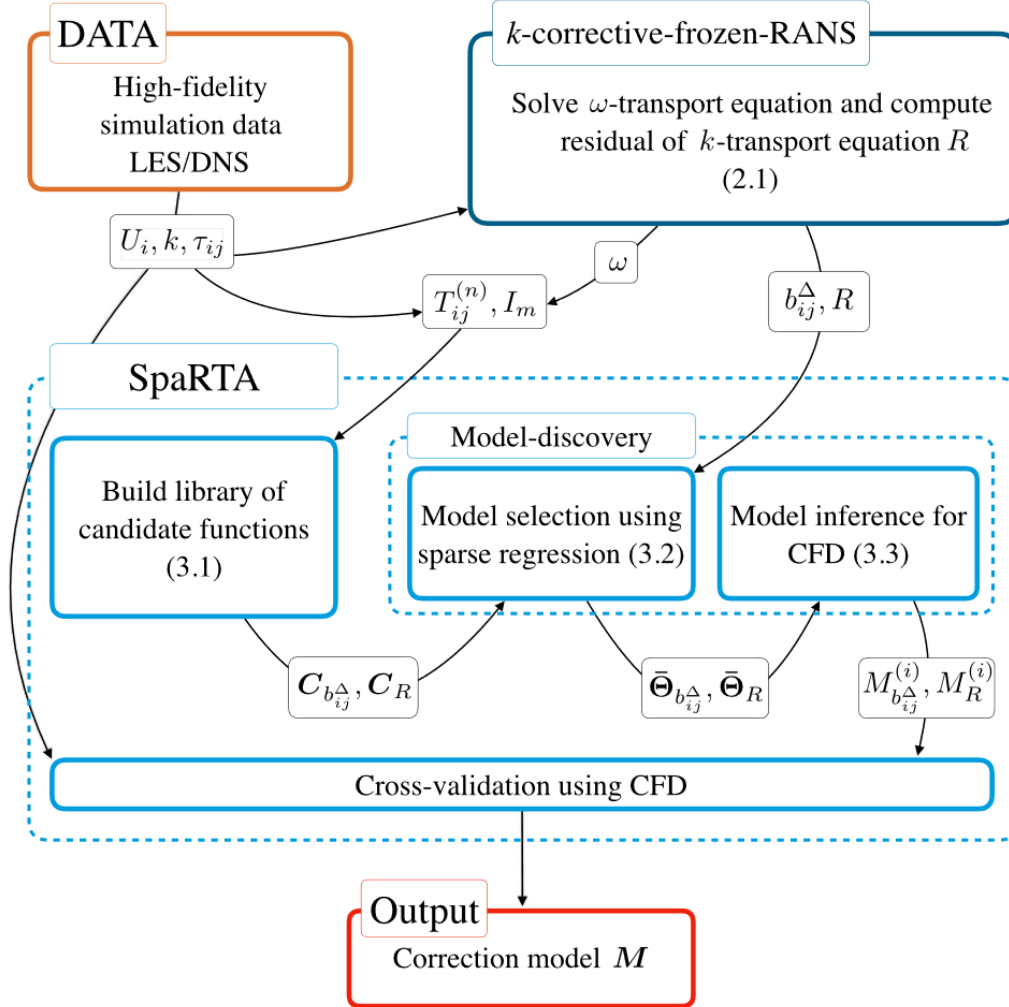
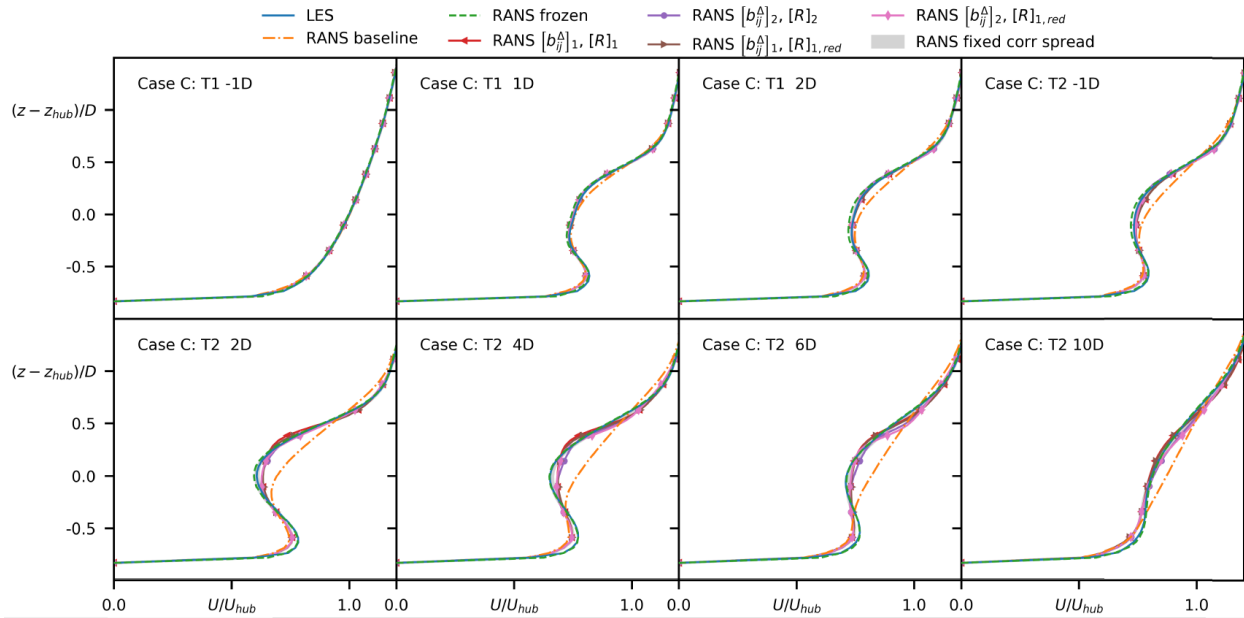
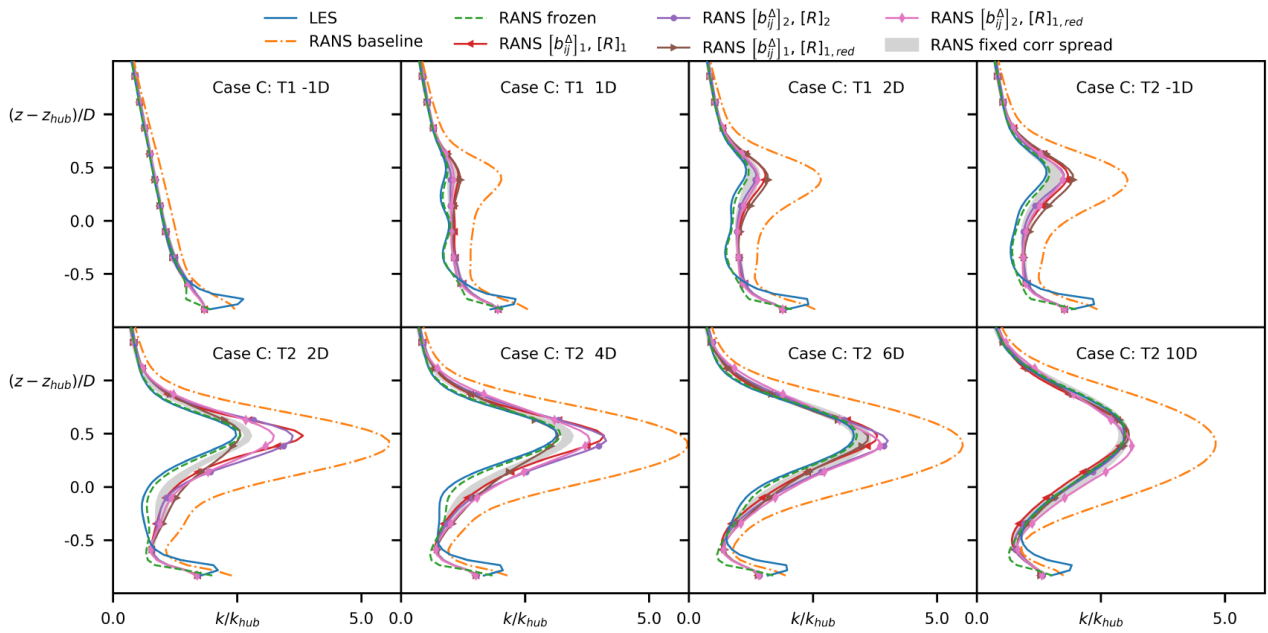


Figure 3.1: Technical flowchart of the SpaRTA (Sparse Regression of Turbulent Stress Anisotropy) methodology. Figure taken from Schmelzer, Dwight, and Cinnella [13].

The SpaRTA framework was applied to three-dimensional higher Reynolds number cases [5], [74]. Steiner, Dwight, and Viré [5] inferred turbulence models for wind turbine wake flows on wind tunnel scale. A much richer set of input features was used, in part because of the three-dimensional nature of wind turbine flows. A pre-processing step is added to the methodology, in which the number of features is reduced by assessing the mutual information a feature has with the optimal corrections. Only the set of the most important features are selected so that overall computational cost of the model discovery steps remain manageable. Stream-wise velocity profiles and TKE profiles are shown for a dual turbine constellation case in fig. 3.2a and fig. 3.2b, respectively. The second turbine (T2) is immersed in the wake of the first turbine (T1). Once again, insertion of the optimal corrections from the frozen approach resulted in wake velocity profiles that were consistent with the LES reference data. The learned models showed significant improvements over the baseline  $k - \epsilon$  model. This is a significant result, since  $k - \epsilon$  and other basic turbulence models fail to accurately predict wind turbine wake flows, as discussed in detail in section 3.3.1. The others note that a few of the obtained models were unstable, highlighting the importance of appropriate model selection.



(a) Stream-wise velocity



(b) Turbulent kinetic energy

Figure 3.2: Comparison between the LES reference data, the baseline RANS model, the frozen-RANS predictions and the corrected models for a dual turbine constellation. Figure taken from Steiner, Dwight, and Viré [5].

Future work includes understanding these abilities, considering non-neutral atmospheric stability and industrial scale flows. In summary, learning of algebraic models using SpaRTA has potential because there are less issues with model conditioning [70]. Furthermore, the models can be interpreted to gain physical insights, they can be tweaked to improve numerical stability and they are easily implemented in CFD solvers.

Errors in the Reynolds stress propagates to uncertainty the scalar-flux by two mechanisms; altering the mean flow and altering the input for the scalar flux model [75]. Besides this effect, in heated flows, error in the scalar-flux model is propagated back to the mean flow by buoyancy related terms in the momentum equation and in the turbulent transport equation. Machine learning was first used in scalar-flux modelling to learn the values of model coefficients [76], [77]. Weatheritt, Zhao, Sandberg, *et al.* [15] first generalized the scalar fluxed itself, based on not only the Reynolds stress and temperature gradient, but also on invariants of the strain and rotation rate tensors. The alignment of the basis vectors with the reference scalar-flux is checked a priori, since well aligned bases are required in order to produce an satisfactory model. It was found that no particular basis vector had good alignment everywhere, justifying the approach of data-driven model inference from multiple basis vectors and enabling the reduction of the number of bases. The resulting algebraic scalar flux models outperformed the gradient-diffusion hypothesis in all test cases in terms of heat flux. The resulting velocity profiles are not reported. In a similar study, Milani, Ling, and Eaton [16] successfully implemented the tensor bases neural network to the scalar-flux [10], also in the jet in cross-flow case. The model was not coupled to a RANS solver but rather applied to the LES fields to predict the heat-flux. Although data-driven modelling of the heat-flux is still very much in its infancy, good potential is demonstrated in the mentioned studies by improving the scalar flux predictions. There is still a gap however; it is not clear how the accuracy of the mean flow field improves when data-driven models are applied to both the Reynolds stress and scalar-flux simultaneously.

## 4.1 Large-Eddy Simulations

In the present thesis, three cases are used to demonstrate the methodology: the neutral boundary layer (NBL) case, the convective boundary layer (CBL) and the stable boundary layer (SBL) case. This section presents the methodology for running Large-Eddy Simulations in SOWFA-6 to generate reference data on these cases.

### 4.1.1 Case Definitions

The general strategy for generating high-quality reference data is to first develop the LES setup and methodology by validation against scientific literature for non-neutral atmospheric boundary layer flows. Firstly, the GEWEX Atmospheric Boundary Layer Study (GABLS) [78] is selected for validating the SBL case setup. This inter-comparison study contains data from multiple participants and thereby offers a range of output values. Secondly, the unstably stratified case of Abkar and Moin [79] is used for the validation of the CBL. Finally, all cases are validated against the analytical log-law for rough wall atmospheric boundary layer flows, eq. (2.7).

The general case parameters of the SBL case and CBL case are the same as those presented in the validation literature. The NBL case is a modification of the SBL case. Only the initial temperature condition and wall temperature flux are modified such that stable conditions are maintained in the NBL case simulations. The general case parameters are summarized in table 4.1.

Table 4.1: General parameters and conditions used in the LES cases

	NBL	SBL	CBL
Reference density $\rho_0$ [ $kg/m^3$ ]	1.225	1.225	1.225
Prandtl number $Pr$	0.7	0.7	0.7
Kinematic viscosity $\nu$ [ $m^2/s$ ]	1.569E-5	1.569E-5	1.569E-5
Reference potential temperature $\theta_0$ [ $K$ ]	263.5	263.5	301.78
Von Kármán constant $\kappa$	0.4	0.4	0.4
Latitude $\phi$ [ $^\circ$ ]	73.0	73.0	43.36
Earth's rotation period $P$ [ $hr$ ]	24	24	24
Roughness length $z_0$ [ $m$ ]	0.1	0.1	0.16

### 4.1.2 Governing Equations

The governing LES equations solved in SOWFA-6 are given in eq. (4.1), eq. (4.2) and eq. (4.3).

$$\frac{\partial \tilde{u}_i}{\partial x_i} = 0 \quad (4.1)$$

$$\frac{\partial \tilde{u}_i}{\partial t} + \frac{\partial \tilde{u}_i \tilde{u}_j}{\partial x_j} = -\frac{1}{\rho_0} \frac{\partial \tilde{p}}{\partial x_i} + \frac{\partial}{\partial x_j} \left( \nu \frac{\partial \tilde{u}_i}{\partial x_j} - \tau_{ij}^{SGS} - \tau_{w,ij} \right) + \left( \frac{\tilde{\theta} - \theta_0}{\theta_0} \right) g_i - 2\epsilon_{i3k} \Omega_3 \tilde{u}_k + S_i + \frac{1}{\rho_0} f_i^T \quad (4.2)$$

In the SOWFA-6 formulation,  $\frac{1}{\rho_0} \frac{\partial \tilde{p}}{\partial x_i}$  is the density normalized pressure gradient as deviation from the hydrostatic component and the mean horizontal pressure gradient. The wall stress is enforced by adding the term  $\tau_{w,ij}$ .  $S_i$  is the momentum source term. Theoretically, it is the horizontal mean pressure gradient that drives the flow. Practically, its value is controlled such that the horizontal mean wind speed is constant at a certain reference height. Furthermore,

$\Omega_3 = \frac{2\pi}{P \cdot 3600} \sin(\phi)$  with  $P$  Earth's rate of rotation and  $\phi$  the latitude. Finally, turbine actuator forces are represented by  $f_i^T$ .

$$\frac{\partial \tilde{\theta}}{\partial t} + \frac{\partial \tilde{\theta} \tilde{u}_j}{\partial x_j} = \frac{\partial}{\partial x_j} \left( \frac{\nu}{Pr} \frac{\partial \tilde{\theta}}{\partial x_j} + q_{w,j} - q_j^{SGS} \right) \quad (4.3)$$

As was done with the wall stress in eq. (4.2), the wall heat flux is added as the source term  $q_{w,j}$ .

As is standardly implemented in SOWFA-6, the sub-grid scale turbulent fluxes are parameterized with the one equation Deardoff model for planetary boundary layer flows [80], [81]. This model assumes a stability dependant sub-grid length scale  $l$  which is a function of stability. The value of  $l$  decreases for stably stratified conditions to include the effect of turbulence suppression.

$$l = \min \left( \Delta, 0.76 \sqrt{k_{SGS}} \left( \frac{\partial \tilde{\theta}}{\partial x_i} \frac{g_i}{\theta_0} \right)^{-1/2} \right) \quad (4.4)$$

The local grid size  $\Delta$  is computed as the cube root of the volume of the respective cell and  $k_{SGS}$  is the sub-grid scale turbulent kinetic energy, which is governed by a transport equation. The formulation for the SGS eddy viscosity is shown in eq. (4.5).

$$\nu_{SGS} = l C_k \sqrt{k_{SGS}} \quad (4.5)$$

The model coefficient  $C_k = 0.1$ , whereas the coefficient  $C_e = 0.19 + 0.74 \frac{l}{\Delta}$ , such that its  $C_e = 0.93$  when  $l = \Delta$  for neutral or unstable conditions [82]. For the SGS heat flux, the gradient diffusion hypothesis model is used. Equation (4.6) and eq. (4.7) show the corresponding expressions.

$$q_j^{SGS} = - \frac{\nu_{SGS}}{Pr_{SGS}} \left( \frac{\partial \tilde{\theta}}{\partial x_j} \right) \quad (4.6)$$

$$Pr_{SGS} = \left( 1 + \frac{2l}{\Delta} \right)^{-1} \quad (4.7)$$

### 4.1.3 Numerical Schemes

The differential operators in eq. (4.1), eq. (4.2) and eq. (4.3) are discretized with second-order finite volumes schemes. Table 4.2 summarizes which schemes are used for which operators. An additional constraint on the time-marching is that the CFL number does not exceed 0.75.

Table 4.2: Finite volume schemes for LES solver

Operator	Scheme	Order
$\frac{\partial}{\partial t}$ (time)	CrankNicolson 0.9	second
$\nabla$ (gradient)	Gauss linear	second
$\nabla \cdot$ (divergence)	$\tilde{u}_i, \tilde{\theta}$ : Gauss localBlended linear upwind Remaining: Gauss linear	second second
$\nabla^2$ (Laplacian)	Gauss linear corrected	second
Surface-normal gradient	corrected	second

### 4.1.4 Precursor-Successor Approach

The governing equations are solved on a rectangular domain in which the air flows from the west face to the east face. The precursor-successor approach is used to generate realistic turbulent conditions at the west boundary [83]. In the precursor stage of the simulation, no wind turbines are present in the domain. The west and east boundaries as well as the north and south boundaries are connected by cyclic boundary conditions. The flow is driven by the momentum source term  $S_i$  which is controlled to maintain a constant horizontal velocity at a reference height. The simulation is continued until turbulence has developed fully. From this point onwards, the flow is said to be statistically stationary and boundary plane data of the west boundary is collected at every time step until the end of the precursor simulation.

In the successor stage of the simulation, the wind turbines are present in the domain and the west and east boundaries become inflow and outflow boundaries. The inflow conditions at the west boundary are prescribed from the boundary planes saved during the precursor stage. The driving momentum source term  $S_i$  during the successor stage is set as the mean of the precursor momentum source. A schematic of the precursor-successor concept is shown in fig. 4.1 [83].

In chapter 5, it will be shown how the present LES framework is developed and validation against literature. It is important to note that the validation cases are similar to the precursor stage, as the west and east boundaries are

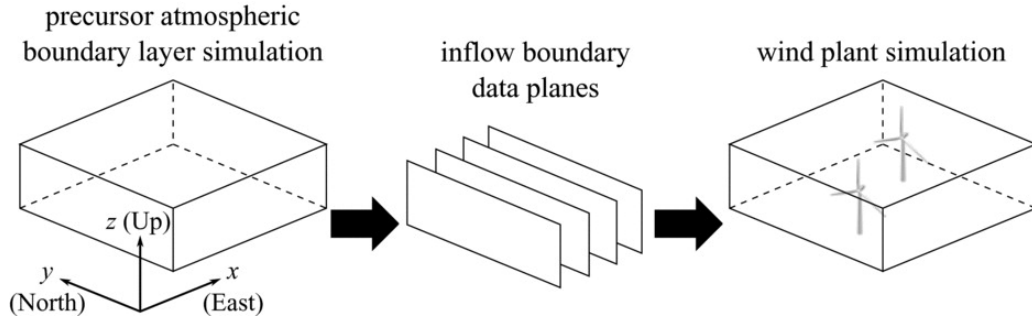


Figure 4.1: Schematic of the precursor-successor approach to providing inflow conditions for wind turbine flows. The figure is obtained from Matthew J. Churchfield, Lee, Michalakes, *et al.* [83].

connected by cyclic boundary conditions and no wind turbines are present in the domain. However, the precursor stages of the final turbine simulations vary slightly from the validation case in the wind direction. In the precursor, the momentum source is always controlled such that the hub-height velocity as a zero lateral component (i.e.  $V_{hub} = 0$ ) so that the flow is generally aligned with the coordinate axis and flows from west to east. For the validation cases, however, the momentum source is controlled such that the geostrophic wind speed matches the values reported in the literature used for validation, resulting in a generally non-zero lateral wind speed at hub-height.

### Simulation time and Statistical Stationarity

The simulation validation cases are kept the same as in the reference literature; 2.5 *hr* for the CBL case and 9 *hr* for the SBL case. The precursor cases last 1.5 *hr* longer than the validation case so that the boundary plane data can be collected during this period. For the NBL case, the precursor is run for 6.5 *hr* of total simulation time. With this time, the case is statistically stationary for at least the final 1.5 *hr*, meaning the friction velocity  $u_*$  and mean forcing no longer change. All successor cases run for the 1.5 *hr* that coincides with the collection of boundary plane data in the respective precursor stage.

The main output for the Large-Eddy Simulations are the time-averaged statistics such as the mean velocity field, Reynolds stress tensor and turbulent heat flux. In all precursor and successor cases, these statistics are obtained by averaging over the very final hour of simulation time using data from every timestep.

## 4.1.5 Initial Conditions

### Precursor stage

For all three precursor cases, the velocity field is initialized as a uniform which is equal to geostrophic velocity, which was  $U_i = (9, 0, 0)$  *m/s* for the NBL case and the SBL case, and  $U_i = (10, 0, 0)$  *m/s* for the CBL case. Additionally, the velocity in the stream-wise and span-wise direction,  $U$  and  $V$ , are perturbed so that the development of turbulence is promoted.

The initial condition for the potential temperature is  $\theta$ , together with the wall heat flux, the determining factor for atmospheric stability in a Large-Eddy Simulation. For the NBL case, the initial temperature is uniform with a value equal to the reference potential temperature  $\theta_0$ . The initial potential temperature conditions for the CBL and SBL are set according to Abkar and Moin [79] and Beare, Macvean, Holtslag, *et al.* [78], respectively. The initial condition is a function height  $z$  only, as shown in fig. 4.2. In the CBL case, the  $\theta = 300$  *K* until  $z = 937$  *m*, after which there is a strong capping inversion in which the temperature rises \* *K* in 126 *m*. Above the capping inversion, the temperature rises with 3 *K/km*. The strong capping inversion effectively sets the height of the initial boundary layer by suppressing turbulence locally. For the SBL case, the  $\theta = 265$  *K* until  $z = 100$  *m*, after which it rises with 1 *K/km*.

The initial condition for SGS kinetic energy is set as uniform  $k_{SGS} = 0.5$  *m*<sup>2</sup>/*s*<sup>2</sup> for all three cases. Finally, the initial condition for the SGS eddy viscosity is set as uniform  $\nu_{SGS} = 0$  *m*<sup>2</sup>/*s*.

### Successor Stage

For the initial conditions of the successor stage, the usual approach is to use the instantaneous field data from the precursor case. This field data should be taken at the time in the precursor at which the successor starts and boundary data is collected for inflow. However, in the present LES setup, the precursor domain and mesh are generally not the same as those of the successor, as explained in section 4.1.8. The alternative approach used here is to first take planar averages for the velocity and temperature of the precursor field. These planar averages are then written to successor case. The downside of this method is the lack of proper turbulence in the initial conditions, as is particularly visible in

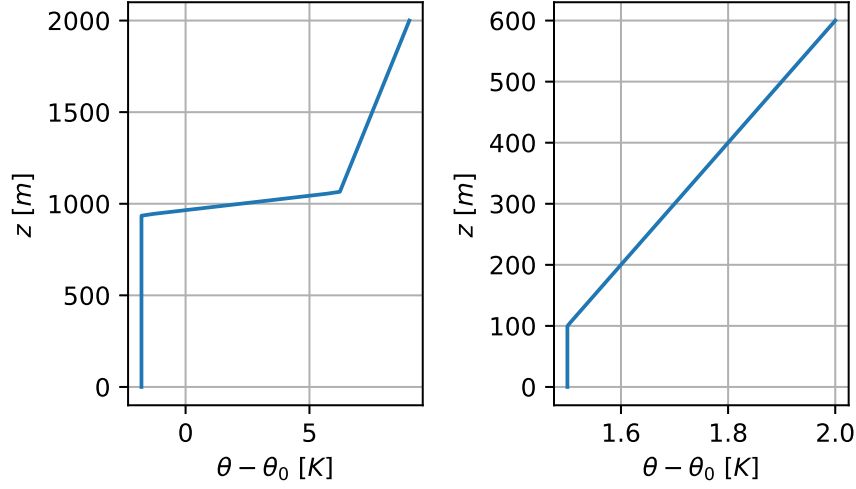


Figure 4.2: Initial conditions for the potential temperature  $\theta$  for the CBL case (left) and the SBL case (right)

the velocity field. However, as will be shown in section 5.4, turbulence is still propagated through the domain due to the turbulent inflow conditions, and the flow reaches statistical stationarity relatively quickly. Similarly to the precursor stage, the SGS kinetic energy and SGS eddy viscosity are initialized as  $k_{SGS} = 0.5 \text{ m}^2/\text{s}^2$  and  $\nu_{SGS} = 0 \text{ m}^2/\text{s}$ .

#### 4.1.6 Boundary Conditions

The Schumann-Grötzbach boundary condition is used for the wall stress at the lower boundary. This model relates the local instantaneous wall shear stress  $\tau_{i3}$  to rough wall ABL log-law from Monin-Obukhov similarity theory.

$$\tau_w = u_*^2 = \left( \frac{\langle u_r \rangle \kappa}{\ln(z/z_0) - \Psi_m} \right)^2 \quad (4.8)$$

$$\tau_{i3} = -\frac{\tilde{u}_i}{\langle u_r \rangle} \tau_w, \quad i = 1, 2 \quad (4.9)$$

The wall parallel velocity is given by  $u_r = \sqrt{\tilde{u}_1^2 + \tilde{u}_2^2}$ , and  $\langle \dots \rangle$  indicates the planar average operator. For the determination of the stability dependant term  $\Psi_m$ , which was defined in eq. (2.10) and eq. (2.9), the Monin-Obukhov coefficients  $\beta = 4.9$  and  $\gamma_1 = 15$  are used.

Next to the Schumann-Grötzbach boundary condition for the wall stress, it is customary to use the no-slip boundary condition for the velocity at the lower wall. Although this is possible, it is recommended in default SOWFA-6 to use boundary condition `velocityABLWallFunction`. This boundary condition sets the velocity at the first cell off the wall such that the wall-normal velocity gradient at the wall is equal to the wall-normal velocity gradient at the top face of the first cell. The purpose of this is to supply a proper vertical velocity gradient to the SGS model. As shown in section 5.1, `velocityABLWallFunction` produces better stress results for the present setup. As such, the condition is used for the NBL and SBL cases. In section 5.2 it is shown that the no-slip condition must be used for the CBL case.

For the wall heat flux, a fixed uniform value of  $q_w = 0.24 \text{ Km/s}$  is used for the CBL case, while a constant temperature change of  $-0.25 \text{ K/h}$  is prescribed for the SBL case, starting from  $265 \text{ K}$  at the start of the simulation. Given the surface temperature, the instantaneous heat flux is computed using the `fixedHeatingRate` boundary condition which evaluates the following expression.

$$q_w = \frac{\kappa u_* \Delta\theta}{\sigma_\theta \ln\left(\frac{z}{z_0}\right) - \psi_h} \quad (4.10)$$

Here,  $\Delta\theta$  is the temperature difference between the surface and the fluid at the first cell,  $\Psi_h$  is the Monin-Obukhov function for the heat flux with the coefficients for its determination being  $\sigma_\theta = 1$  and  $\gamma_2 = 9$ .

All other boundary conditions are listed in table 4.3 for the precursor stage and table 4.4 for the successor stage. The value corresponding to a fixed value or gradient boundary condition is indicated as well. Note that `timeVaryingMappedFixedValue` represent the boundary condition that reads and applies the boundary plane data from the precursor stage.

Table 4.3: Boundary conditions of the LES precursor cases under neutral (N), stable (S) and unstable (U) conditions

		Lower	Upper	West	South	East	North
$\tilde{u}_i$	N	velocityABLWallFunction	slip	cyclic	cyclic	cyclic	cyclic
	S	velocityABLWallFunction					
	U	noSlip					
$\tilde{p}$		fixedFluxPressure	fixedFluxPressure	cyclic	cyclic	cyclic	cyclic
$\tilde{\theta}$	N	zeroGradient	zeroGradient	cyclic	cyclic	cyclic	cyclic
	S		fixedGradient 0.003				
	U		fixedGradient 0.001				
$\tau_w$		SchumannGrotzbach	fixedValue 0	cyclic	cyclic	cyclic	cyclic
$q_w$	N	fixedValue 0	fixedValue 0	cyclic	cyclic	cyclic	cyclic
	S	fixedHeatingRate					
	U	fixedValue $q_w$					
$\nu_{SGS}$		fixedValue 0	fixedValue 0	cyclic	cyclic	cyclic	cyclic
$k_{SGS}$		zeroGradient	zeroGradient	cyclic	cyclic	cyclic	cyclic

Table 4.4: Boundary conditions of the LES successor cases under neutral (N), stable (S) and unstable (U) conditions

	Lower	Upper	West	South	East	North
$\tilde{u}_i$	N	velocityABLWallFunction				
	S	velocityABLWallFunction	timeVaryingMappedFixedValue	cyclic	inletOutlet	cyclic
	U	noSlip				
$\tilde{p}$		fixedFluxPressure	fixedFluxPressure	cyclic	zeroGradient	cyclic
	N		zeroGradient			
	S	zeroGradient	fixedGradient 0.001	cyclic	zeroGradient	cyclic
$\tilde{\theta}$	U		fixedGradient 0.003			
		SchumannGrotzbach	fixedValue 0	cyclic	fixedValue 0	cyclic
	N	fixedValue 0				
$q_w$	S	fixedHeatingRate	fixedValue 0	cyclic	fixedValue 0	cyclic
	U	fixedValue $q_w$				
		fixedValue 0	zeroGradient	cyclic	zeroGradient	cyclic
$\nu_{SGS}$	zeroGradient	zeroGradient	zeroGradient	cyclic	zeroGradient	cyclic
$k_{SGS}$				cyclic	zeroGradient	cyclic

## 4.1.7 Turbine Representation

For the turbine, the NREL 5 MW Reference Turbine is used [84]. This three-bladed upwind turbine is representative of modern industrial-scale off-shore wind turbines. As described in section 3.4, the actuator disc model (ADM) is the preferred method for wind turbine parameterization over the actuator line model (ALM) in the LES cases for the present study. The primary reason for this is the significantly lower computational cost required coupled with a comparable accuracy for the time-averaged fields, which are our main quantities of interest in the LES cases. In the Large-Eddy Simulations, the wind turbine power production is controlled by two independent basic control systems: the generator-torque controller and the collective rotor blade pitch controller. The generator torque controller effectively controls the rotational speed of the wind turbine and is mostly active below the rated operating point where power production is maximized. The blade pitch controller is active above rated speed such that power production is limited. A detailed description of the parameters of the two control systems can be found in the NREL technical report[84].

## 4.1.8 Domain and Mesh

The LES equations are solved on a rectangular domain with sizes as shown in table 4.5. For the precursor NBL and SBL cases, the domain size is reduced in stream-wise length to save computational cost. For the CBL case, the domain is large to allow large convective eddies to form.

Table 4.5: Domain size  $L_x \cdot L_y \cdot L_z$  for the LES precursor and successor stages

	NBL	CBL	SBL
Precursor	800 m · 800 m · 800 m	5000 m · 2000 m · 2000 m	600 m · 600 m · 600 m
Successor	2000 m · 800 m · 800 m	5000 m · 2000 m · 2000 m	2000 m · 600 m · 600 m

For actuator disc turbine representations, 25 grid cells are required per rotor diameter [85]. This translates to a mesh resolution of 5 m at the turbine. As such, the NBL and SBL case mesh resolution  $\Delta_x \cdot \Delta_y \cdot \Delta_z$  is set as 5 m · 5 m · 5 m below  $z = 200$  m and is coarsened to 10 m · 10 m · 10 m above  $z = 200$  m. For the convective boundary layer, multiple refinement zones are used to limit the total cell count for such a large domain. The mesh definitions are presented in table 4.6.

Table 4.6: Mesh resolution and refinement zones for the CBL precursor case

		$\Delta_x$ [m]	$\Delta_y$ [m]	$\Delta_z$ [m]	position $x$ [m]	position $y$ [m]	position $z$ [m]
precursor	Background	100	100	40	-	-	-
	Refinement 1	50	50	20	$0 \leq x \leq 2000$	$0 \leq y \leq 2000$	$0 \leq z < 1500$
successor	Background	100	40	40	-	-	-
	Refinement 1	50	20	20	$0 \leq x \leq 2000$	$0 \leq y \leq 2000$	$0 \leq z < 1500$
	Refinement 2	25	10	10	$0 \leq x < 2640$	$685 < y < 1315$	$0 \leq z < 504$
	Refinement 3	12.5	5	5	$0 \leq x < 2010$	$811 < y < 1189$	$0 \leq z < 378$

## 4.2 Frozen-RANS

The goal of the frozen-RANS method is to find the model-form errors between a baseline RANS turbulence model and time-averaged high fidelity reference data. These errors are postulated where the baseline RANS model is known to suffer from simplifying assumptions, and such that the RANS model becomes consistent with the reference data. For selecting the baseline model, it is convenient to choose simple and commonly used models. This allows us to gain insight into the failure mechanisms of these models and leverage fast convergence rates during the simulations. The latter is not only important now, but also, particularly when machine learning techniques are used to generalize the frozen-RANS corrections, and when these models are applied to novel cases. Furthermore, in order to demonstrate the novel frozen-RANS framework, the complexity of the baseline model is an arbitrary matter beyond computational time.

### 4.2.1 Baseline $k - \epsilon$ model

For the baseline model, the requirements are that atmospheric stratification is considered. The basic  $k - \epsilon$  model described of Duynkerke [86] and Wyngaard [87] is selected. More sophisticated  $k - \epsilon$  models do exist for the stratified ABL, such as the model of Koblitz [88]. However, to demonstrate the novel frozen approach a simple model is sufficient. The transport equations of the selected model are given in eq. (4.11) and eq. (4.12).

$$\frac{Dk}{Dt} = P_k + B - \epsilon + \frac{\partial}{\partial x_j} \left[ \left( \nu + \frac{\nu_t}{\sigma_k} \right) \frac{\partial k}{\partial x_j} \right] \quad (4.11)$$

$$\frac{D\epsilon}{Dt} = \frac{\epsilon}{k} \left( C_{\epsilon 1} P_k - C_{\epsilon 2} \epsilon + C_{\epsilon 3} B + C_{\epsilon 4} \frac{B^2}{\epsilon} \right) + \frac{\partial}{\partial x_j} \left[ \left( \nu + \frac{\nu_t}{\sigma_\epsilon} \right) \frac{\partial \epsilon}{\partial x_j} \right] \quad (4.12)$$

The model coefficients are a function of atmospheric stratification. For the neutral case,  $C_{\epsilon 3} = C_{\epsilon 4} = 0$ , since there are no temperature variations. For the unstable case,  $C_{\epsilon 3} = C_{\epsilon 1}$  and  $C_{\epsilon 4} = 0$ . For the stable case  $C_{\epsilon 3} = 0.5$  and  $C_{\epsilon 4} = 1.0$ . For the other model coefficients standard values for ABL flows are used [89]. All standard model coefficients are summarised in table 4.7

Table 4.7: Standard model coefficients for the selected  $k - \epsilon$  ABL model, under neutral, stable and unstable conditions

	$C_\mu$	$C_{\epsilon,1}$	$C_{\epsilon,2}$	$C_{\epsilon,3}$	$C_{\epsilon,4}$	$\sigma_k$	$\sigma_\epsilon$
$k - \epsilon$ ABL neutral	0.03	1.21	1.92	0	0	1.00	1.30
$k - \epsilon$ ABL stable	0.03	1.21	1.92	0.5	1	1.00	1.30
$k - \epsilon$ ABL unstable	0.03	1.21	1.92	1.21	0	1.00	1.30

For the turbulent heat flux, the gradient diffusion hypothesis model, eq. (3.22), is used as this is the most common and simple model.

$$-\overline{u'_i \theta'} = \frac{\nu_t}{Pr_t} \frac{\partial \bar{\theta}}{\partial x_i}$$

$Pr_t = 0.85$  is used in all frozen-RANS and RANS cases since Li [90] have shown that the turbulent Prandtl number asymptotically reaches this value for the large Peclet numbers observed in the atmospheric boundary layer.

## 4.2.2 Postulation of model-form error

With the baseline model known, the model-form error can be postulated. With the addition of this error in the model, the complete RANS and turbulence model equations become fully consistent with the time-averaged LES reference system. In terms of terminology, an unknown error is usually referred to as uncertainty, while a known error can be corrected for. Since the frozen-RANS approach derives exact known model-form errors, the term model-form error is often interchanged with the term correction. The corrections are postulated in the Reynolds stress anisotropy, the turbulent kinetic energy transport equation, and in the current framework, in the turbulent heat flux.

### Normalised anisotropy error

Following Weatheritt and Sandberg [12], a correction to the normalised Reynolds stress anisotropy  $b_{ij}^\Delta$  is defined in eq. (4.13).

$$b_{ij} = \frac{\overline{u'_i u'_j} - \frac{2}{3} k \delta_{ij}}{2k} = b_{ij}^{Boussinesq} + b_{ij}^\Delta = \frac{-2\nu_t S_{ij}}{2k} + b_{ij}^\Delta \quad (4.13)$$

The change to the normalised anisotropy impacts the RANS model directly at the Boussinesq hypothesis since the term  $b_{ij}^{Boussinesq}$  is normally an approximating model for  $b_{ij}$ . Additionally, the change impacts the expression for the shear production of turbulence in the  $k$  and  $\epsilon$  transport equations.

$$P_k = -\overline{u'_i u'_j} \frac{\partial U_i}{\partial x_j} = P_k^{Boussinesq} + P_k^\Delta = 2\nu_t S_{ij} \frac{\partial U_i}{\partial x_j} - 2k b_{ij}^\Delta \frac{\partial U_i}{\partial x_j}$$

### Transport equation residual

As shown by Schmelzer, Dwight, and Cinnella [13], the  $k$ -transport equation is not exactly satisfied on mean LES fields, even with the addition of the correction term  $b_{ij}^\Delta$ . As such a residual  $R$  to the  $k$  transport equation is needed for the RANS system to be consistent with LES.

$$\frac{Dk}{Dt} = P_k + R + B - \epsilon + \frac{\partial}{\partial x_j} \left[ \left( \nu + \frac{\nu_t}{\sigma_k} \right) \frac{\partial k}{\partial x_j} \right] \quad (4.14)$$

The  $k$  transport equation residual  $R$  can be considered as an additional term for turbulence production or destruction inside the transport equation. As such,  $R$  also appears in the  $\epsilon$  transport equation.

$$\frac{D\epsilon}{Dt} = \frac{\epsilon}{k} \left( C_{\epsilon 1} (P_k + R) - C_{\epsilon 2} \epsilon + C_{\epsilon 3} B + C_{\epsilon 4} \frac{B^2}{\epsilon} \right) + \frac{\partial}{\partial x_j} \left[ \left( \nu + \frac{\nu_t}{\sigma_\epsilon} \right) \frac{\partial \epsilon}{\partial x_j} \right] \quad (4.15)$$

## Turbulent heat flux error

In the scalar transport equation for the potential temperature eq. (3.15), the unknown turbulent heat flux  $\overline{u'_j \theta'}$  is modelled by the Gradient-Diffusion Hypothesis (GDH). Equation (4.16) shows how the turbulent heat flux error  $q_j^\Delta$  is defined as the difference between the GDH value and the LES value.

$$\overline{\theta' u'_j} = q_j^{GDH} + q_j^\Delta = -\frac{\nu_t}{Pr_t} \frac{\partial \Theta}{\partial x_j} + q_j^\Delta \quad (4.16)$$

With the addition of the turbulent heat flux error,  $q_j^\Delta$ , the scalar transport equation for potential temperature becomes the expression given in eq. (4.17).

$$\frac{\partial \Theta U_j}{\partial x_j} = \frac{\partial}{\partial x_j} \left[ \left( \frac{\nu}{Pr} + \frac{\nu_t}{Pr_t} \right) \frac{\partial \Theta}{\partial x_j} \right] - \frac{\partial q_j^\Delta}{\partial x_j} \quad (4.17)$$

Additionally to the altered form of the potential temperature transport equation, the expression for the buoyant production of turbulence in the  $k$  and  $\epsilon$  transport equations change as shown below. The gravitational vector used is  $g_j = (0, 0, -9.81)$ .

$$B = \frac{g_j \overline{u'_j \theta'}}{\theta_0} = B^{GDH} + B^\Delta = \frac{g_j}{\theta_0} \frac{\nu_t}{Pr_t} \frac{\partial \Theta}{\partial x_j} - \frac{g_j}{\theta_0} q_j^\Delta$$

## 4.2.3 Algorithm Description

In order for the corrections  $R$ ,  $b_{ij}^\Delta$  and  $q_j^\Delta$  to be calculated, the fields for  $\nu_t$  and  $\epsilon$  are required. The  $k - \epsilon$  equations with corrections are iteratively solved on the frozen LES fields to do so. Figure 4.3 shows the flow of the algorithm. First, all variables that are known or calculated from LES are loaded in and *frozen*, meaning they are not updated or recalculated throughout the process. Frozen variables are indicated with an asterisk. After all corrections and  $\epsilon$  are initialized as zero, and  $\nu_t$  is initialized with  $10^{-5}$ , the main loop is started. The turbulence production terms are calculated, including the effect of the normalised anisotropy correction  $b_{ij}^\Delta$  and the heat flux correction  $q_j^\Delta$ . The epsilon equation is evaluated to update  $\epsilon$ , after which  $\nu_t$  is updated. Finally, the values for all corrections are updated. The process is repeated until the residual for epsilon drops below  $10^{-10}$ .

## 4.2.4 Numerical Schemes

The numerical schemes for the froze-RANS approach are the same as those of the RANS simulation. The used schemes are shown in table 4.8.

Table 4.8: Finite volume schemes for RANS and frozen-RANS solvers

Operator	Scheme	Order
$\frac{\partial}{\partial t}$ (time)	steadyState	-
$\nabla$ (gradient)	$U_i, \Theta$ : cellLimited Gauss linear 1.0 Remaining: Gauss linear	second second
$\nabla \cdot$ (divergence)	$U_i$ : bounded Gauss linearUpwindV $\Theta$ : bounded Gauss linearUpwind $k, \epsilon, R$ : bounded Gauss upwind Remaining: Gauss linear	second second first second
$\nabla^2$ (Laplacian)	Gauss linear corrected	second
Surface-normal gradient	corrected	second

## 4.2.5 Boundary Conditions

In OpenFOAM-6, the wall stress in typical neutral ABL RANS simulations is set by the  $\nu_t$  nutkAtmRoughWallFunction. The boundary condition is adapted to include the effects of atmospheric stratification in the ABL log-law by adding the integrated Monin-Obukhov function  $\Psi_m$ . The modified expressions, now represented by the boundary condition nutkStratAtmRoughWallFunction, are shown in eq. (4.18). The condition is used in all present frozen-RANS and RANS simulations. All other boundary conditions for the frozen-RANS method are shown in table 4.9.

$$\tau_w / \rho = \nu \frac{\partial U}{\partial z} \Big|_{wall} = u_*^2 = u_* \frac{U_1 \kappa}{\left[ \log\left(\frac{z_1}{z_0}\right) - \Psi_m \right]} = C_\mu^{1/4} \sqrt{k} \frac{U_1 \kappa}{\left[ \log\left(\frac{z_1}{z_0}\right) - \Psi_m \right]} \cong (\nu + \nu_t) \frac{U_1}{z_1} \quad (4.18)$$

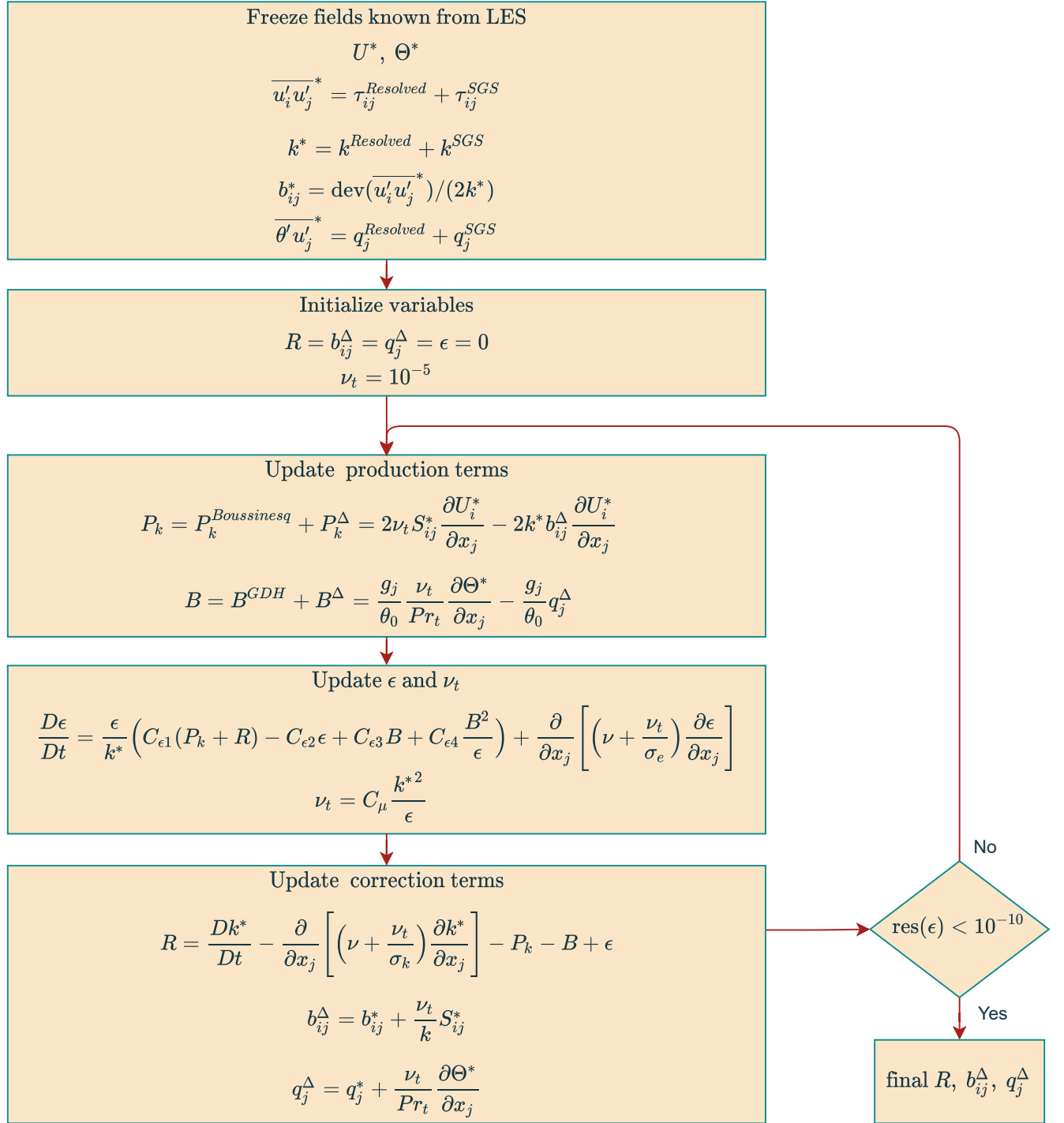


Figure 4.3: Flowchart for the Frozen-RANS method to computing model-form errors

#### 4.2.6 Consistency with LES System

In order to ensure the frozen-RANS cases are consistent with LES in terms of wall stress and driving force,  $u_*$  needs to be matched. This is done by changing the  $k - \epsilon$  model coefficients  $C_\mu$  and  $C_{\epsilon 1}$  according to eq. (4.19) and eq. (4.20). These relations relate the coefficients to the wall stress under wall equilibrium turbulence [89].

$$C_\mu = \frac{u_*^4}{k|_w^2} \quad (4.19)$$

Table 4.9: Boundary conditions for the Frozen-RANS cases

	Lower	Upper	West	South	East	North
$\nu_t$	nutkStratAtmRoughWallFunction	slip	zeroGradient	cyclic	zeroGradient	cyclic
$k$	kqRWallFunction	slip	zeroGradient	cyclic	zeroGradient	cyclic
$\epsilon$	epsilonWallFunction	slip	zeroGradient	cyclic	zeroGradient	cyclic
$R$	calculated	calculated	calculated	cyclic	calculated	cyclic
$b_{ij}^\Delta$	calculated	calculated	calculated	cyclic	calculated	cyclic
$q_j^\Delta$	calculated	calculated	calculated	cyclic	calculated	cyclic

$$C_{\epsilon 1} = C_{\epsilon 2} - \frac{\kappa^2}{\sqrt{C_\mu} \sigma_\epsilon} \quad (4.20)$$

Here, the total wall turbulent kinetic energy is obtained from the reference LES case as  $k|_w = k^{Resolved}|_w + k^{SGS}|_w$ . The friction velocity  $u_*$  is obtained as the mean from the final hour of simulation time of the precursor case. The values of  $k|_w$  and  $u_*$  are shown in table 4.10, and the corresponding model coefficients are shown in table 4.11.

Table 4.10: LES friction velocity and wall turbulent kinetic energy

	$u_*$	$k _{wall}$
Neutral	0.40	0.54
Stable	0.25	0.06
Unstable	0.57	4.39

 Table 4.11:  $k - \epsilon$  model coefficients that ensure consistency with the LES reference for the NBL case, SBL and CBL case

	$C_\mu$	$C_{\epsilon,1}$	$C_{\epsilon,2}$	$C_{\epsilon,3}$	$C_{\epsilon,4}$	$\sigma_k$	$\sigma_\epsilon$
standard $k - \epsilon$ ABL	0.03	1.21	1.92	0	0	1.00	1.30
NBL case	0.085	1.50	1.92	0	0	1.00	1.30
SBL case	1.17	1.81	1.92	0.5	1	1.00	1.30
CBL case	0.0056	0.28	1.92	0.28	0	1.00	1.30

## 4.3 Corrected RANS

With the turbulence model corrections  $R$  and  $b_{ij}^\Delta$ , and the turbulent heat flux model correction  $q_j^\Delta$  known from frozen-RANS, they can be injected back into the models during the RANS simulation. The hypothesis being that the injection results in significant improvements in the Reynolds stress profiles, the turbulent kinetic energy profiles and in the turbulent heat flux profiles. These improvements should in turn result in near-perfect matches for the velocity and potential temperature. If this is the case, the frozen-RANS framework can be applied to a set of similar LES reference flows for wind turbines in non-neutral atmospheres. The resulting corrections can then be used as input data for machine techniques to construct generalized corrected turbulence models that can be applied in a predictive setting.

### 4.3.1 Governing and Model Equations

The governing RANS equations solved in SOWFA-6 are shown in eq. (4.21), eq. (4.22) and eq. (4.23).

$$\frac{\partial U_i}{\partial x_i} = 0 \quad (4.21)$$

$$\frac{\partial U_i U_j}{\partial x_j} = -\frac{1}{\rho_0} \frac{\partial P}{\partial x_i} + \frac{\partial}{\partial x_j} \left( \nu \frac{\partial U_i}{\partial x_j} - \overline{u'_i u'_j} \right) + \left( \frac{\Theta - \theta_0}{\theta_0} \right) g_i - 2\epsilon_{i3k} \Omega_3 U_k + S_i + \frac{1}{\rho_0} \overline{f_i^T} \quad (4.22)$$

$$\frac{\partial \Theta U_j}{\partial x_j} = \frac{\partial}{\partial x_j} \left( \frac{\nu}{Pr} \frac{\partial \Theta}{\partial x_j} - \overline{\theta' u'_j} \right) \quad (4.23)$$

The momentum source  $S_i$  is taken as the mean value of the LES precursor case. The turbine forcing term  $\overline{f_i^T}$  is calculated once again by the actuator disc model. Now, however, the pitch and rotor speed are not regulated by the

Table 4.12: Mean LES rotor revolutions per minute (RPM) and pitch angle, used as input settings for the RANS cases

	mean RPM	mean rotor pitch [°]
NBL	9.09	0.0
SBL	9.301463494059407	0.0
CBL	8.43	0.0

controllers as in LES but instead kept fixed at the mean LES values shown in table 4.12.

The turbulence model turbulent heat flux model equations are the same as the frozen-RANS model equations described in section 4.2.2. The known model-form errors or corrections, calculated by the frozen method, are injected into the model equations. A blending term  $F$  is introduced that switches off the corrections 30  $m$  below the upper boundary to avoid interaction with the boundary conditions. The blending term can also be used to switch of certain corrections at the lower wall. Additionally, a relaxation term  $\gamma$  is introduced that ramps from 0 to 1 in the span of 50 or 100 iterations, depending on whether the domain is empty, for simulating free-stream flow, or contains the turbine.

$$\begin{aligned}
 \widetilde{R} &= \gamma_R F_R R \\
 \widetilde{b_{ij}^\Delta} &= \gamma_b F_b b_{ij}^\Delta \\
 \widetilde{q_j^\Delta} &= \gamma_b F_b q_j^\Delta
 \end{aligned} \tag{4.24}$$

### 4.3.2 Momentum Forcing

### 4.3.3 Initial and Boundary Conditions

For the initial conditions, the LES field for  $U_i$ ,  $P$  and  $\Theta$  are used. The initial fields for  $k$ ,  $\epsilon$  and  $\nu_t$  are taken as the final fields from the respective frozen case. For the inflow conditions, the frozen cases act as precursors to the RANS stages. During the frozen stage, boundary plane data is collected at the inflow boundary for  $U$ ,  $\Theta$ ,  $k$ ,  $\epsilon$  and  $\nu_t$ . The boundary plane data of the final frozen iterations (the iteration upon which  $\epsilon$  has converged) is then used as inflow data for the RANS case. This is represented by the `mappedFixedValue` boundary condition in `OpenFOAM-6`. All other boundary conditions for the RANS simulations are shown in table 4.13.

Table 4.13: Boundary conditions for the RANS cases under neutral (N), stable (S) and unstable (U) conditions

	Lower	Upper	West	South	East	North
$U_i$	noSlip	slip	mappedFixedValue	cyclic	inletOutlet	cyclic
$P_{rgh}$	fixedFluxPressure	fixedFluxPressure	fixedFluxPressure	cyclic	zeroGradient	cyclic
$\bar{\theta}$	zeroGradient	zeroGradient	mappedFixedValue	cyclic	zeroGradient	cyclic
$q_w$	fixedValue 0	fixedValue 0	fixedValue 0	cyclic	fixedValue 0	cyclic
$\nu_t$	nutkStratAtmRoughWallFunction	slip	mappedFixedValue	cyclic	zeroGradient	cyclic
$k$	kqWallFunction	slip	mappedFixedValue	cyclic	zeroGradient	cyclic
$\epsilon$	epsilonWallFunction	slip	mappedFixedValue	cyclic	zeroGradient	cyclic

# Large-Eddy Simulation Results

In this chapter, the LES results are presented. First, the validation of the setup is discussed in section 5.1 for the stable case, in section 5.2 for the convective case and in section 5.3 for the neutral case. Afterwards, in section 5.4, the most important results from the main precursor and successor cases are shown. All other LES successor results are shown in chapter A. Unless stated otherwise, all validation and precursor results are both temporally and spatially (in-plane) averaged, while the successor results are only temporally averaged profiles along a certain line.

## 5.1 Validation Case 1: GABLS

In this section, the validation for the SBL case is shown. Simulation results are plotted against the GABLS data [78] which is shown as a set of black lines. All of the GABLS profiles are obtained with a uniform mesh resolution of  $3.125\text{ m}$ . This is slightly finer than the mesh resolution of the SOWFA-6 cases, which have a  $5\text{ m}$  resolution below  $z = 250\text{ m}$  and a  $10\text{ m}$  resolution above.

In the LES development, particular attention is paid to the choice of velocity boundary condition on the lower wall, next to validating the general setup and mesh resolution. As described in section 4.1.6, the boundary condition `velocityABLWallFunction` is used in SOWFA-6 to limit the wall-normal velocity gradient that is supplied to the SGS model. The no-slip boundary condition is normally used in other LES solvers. In the validation plots, both boundary conditions are tested and compared with the GABLS data.

Figure 5.1 shows the time-averaged profiles of velocity and temperature for the present LES and the GABLS LES cases. The SOWFA-6 results agree with the GABLS data, which displays moderate spread. The boundary layer height, measured as the lowest location at which the wind speed can be considered geostrophic, varies from  $200\text{ m}$  to  $240\text{ m}$  between the cases. In terms of potential temperature, the profiles show a positive wall-normal gradient throughout the domain, indicating purely stable conditions. The difference between the two boundary conditions is negligible for both velocity and temperature.

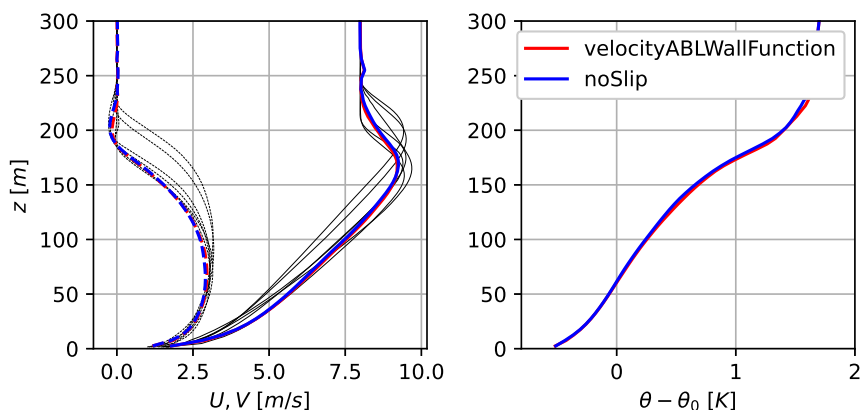


Figure 5.1: Stable boundary layer case validation results. Left:  $U$  (solid) and  $V$  (dashed) components of velocity. Right: temperature distribution. Thin black lines represent the GABLS data.

The components of the resolved Reynolds stress tensor are shown plotted against the GABLS data in fig. 5.2. At the wall, a large spread is observed in the GABLS data. The SOWFA-6 LES results show good agreements in general,

but a small peak is observed in the  $\overline{v'v'}$  and  $\overline{w'w'}$  components right below the top of the boundary layer at  $z = 180$  m. The pattern seems to be present in some of the GABLS cases as well, although less pronounced. The small local peaks are not thought to be mesh dependant, since they do not occur at the coarsening height of  $z = 250$  m.

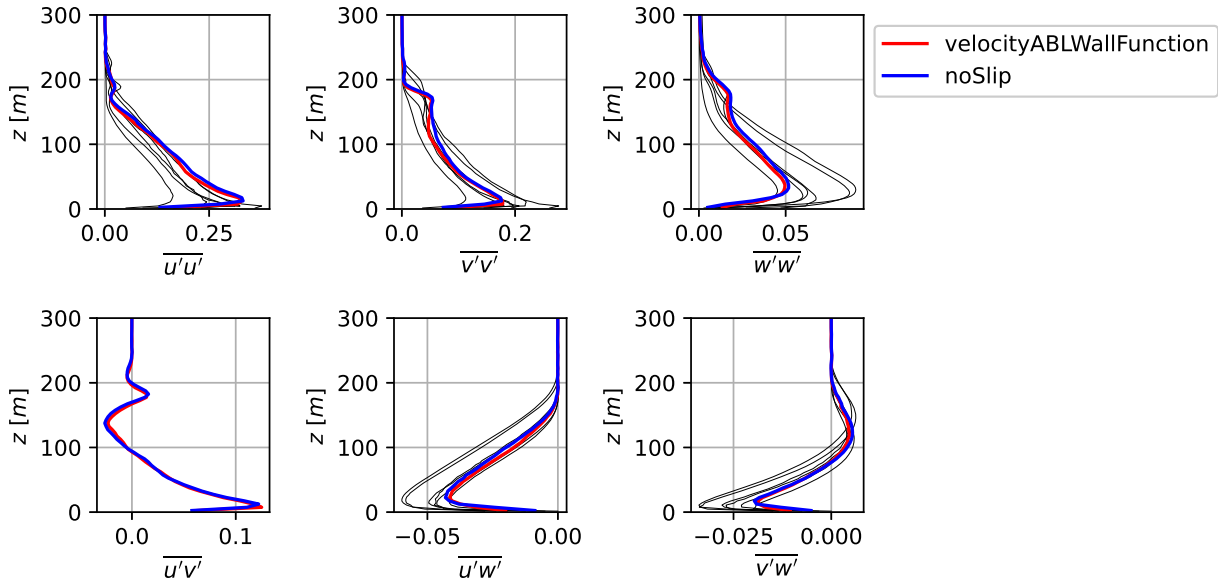


Figure 5.2: Stable boundary layer case validation results for the Resolved Reynolds stress components. Thin black lines represent the GABLS data.

The resolved heat flux components are shown in fig. 5.3. Simulation results agree reasonably with the GABLS data. For the  $x$  component, the predicted magnitudes are slightly higher than the GABLS values, while the match is better around the top of the boundary layer. For the  $y$  component, the predicted values are right on the edge of the GABLS range throughout the height of the boundary layer. For the  $z$  component, the predicted magnitudes are slightly lower than the reference close to the wall but agree well above. Once again, the choice of velocity boundary condition does not play a significant effect.

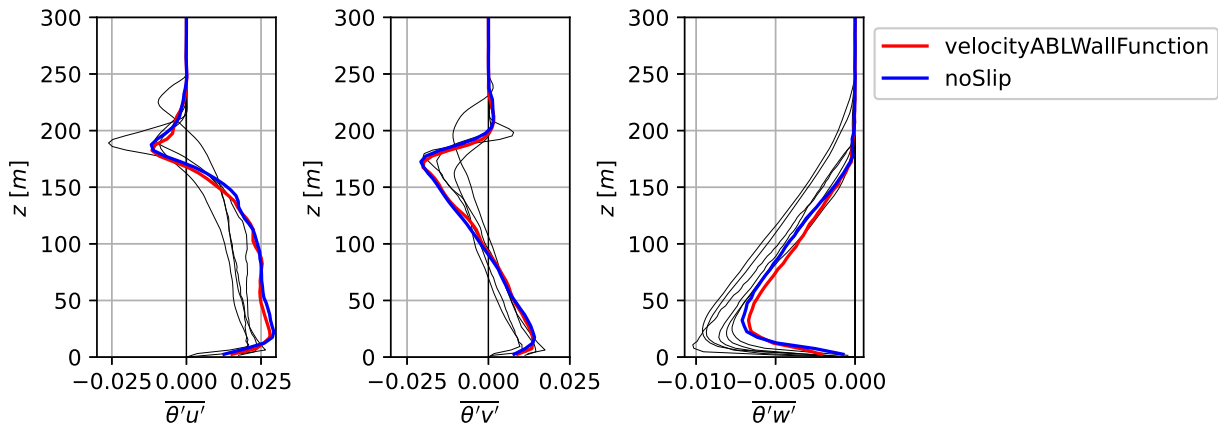


Figure 5.3: Stable boundary layer case validation results for the Resolved heat flux components. Thin black lines represent the GABLS data.

In fig. 5.4 the vertical momentum flux, or  $xz$  component of the Reynolds stress, is shown decomposed into the resolved component, the SGS component and the total. In the total momentum flux plots for the SOWFA-6 LES cases, the  $xz$  component of the average wall shear stress  $\overline{\tau_{w,xz}}$  is added at the wall. In the actual simulation code, the wall stress is introduced as a source term to the momentum equation. A large difference is observed in the SGS component of the momentum flux at the wall. For the no-slip condition, the value is significantly larger than for the velocityABLWallFunction condition or than for any of the GABLS cases. This results in a spike in the total momentum flux for the no-slip condition. Although both velocity boundary conditions show discontinuous behaviour close to the wall, it can be concluded that velocityABLWallFunction produces results that closer agree with the

validation data. Since the choice of velocity boundary condition does not have a large effect on the prediction quality of the velocity, temperature, resolved Reynolds stress and resolved heat flux profiles, the velocity boundary condition `velocityABLWallFunction` is the preferred choice in the present setup. The condition is used for all SBL and NBL cases, but can not be used for the CBL cases, as is explained in section 5.2.

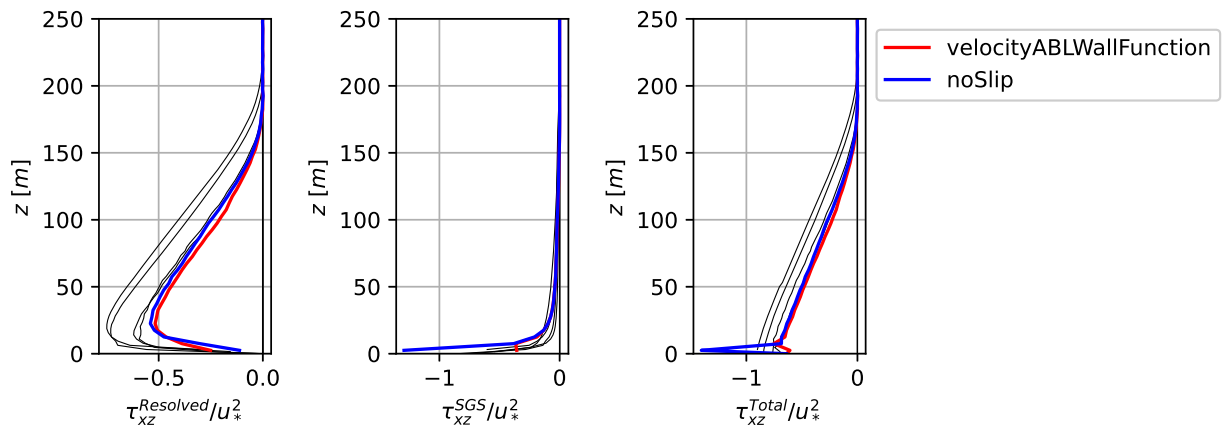


Figure 5.4: Stable boundary layer case validation results for the Vertical momentum flux decomposed into the Resolved and SGS components. Thin black lines represent the GABLS data.

## 5.2 Validation Case 2: Abkar & Moin Convective Planetary Boundary Layer

In this section, the validation for the CBL case is shown. The convective case of Abkar and Moin [79] is used as reference data. Throughout the section, their data is labelled as 'Abkar & Moin'. Figure 5.5 shows the simulation results for the mean planar average velocity and potential temperature profiles. The velocity profiles obtained using the `velocityABLWallFunction` show a large discrepancy with the validation data below the boundary layer height  $z_i$ , which is defined as the wall-normal location where the wall-normal turbulent heat flux is lowest. Additionally, an oscillating pattern is seen right in the lower part of the boundary layer, with the strongest oscillation right at the wall. The results for the no-slip condition show much greater agreement with the validation data. Moderate discrepancies exist in the stream-wise velocity in the upper part of the boundary layer and around the capping inversion. As the wind turbine in the successor stage only stretches until  $z = 150.6 \text{ m}$  or  $z/z_i = 0.146$ , the velocity mismatch at the boundary layer top likely does not affect the quality of the successor solution. Considering Abkar & Moin used a pseudo-spectral code for their LES, and `OpenFOAM` is a finite volume code, the velocity results for the no-slip case are satisfactory. Both the potential temperature profiles obtained with no-slip condition and the `velocityABLWallFunction` condition agree well with the reference, with the no-slip condition providing a slightly better match at the wall.

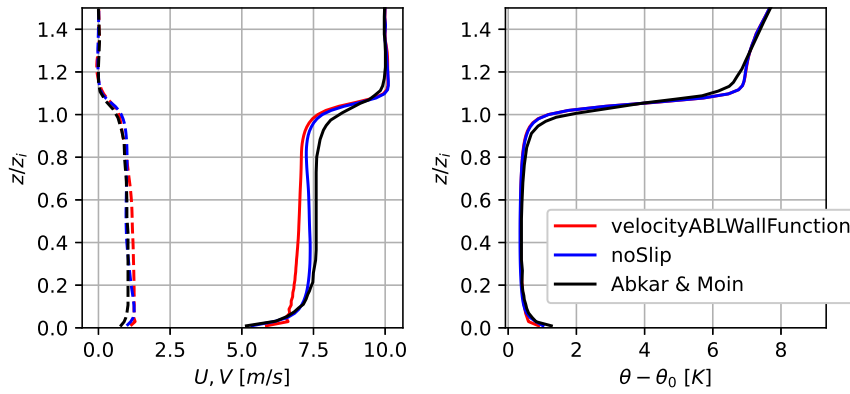


Figure 5.5: Convective boundary layer case validation result. Left: Planar averages of mean  $U$  (solid) and  $V$  (dashed) components of velocity. Right: Planar average of mean potential temperature distribution.

Figure 5.6 shows planar average profiles of the horizontal and vertical resolved stress. The values are normalised by the convective velocity  $w_* = \sqrt[3]{(|g|/\theta_0)q_w z_i}$ . Additionally, fig. 5.6 shows field observations obtained by aircraft in the Air Mass Transformation Experiment [91]. The results from both velocity boundary conditions lie on the low end of the range of the field observations. For the vertical resolved stress, the no-slip condition produces an excellent match with both observations and the validation LES results.

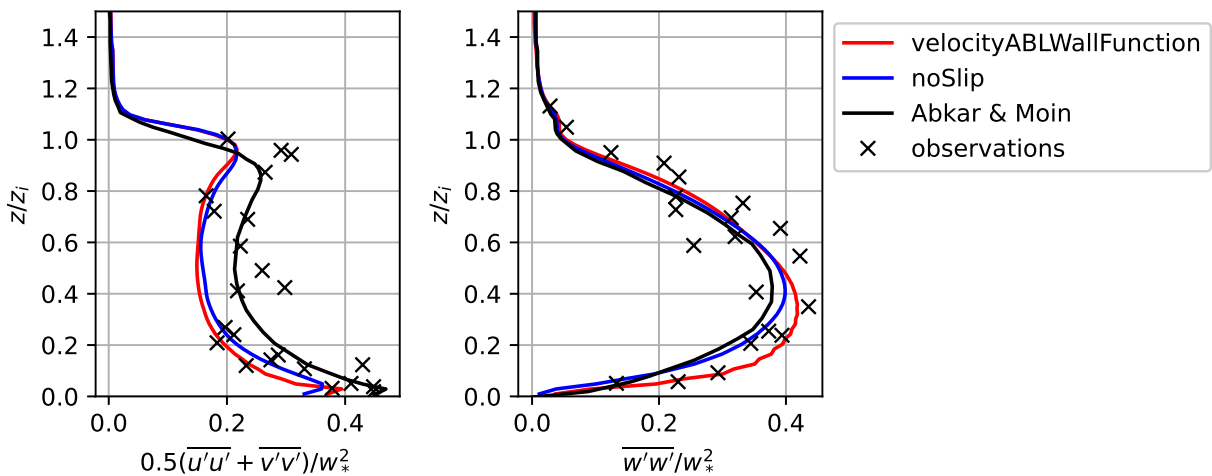


Figure 5.6: Convective boundary layer case validation results for the planar averages of the horizontal (left) and vertical (right) resolved stresses, compared to field aircraft observations.

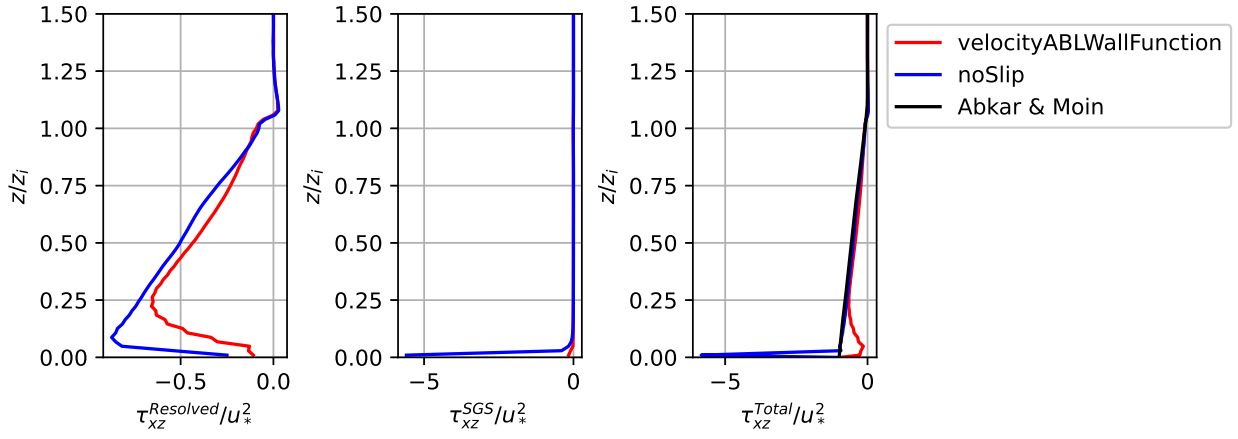


Figure 5.7: Convective boundary layer case validation results for the planar averages of the vertical momentum flux decomposed into the Resolved and SGS components.

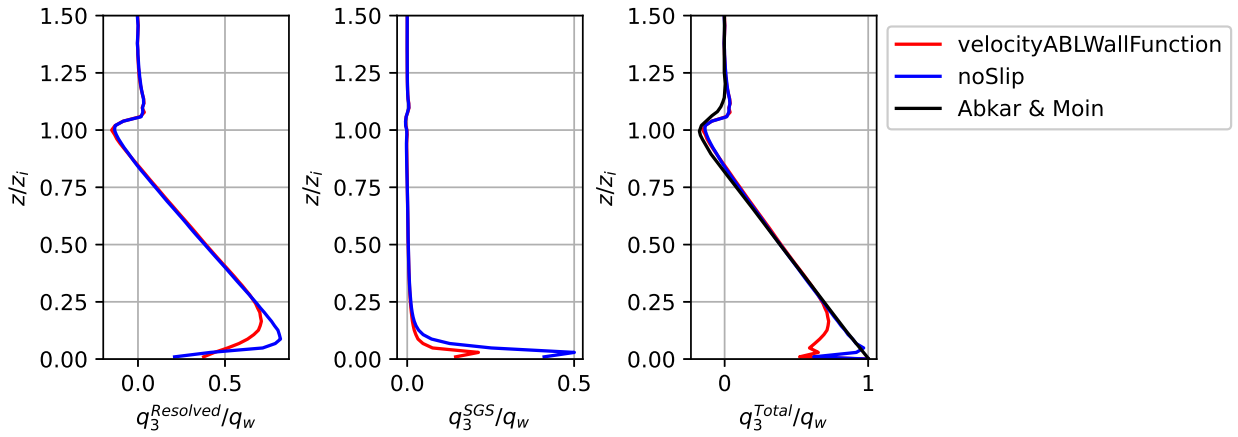


Figure 5.8: Convective boundary layer case validation results for planar averages of the vertical heat flux decomposed into the Resolved and SGS components.

The momentum flux is compared with the validation case in fig. 5.7. In accordance with the results obtained for the stable boundary layer, using the no-slip condition for velocity at the wall results in a high value of SGS momentum flux at the wall, which carries over to the total momentum flux. upwards of this peak in momentum flux, the no-slip actually produces a much closer match with the validation case than `velocityABLWallFunction` does. Figure 5.8 shows the vertical component of the turbulent heat flux. At the wall, the value of  $q_w = 0.24$  is added to the total vertical heat flux. During simulation runtime, this value is not added to the resolved or SGS component of the heat flux, but rather added as a source term to the temperature equation, as seen in eq. (4.3). The results from both velocity boundary conditions agree well in the middle and upper part of the boundary layer. However, as was the case with the momentum flux, the no-slip condition produces a better match in the lower part of the boundary layer. Only at the height of the first two cells does the total heat flux disagree with the reference.

### 5.3 Validation Case 3: Rough Wall Atmospheric Log-Law

As was established in the section 5.1, the use of the velocity boundary condition `velocityABLWallFunction` is preferred over the no-slip condition if possible. As another check, the NBL case, which is essentially the GABLS case modified to be neutrally stratified, is compared against the atmospheric boundary layer log-law (eq. (2.7)) in fig. 5.9. The agreement is well throughout most of the domain. At the first cell, the velocity is lower than log-law. This is the direct working of the boundary condition `velocityABLWallFunction`. Since the match is generally well and the profile is smooth, unlike how it was for the CBL case, the boundary conditions is deemed suitable for the NBL case.

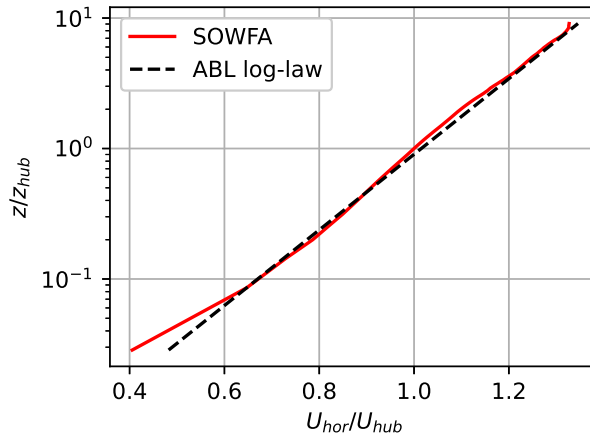


Figure 5.9: Neutral boundary layer case horizontal velocity planar averages compared to the rough wall ABL log-law

## 5.4 Main Case Results

The main precursor and successor results are shown in this section. For the successor stage, only velocity deficit profiles are shown. Kinetic energy and heat flux profiles will be shown and discussed in detail in chapter 7, where they are compared to the corrected RANS profiles. The complete set of LES successor wake profiles are also shown in Appendix chapter A. Note that the successor profiles are not spatially averaged but samples along lines in certain parts of the domain. All results are time-averaged unless otherwise stated.

In table 5.1, the general results of the LES precursor and successor cases are summarized. All quantities tabulated are time averages of the final hour of simulation time, during which the simulations are (quasi-)stationary. In all cases, the wind turbine operates in the lowly loaded region and below its rated point of 12.1 RPM [84].

Table 5.1: General time-averaged LES results

		NBL	SBL	CBL
Hub-height velocity	$U_{hub} [m/s]$	7.50	7.45	7.15
Friction velocity	$u_* [m/s]$	0.40	0.25	0.57
Wall heat-flux	$q_w [Km/s]$	0.0	-0.011	0.24
Monin-Obukhov length	$L [m]$	$\infty$	100.0	-61.4
Thrust coefficient	$C_T$	0.82	0.80	0.70
Power coefficient	$C_P$	0.57	0.56	0.44
turbine RPM		9.09	9.00	8.43
turbine pitch	$\phi [^\circ]$	0.0	0.0	0.0

### 5.4.1 Neutral Boundary Layer

In order to assess statistical stationarity, the friction velocity of the simulations is plotted over time in fig. 5.10. A level friction velocity or equivalent wall stress time series indicates a stationary. Time averaging should only be done when the flow is stationary and for a long enough period. The figure shows how the successor case starts 1.5 *hr* before the end of the precursor. In other words, boundary plane data is collected during this window. The time averages of both the precursor and successor stages are taken over the final hour of the simulation so that the averaging periods coincide. This hour constitutes roughly 14 flow-throughs. All time-averages are taken over a period during which the flow can be considered stationary.

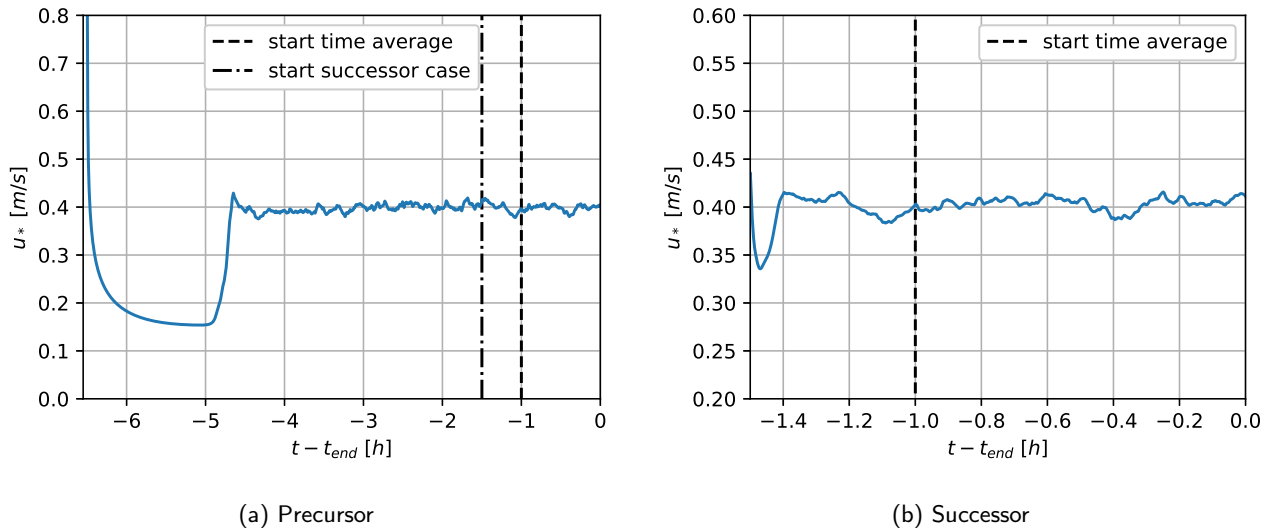


Figure 5.10: Neutral boundary layer case convergence based on friction velocity  $u_*$  time series

Velocity profiles along vertical lines upstream of the wind turbine are plotted in fig. 5.11. The effect of the turbine forcing shows as the velocity decreases closer to the turbine. The profile at 1.5 rotor diameters  $D$  upstream of the turbine is considered outside of the induction region, and is used as free-stream velocity to calculate later velocity deficit profiles.

Figure 5.12 shows vertical wake velocity and wake velocity deficit profiles on the left, and horizontal wake profiles on the right. All profiles are collected along lines at the indicated stream-wise stations with respect to the turbine.

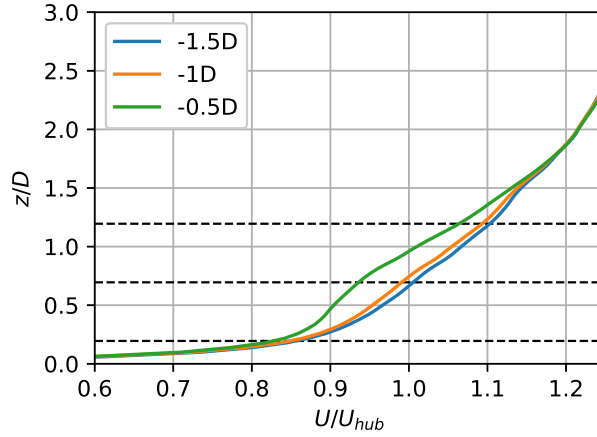


Figure 5.11: Neutral boundary layer velocity profiles in the induction region

The velocity deficit is clear, and a slow wake-recovery is observed. Furthermore, in the far wake, the horizontal velocity deficit profiles appear to be Gaussian of shape, as is reported in literature.

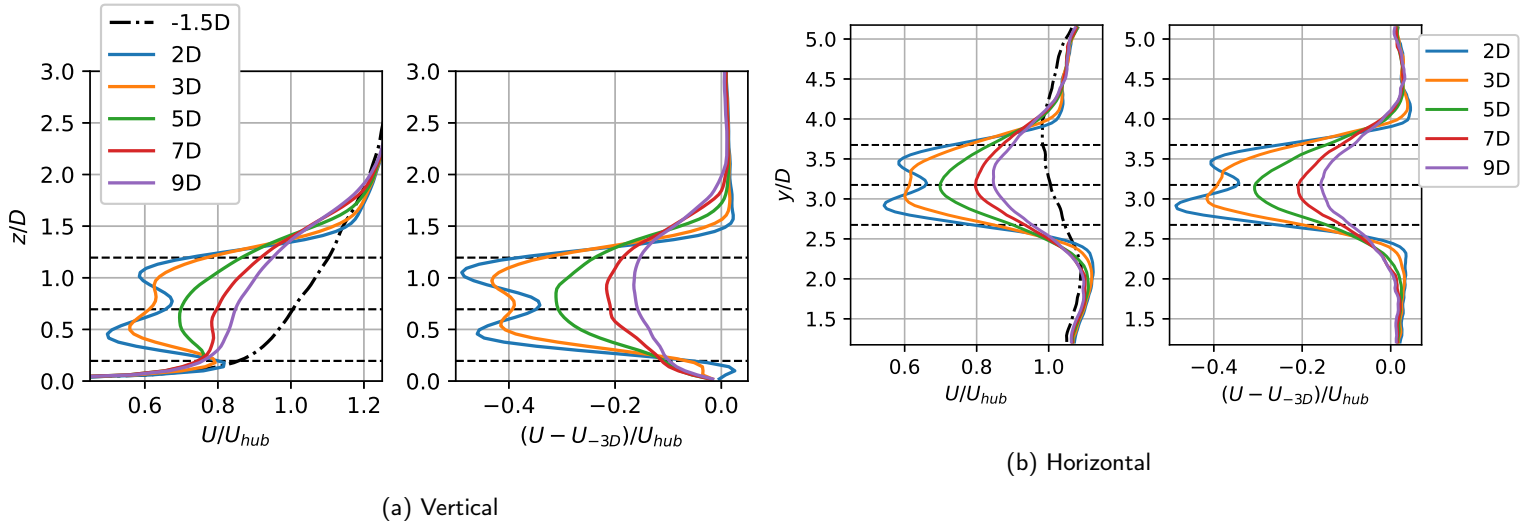


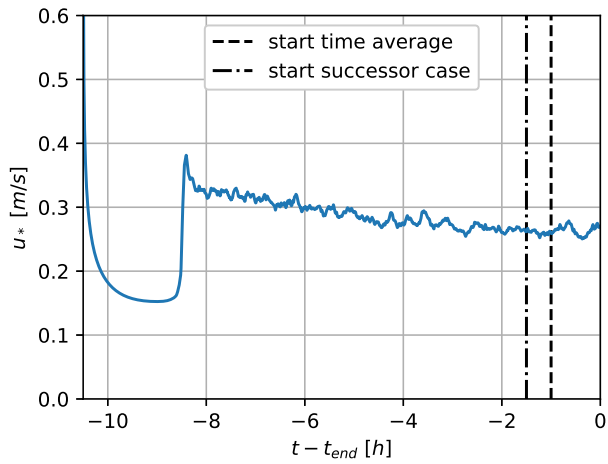
Figure 5.12: Neutral boundary layer velocity and velocity deficit profiles in the wake

### 5.4.2 Stable Boundary Layer

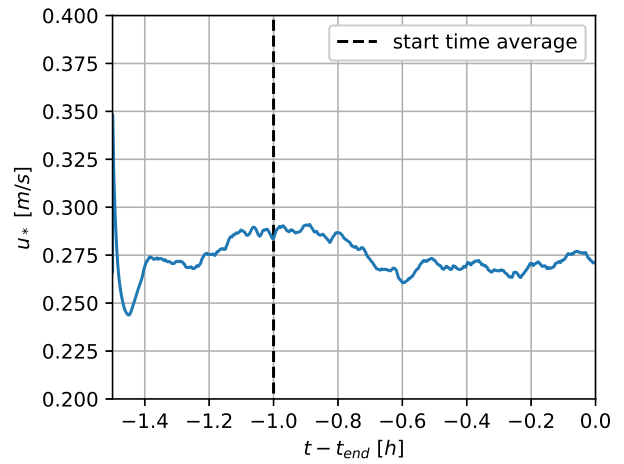
Figure 5.13 shows the friction velocity time series for the precursor and successor case. The result is slightly different than the neutral case, as the friction velocity appears to stabilize after 1.5 *hr* of simulation time but then gradually decreases. This decrease is due to the lower wall heat flux boundary condition. Instead of prescribing a fixed negative surface heat flux, it is considered best practice for stable boundary layer LES to prescribe a constant temperature change. In this case, the wall temperature change is set to  $-0.25 \text{ K/hr}$ , as was done for the GABLS validation case. This results in variable surface heat flux over time until the flow reaches quasi-stationarity, as is shown in fig. 5.14. Again, all time averages are taken over the final hour of simulation time, constituting roughly 14 flow-throughs. Furthermore, all averages are taken during quasi-stationary flow conditions. The flow is considered, quasi-stationary, as opposed to stationary since the temperature in the domain still changes over time due to the non-zero heat balance.

Velocity profiles along vertical lines upstream of the wind turbine are plotted in fig. 5.15. The effect of the turbine forcing shows as the velocity decreases closer to the turbine. A much higher velocity gradient is observed compared to the neutral case, along with a low-level jet. The profile at 1.5 rotor diameters  $D$  upstream of the turbine is considered outside of the induction region, and is used as free-stream velocity to calculate later velocity deficit profiles. Some mesh-dependant effect is seen in the velocity profiles at the mesh coarsening level of  $z/D \approx 2$ .

Figure 5.16 shows vertical wake velocity and wake velocity deficit profiles on the left, and horizontal wake profiles on the right. The velocity deficit is clear, and a slow wake-recovery is observed once more. Compared to the neutral



(a) Precursor



(b) Successor

Figure 5.13: Stable boundary layer case convergence based on friction velocity  $u_*$  time series

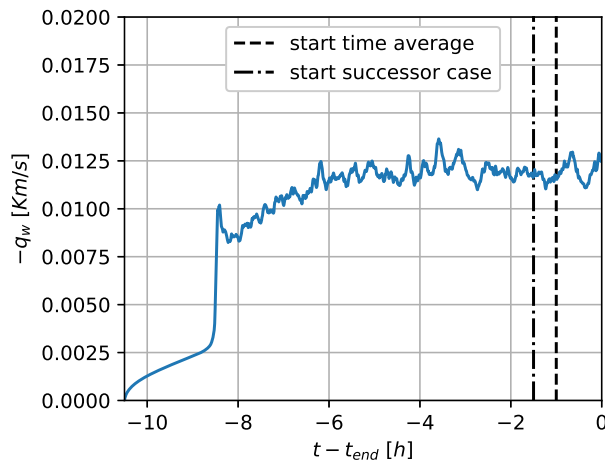


Figure 5.14: Stable boundary layer case wall heat flux  $q_w$  time series

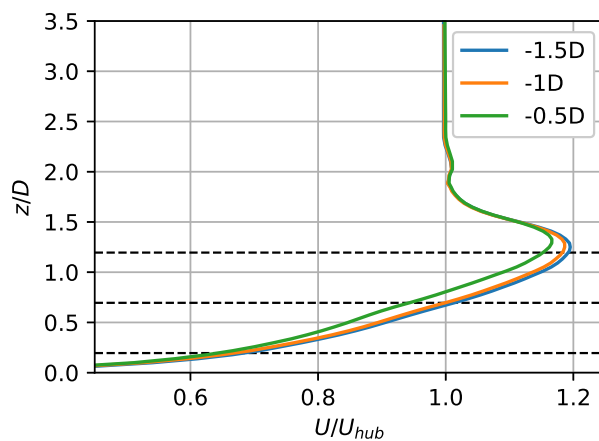


Figure 5.15: Stable boundary layer induction region velocity profiles

case, the wake appears to be significantly thinner, as less spreading is observed. Even until,  $9D$  downstream of the rotor plane, the wake is strictly limited to the lateral and wall-normal coordinates of the wind turbine rotor. Again, Gaussian-shaped velocity deficit profiles are observed in the far-wake.

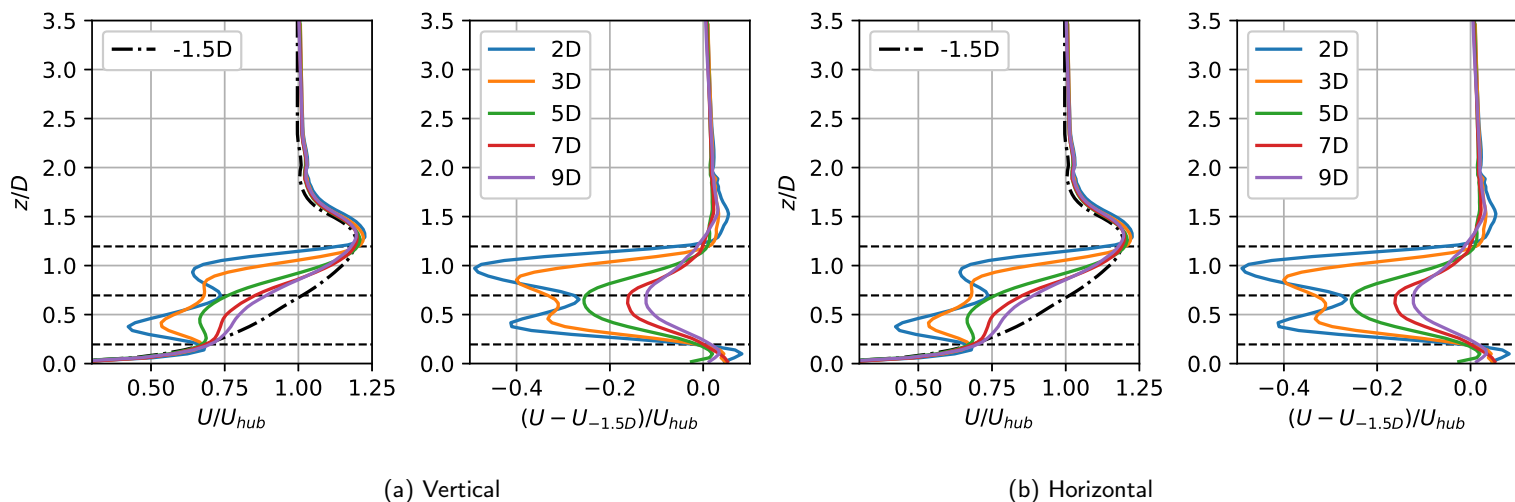


Figure 5.16: Stable boundary layer velocity and velocity deficit profiles in the wake

### 5.4.3 Convective Boundary Layer

Figure 5.17 shows the friction velocity time series for the convective boundary layer precursor and successor stages. After the initial development of turbulence, the flow becomes fully quasi-stationary, since the prescribed heat flux is constant over time. The averaging period of 1 *hr* constitutes 5 flow-throughs. The amount is significantly less than in the neutral and stable case due to the larger stream-wise domain length; 5 *km* for unstable versus 2 *km* for neutral and stable. In section 5.2 it was discussed how the use of the no-slip condition as lower wall velocity boundary

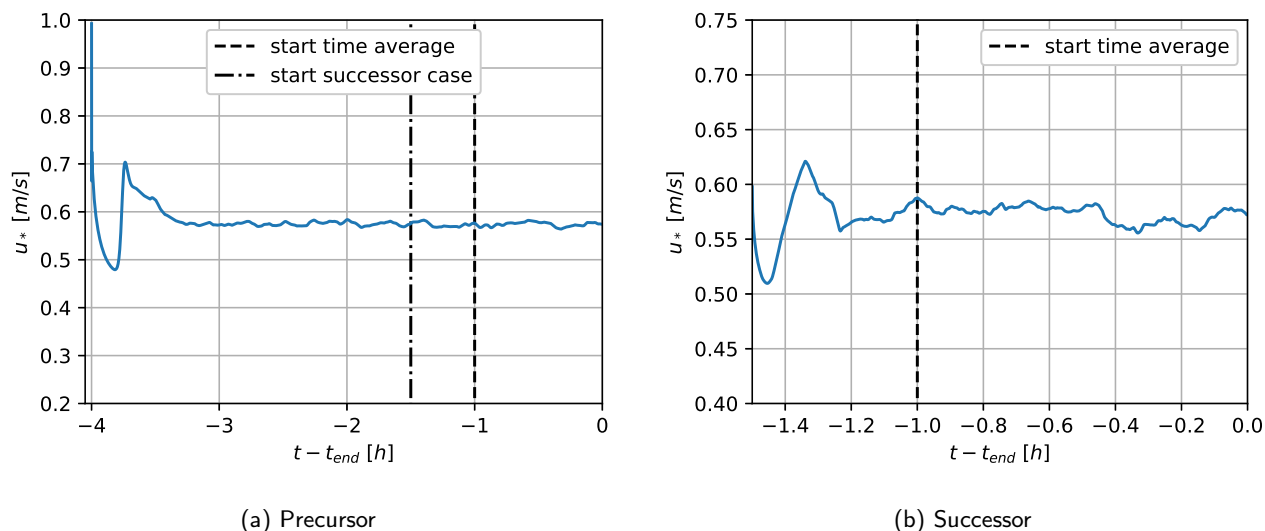


Figure 5.17: Convective boundary layer case convergence based on friction velocity  $u_*$  time series

condition resulted in a high  $xz$  component of the SGS stress tensor. Planar average profiles of the resolved and SGS stress tensor of the precursor are plotted in fig. 5.18. The same high SGS stress observed in the  $xz$  component are seen in the  $xx$ ,  $yy$  and  $zz$  components, resulting in large total stresses at the wall. Figure 5.19 shows a similar pattern for the turbulent kinetic energy.

The velocity profiles in the induction region are shown in fig. 5.20. The induction effect can be seen until about  $3D$  upstream of the turbine, as the difference between the  $5D$  and  $3D$  profiles is negligible. The  $5D$  profile is used as the free-stream in further velocity deficit plots. Even though these results are time-averaged, some non-smooth patterns are observed in the profiles, suggesting the averaging window of 1 *hr*  $\approx$  5 flow-throughs might not be sufficient.

The wake velocity and velocity deficit profiles for the unstable case are shown in fig. 5.21. Wake recovery occurs much quicker than for the neutral and stable case, with the wake being nearly fully recovered at 9 diameters downstream. Furthermore, the lateral wake spread is much greater under convective conditions as well. These are all results that are expected when turbulence production is promoted in the free-stream atmosphere.

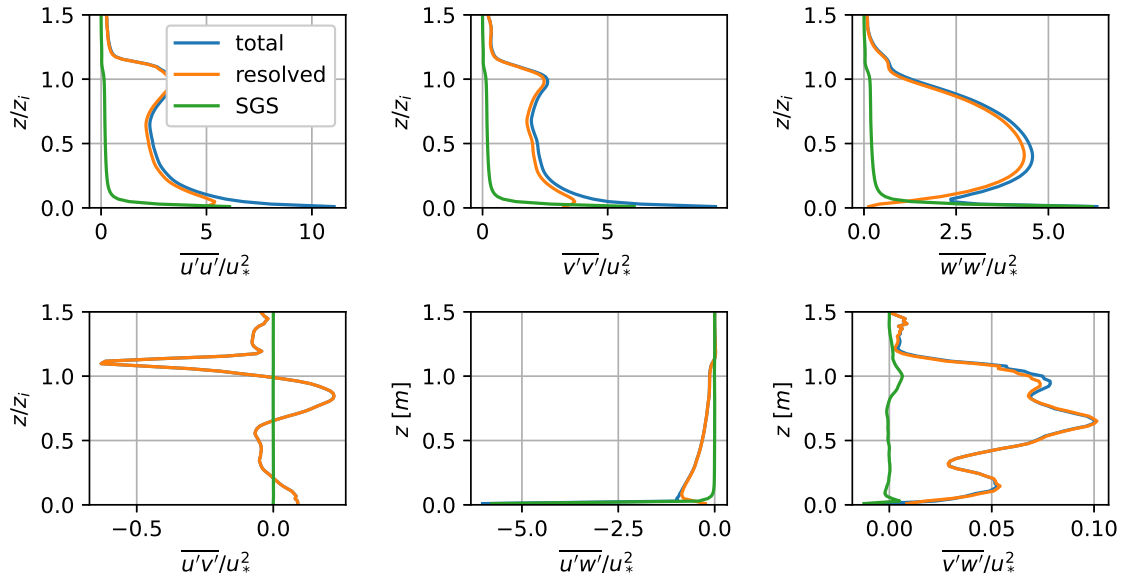


Figure 5.18: Convective boundary layer precursor Reynolds stress components

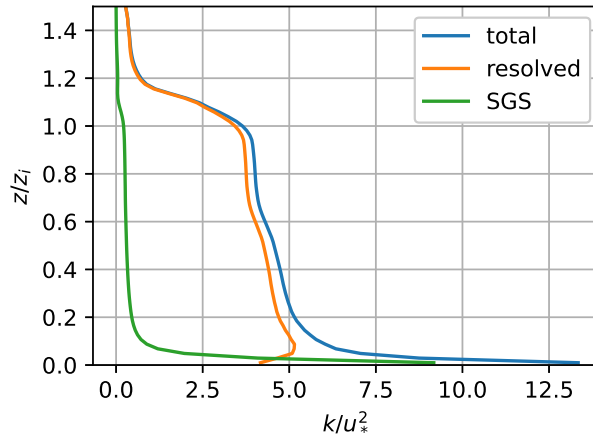


Figure 5.19: CBL case precursor turbulent kinetic energy

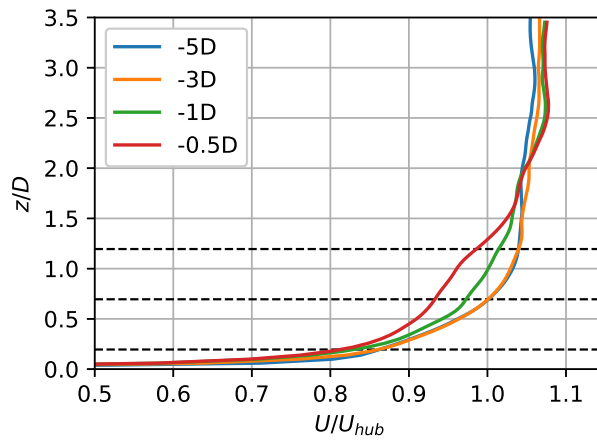


Figure 5.20: Convective boundary layer induction region velocity profiles

## 5.5 Averaging Period Sensitivity Study

For the convective boundary layer, the velocity profiles show high levels of non-smooth structure, particularly in the far-wake. Similar patterns are observed for the turbulent kinetic energy and turbulent heat fluxes in Appendix

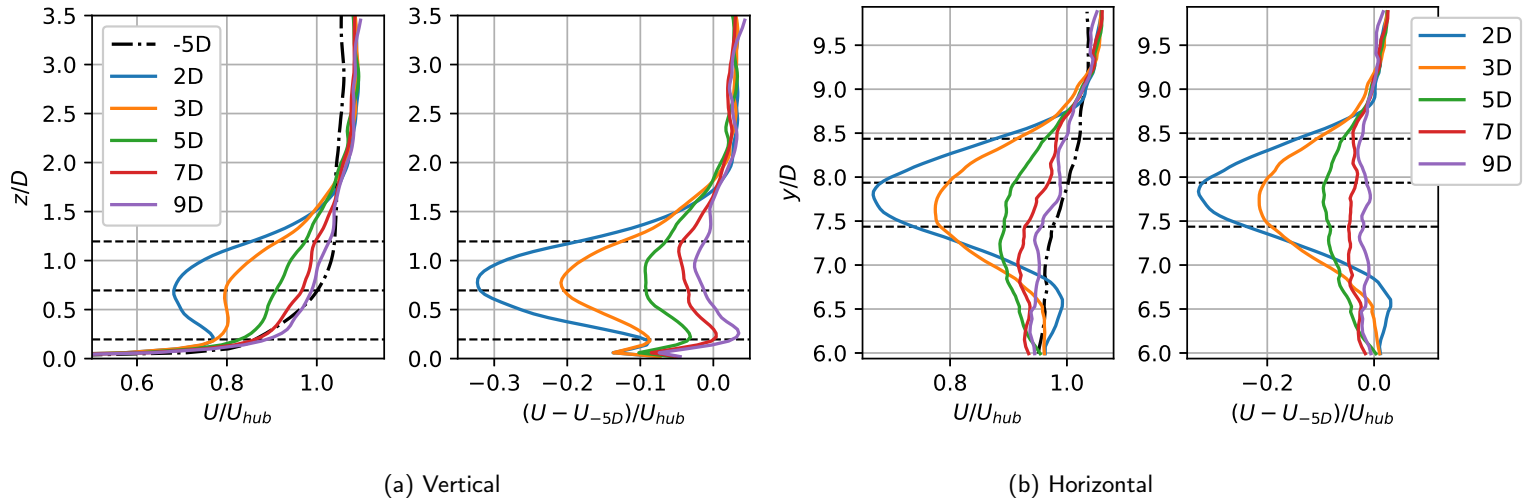


Figure 5.21: Convective boundary layer velocity and velocity deficit profiles in the wake

chapter A. This is an undesirable result, as time-averaged profiles are typically smooth. The non-smooth profiles in the far-wake are attributed to large-scale turbulent structures with long time scales. The near-wake results appear smooth since the turbulent structures here are of much smaller spatial and temporal scales. Similarly, the neutral and stable boundary layer time-averaged profiles are smoother because the more stable boundary layer (relative to the convective boundary layer) limits the observed turbulent sales. The stable boundary layer turbulent heat flux profiles are an exception, as these results also contain some non-smooth structure. The stable boundary layer, however, is not included in the averaging period analysis due to limitations in time.

The non-smooth far-wake profiles in the convective boundary layer successor suggest that larger averaging periods are required. The effect of the averaging window is therefore investigated and presented in this section. Five results are shown; representing time averaging windows that range from 1 hour in duration to five duration. All results are obtained with the time averaging window starting at the same simulation time. Additionally, all convective boundary layer LES successor results with a 5-hour averaging period are shown in Appendix chapter A.

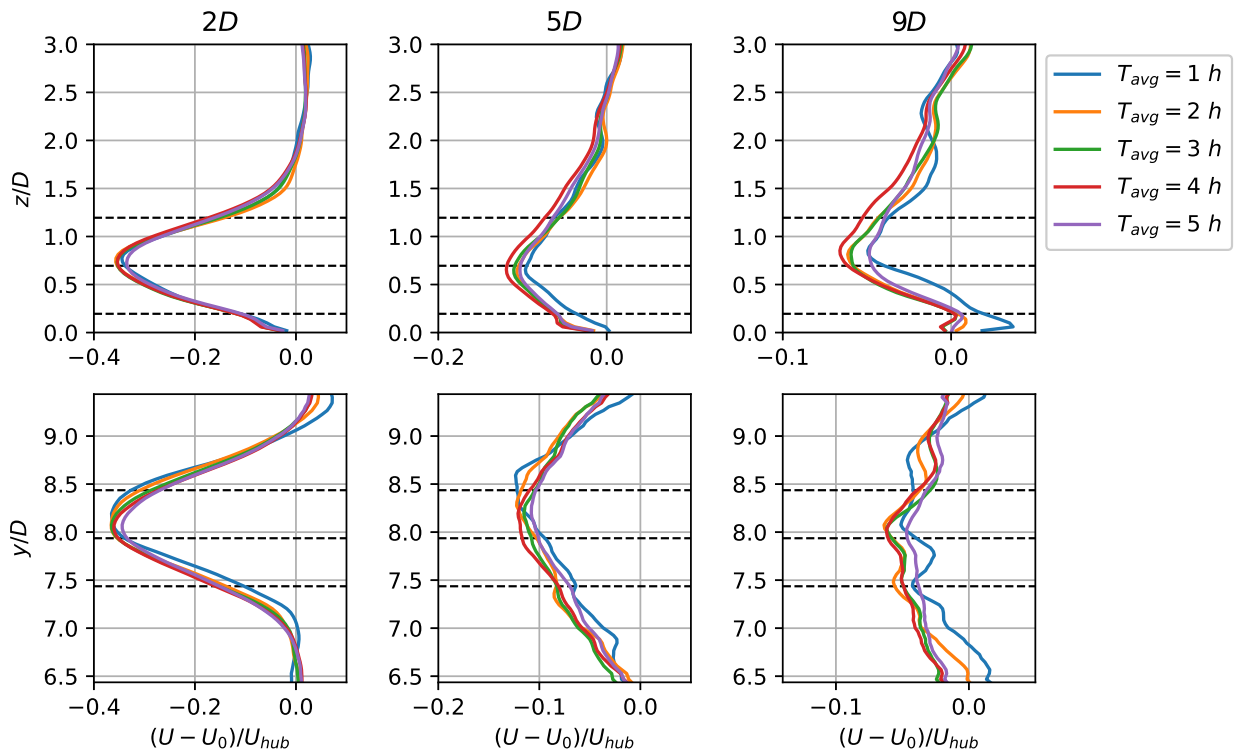


Figure 5.22: Sensitivity of wake velocity deficit profiles to the time averaging period for the CBL case

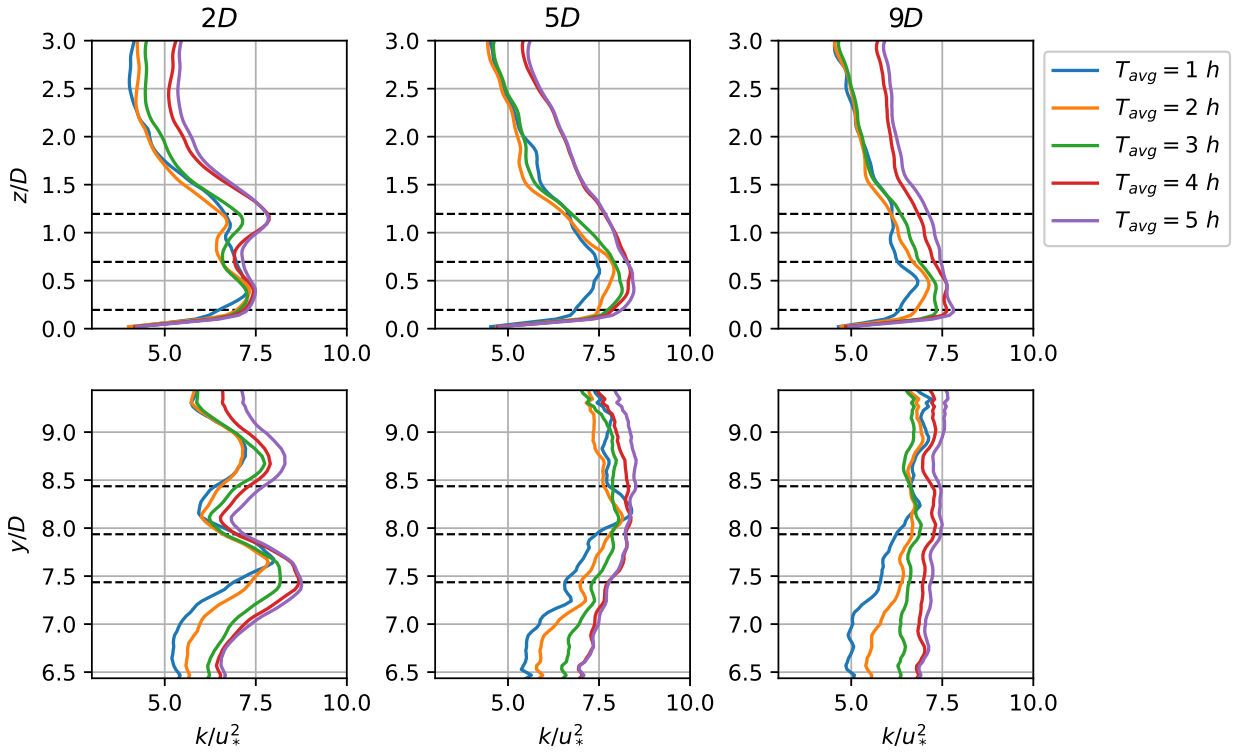


Figure 5.23: Sensitivity of wake turbulent kinetic energy profiles to the time averaging period for the CBL case

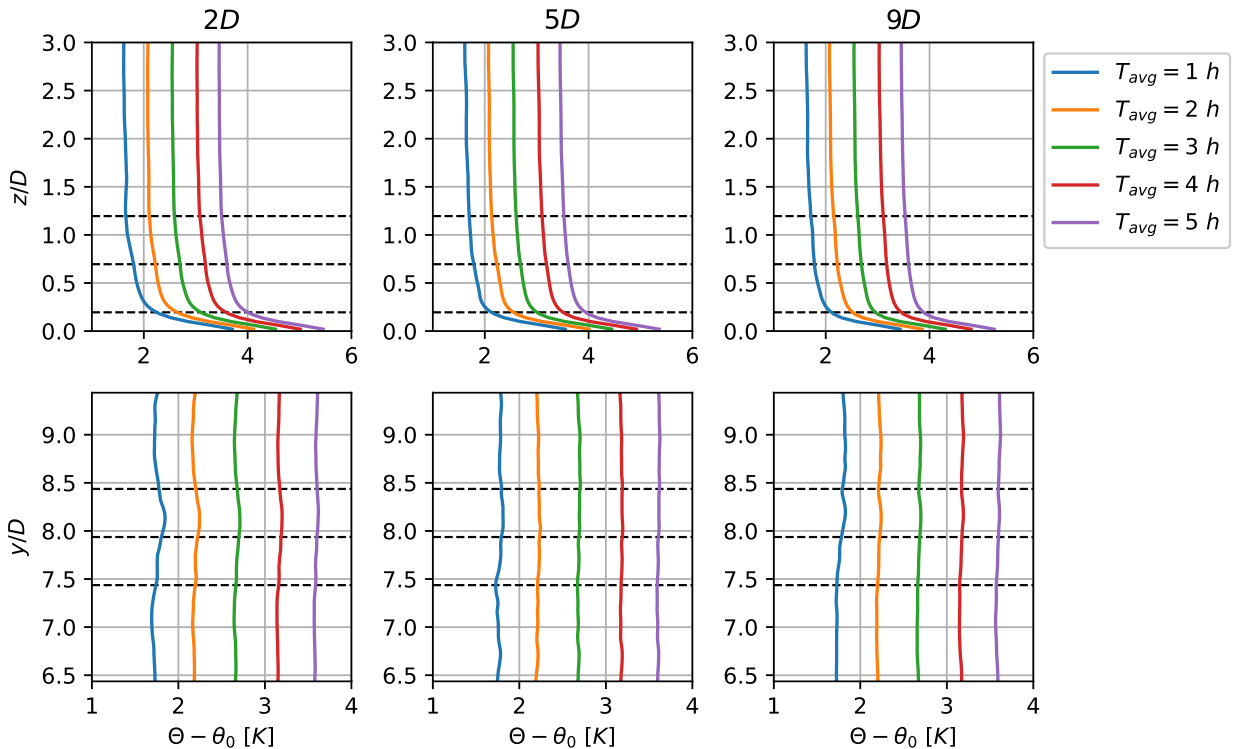


Figure 5.24: Sensitivity of wake potential temperature profiles to the time averaging period for the CBL case

Wake velocity deficit profiles are shown in fig. 5.22. At  $2D$  downstream of the turbine rotor, only minor differences are observed in the location of the wind turbine wake. At  $5D$  and  $9D$  downstream of the rotor, non-smooth profiles are successfully smoothed by longer averaging periods. The strong wall speed-up effect observed for  $T_{avg} = 1 h$  is no longer present for the longer averaging duration. It can not be said, however, that the profiles converge to the same

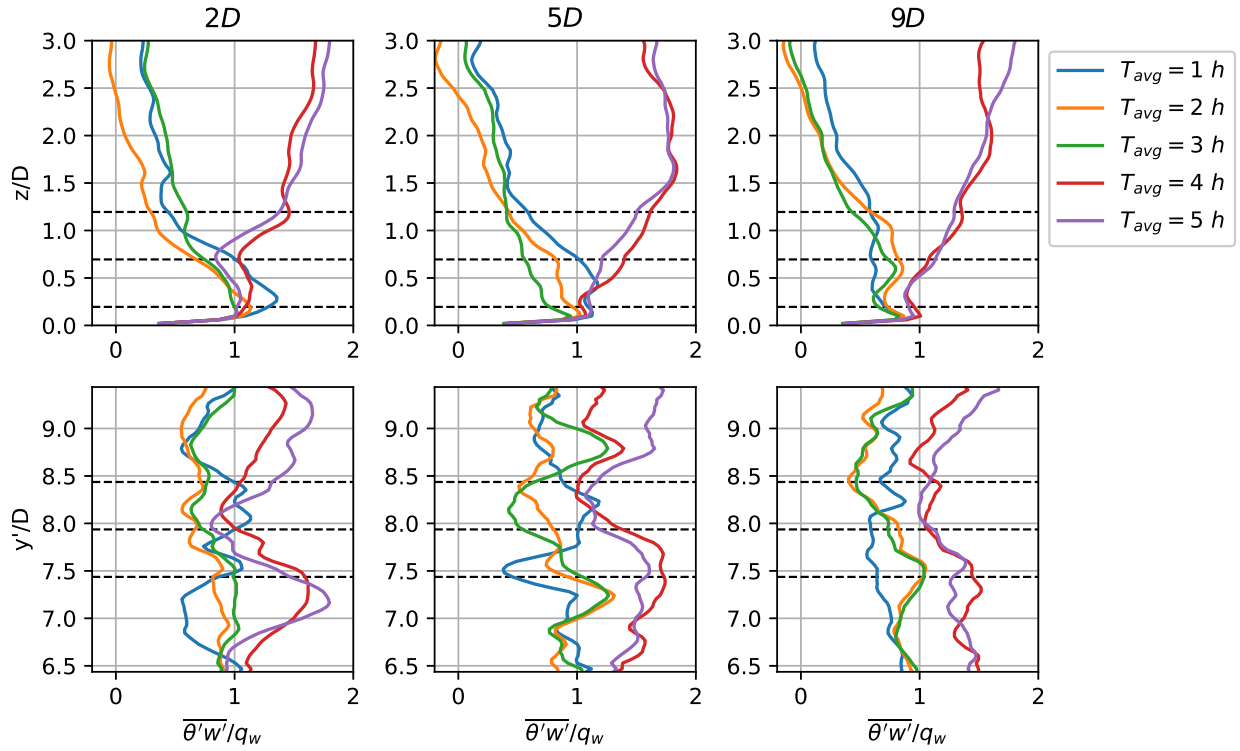


Figure 5.25: Sensitivity of wake wall-normal turbulent heat-flux profiles to the time averaging period for the CBL case

values as some drift is seen at all stations.

For the turbulent kinetic energy, shown in fig. 5.23, increasing the time averaging duration also smooths the profiles significantly. The drift between the different profiles is, however, even stronger than with the velocity. Particularly, there is a large drift between  $T_{avg} = 3 h$  and  $T_{avg} = 4 h$  in the wall-normal profiles. For span-wise wake profiles, the drift is strongest in between the shorter averaging windows.

The small drift observed in the velocity deficit and TKE profiles is a result of the accumulation of heat in the domain. This is seen clearly in the mean potential temperature profiles shown in fig. 5.24. The accumulation of heat results in the flow state changing slowly over time. In a sense, this means that besides turbulent variations around some mean, an additional time-varying bias exists in the solution, which is averaged out in the present formulation. What effect this has on the frozen-RANS and RANS simulation results is unknown.

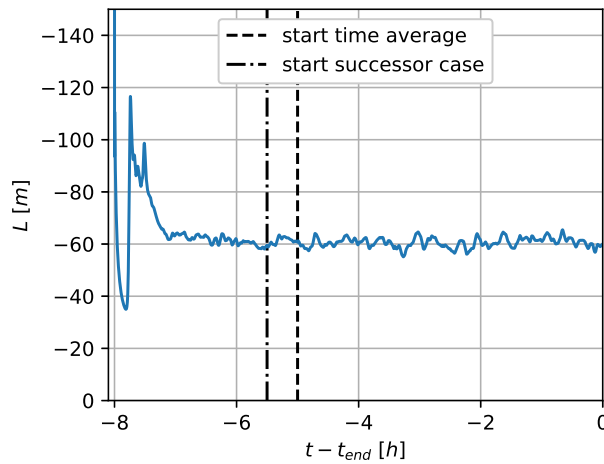


Figure 5.26: Monin-Obukhov length time series for the convective boundary layer case with  $T_{avg} = 5 h$

Finally, the heat flux profiles are shown in fig. 5.25. A drastic variation is seen between  $T_{avg} = 3 h$  and  $T_{avg} = 4 h$ . It looks to be related to the smaller variation seen in the kinetic energy profiles. It seems as though some event occurred between these times that triggered a massive increase in wall-normal turbulent fluctuations for the rest of

the simulation. It is likely that at some point in time one or more very large convective eddies formed in the domain and were recycled for by the periodic boundary conditions at the precursor inflow and outflow boundaries. Since the successor inflow data is obtained from a recording of the precursor inflow boundary, these large convective turbulent motions carried over the successor case. As seen in fig. 5.26, the event that causes the large shift in heat flux and TKE does not have an influence on the Monin-Obukhov length. Besides this result, it is noteworthy that a large degree of non-smooth structure is still present in the  $T_{avg} = 5 h$  profiles.

Although longer averaging periods indeed result in smoother time-averages, the change in averaging period does not seem to improve the frozen-RANS and corrected RANS solution quality. The effect of the LES averaging period on these techniques is shown and discussed in section 7.4.

## Frozen-RANS Results

For all three cases, the frozen-RANS method is first applied to the precursor case. This gives us insight into how well the baseline model replicates the LES free-stream flow. Afterwards, results are shown for the frozen approach applied to the successor case, giving an indication of the baseline model's ability to represent the wind turbine wake.

All model-form errors, or equivalently corrections, as well as their effect on shear and buoyant turbulent production, are plotted relative to the respective LES reference value, indicated by the superscript \*. However, since the transport equation residual  $R$  does not have a direct LES value, it is shown normalized with another metric: the mean Boussinesq shear production or gradient-diffusion hypothesis (GDH) buoyancy production in the lowest part of the boundary layer. This metric is chosen so that it is easy to compare values against production terms that might typically be observed in RANS simulations close to the wall. The definition and value for the metrics vary depending on the stability case and are summarized in table 6.1.

Table 6.1: Shear and buoyancy production based normalization metrics for the frozen correction figures.  $D = 126 m$  and  $z_i = 1070 m$ .

Case	Shear production metric [ $m^2/s$ ]	Buoyancy production metric [ $m^2/s$ ]
NBL	$\text{mean}_{z/D < 1}(P_k^{Boussinesq}) = 0.0194$	-
SBL	$\text{mean}_{z/D < 1}(P_k^{Boussinesq}) = 0.0168$	$\text{mean}_{z/D < 1}(B^{GDH}) = -1.49 \cdot 10^{-3}$
CBL	$\text{mean}_{z/z_i < 0.1}(P_k^{Boussinesq}) = 3.83 \cdot 10^{-3}$	$\text{mean}_{z/z_i < 0.1}(B^{GDH}) = 9.57 \cdot 10^{-4}$

### 6.1 Neutral Boundary Layer

Figure 6.1 shows planar averages of the normalized anisotropy error  $b_{ij}^\Delta$  compared to the Boussinesq and LES (asterisk \*) values. For the 11, 22, 33 and 12 components, the Boussinesq hypothesis completely fails to predict any anisotropy, meaning the  $b_{ij}^\Delta$  completely accounts for the LES reference value. For the 13 and 23 components, the Boussinesq hypothesis provides a reasonable prediction. As such, the corrections remain small. Figure 6.2a shows how the anisotropy error affects the shear turbulence production term. The quantity  $P_k^\Delta$  represents the direct effect of the normalized anisotropy error. It is shown to correct for an overproduction of turbulence at the wall. The transport equation residual  $R$ , shown in fig. 6.2b, has a negative value right at the wall and shows a positive peak above. Additionally, mesh definded oscillations are seen below the coarsening height. Considering the small normalization value (table 6.1), the transport equation residual values are considered small as well.

The effect of the anisotropy error on the shear production of turbulence is shown for the successor case in fig. 6.3a. The negative value around the wind turbine rotor shows that the baseline model over-produces mechanical turbulence around the rotor and in the upper part of the near-wake, as is consistent with literature. Contours for the transport equation residual  $R$  are shown in fig. 6.3b. Large positive and negative values are observed next to each other at the upper edge of the near wake. In the far wake, some noise is observed. Additionally, negative values are seen right upstream of the rotor and at the wall below the rotor. The corrections  $P_k^\Delta$  and  $R$  generally show much greater magnitudes when considering the wind turbine flow. This makes sense considering the increased complexity compared to standard ABL flows and the limitations of the Boussinesq hypothesis.

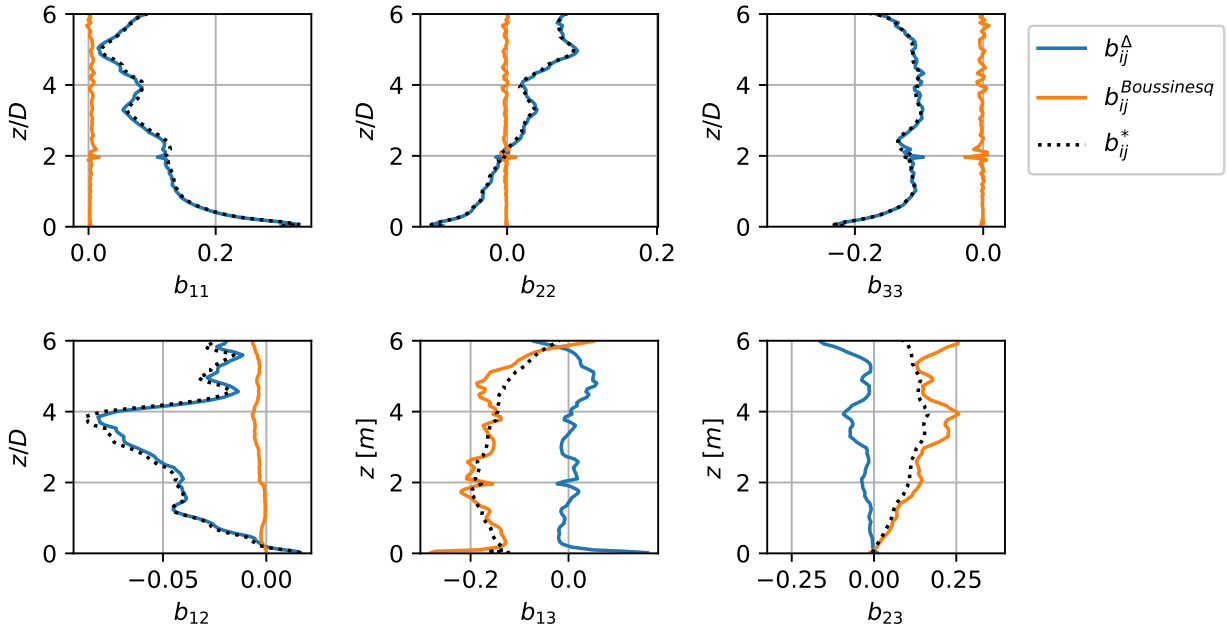


Figure 6.1: Frozen-RANS results for the NBL precursor case showing the normalized anisotropy error

## 6.2 Stable Boundary Layer

### 6.2.1 $k - \epsilon$ Model-Form Errors

The normalized anisotropy error is plotted against the Boussinesq and LES (asterisk \*) values in fig. 6.4. As was the case with the neutral case, the Boussinesq model fails to produce any meaningful values for the 11, 22, 33 and 12 components. However, the Boussinesq model now also fails to produce well-matching results for the other components, leading to large correction values for every single component.

The effect of  $b_{ij}^\Delta$  on shear production is visualized by plotting  $P_k^\Delta$  against the Boussinesq and LES values in fig. 6.5a. A similar pattern is observed with the neutral case;  $P_k^\Delta$  corrects for an overproduction of mechanical turbulence close to the wall. Additionally,  $P_k^\Delta$  corrects for a small production of turbulence right above the peak at the wall until  $z/D \approx 1.7$ . In fig. 6.5b, a very large wall value is observed for the transport equation residual  $R$ .

Contours for  $P_k^\Delta$  and  $R$  are shown in fig. 6.6. The shear production correction shows the baseline model overproduces turbulence at the rotor and around the upper edge of the near wake, as was the case under neutral conditions. The transport equation residual  $R$  shows a similar pattern at the rotor and at the wall below the rotor with small negative values. In the wake, the patterns has changed considerably. Large positive values are observed at the upper edge of the far wake. Furthermore, no noisy patterns are observed.

### 6.2.2 Gradient-Diffusion Hypothesis Error

The turbulent heat flux corrections are shown in fig. 6.7 together with the LES value and the value from the Gradient-Diffusion Hypothesis (GDH) model. The GDH model only predicts a wall normal heat flux value as the potential temperature only varies in the wall-normal direction. Throughout the entire boundary layer depth,  $q_z^\Delta$  corrects for a turbulent heat flux correction that is too great.

The difference in angle between the GDH and LES turbulent heat fluxes is calculated according to eq. (6.1).

$$\angle q_j^*, q_j^{GDH} = \frac{q_j^* q_j^{GDH}}{|q_j^*| |q_j^{GDH}|} \quad (6.1)$$

This difference is shown in fig. 6.8a together with the ratio of the magnitudes of the two vectors. It can be seen that the angle difference varies from  $70^\circ$  to  $90^\circ$ . The gradient-diffusion hypothesis thus completely fails at predicting the direction of the turbulent heat flux. The ratio of magnitudes ranges from 0.1 to around 5, showing that the constant turbulent Prandtl number is violated. The effect of  $q_j^\Delta$  on the buoyancy production of turbulence is shown in fig. 6.8b. As buoyancy production is governed only by the wall-normal component of the turbulent heat flux, the figure shows essentially the same pattern as the wall-normal part of fig. 6.7. Throughout the entire boundary layer, the GDH model shows exceedingly high values of buoyant destruction.

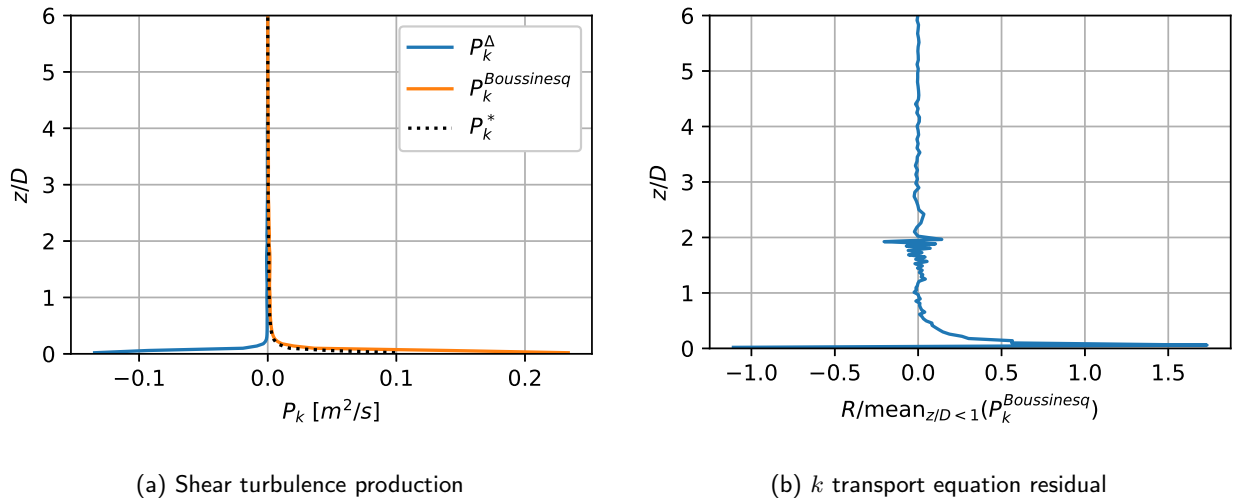


Figure 6.2: Frozen-RANS results for the NBL precursor case

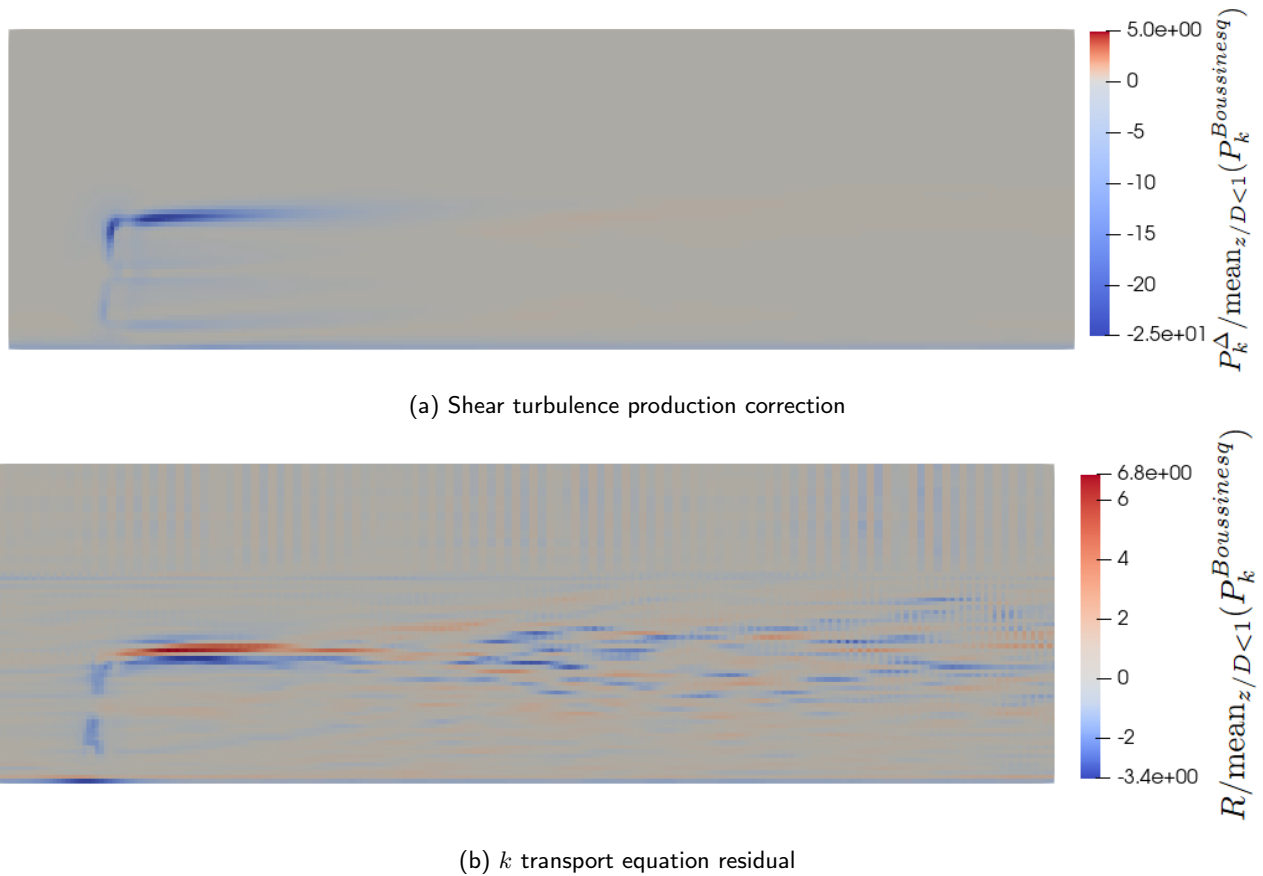


Figure 6.3: Contours of frozen-RANS corrections for NBL wind turbine flow, plotted at  $-1 \leq x/D \leq 9$  relative to the turbine

Figure 6.9 shows contours of the buoyancy production correction in wind turbine flow case. Downstream of the rotor plane, the buoyancy production correction decreases in magnitude compared to the free-stream value. This indicates that the baseline model wall-normal turbulent heat flux shows greater agreement with the LES reference in the near-wake than in the free-stream. This improvement stems from the fact that the LES buoyancy destruction values grow in the wake while the potential temperature, and consequently the GDH buoyancy production, hardly changes in the wake (as is shown in chapter 7). In the far-wake the value of the buoyancy production correction flips sign, indicating the GDH model destroys too little turbulence locally.

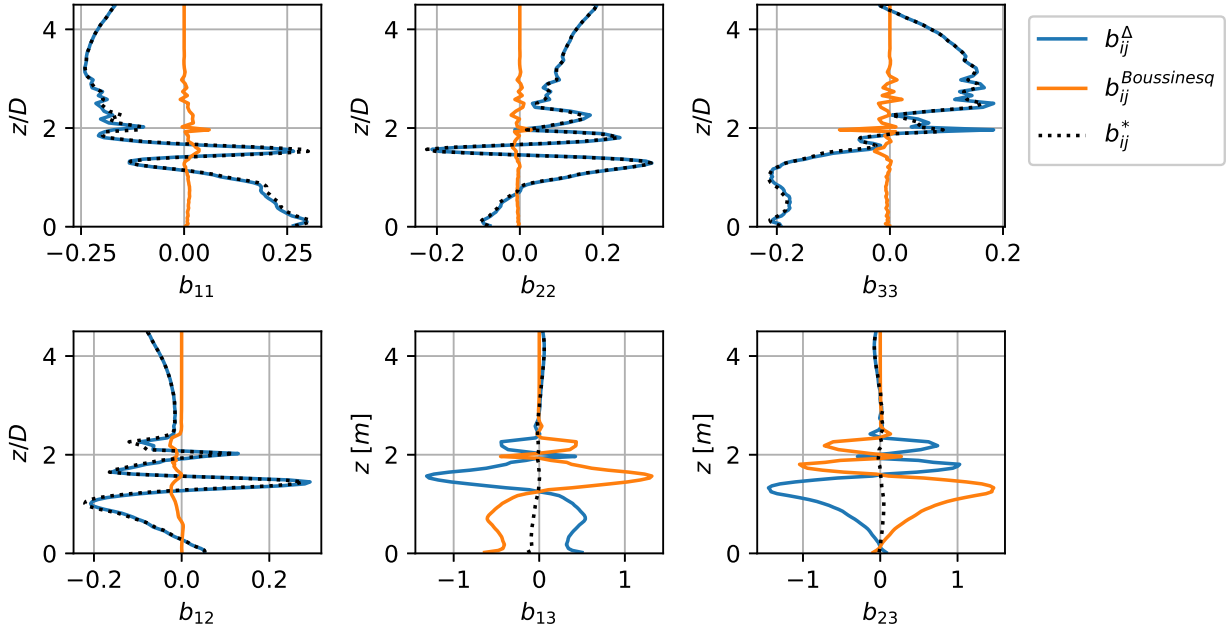


Figure 6.4: Frozen-RANS results for the SBL precursor case showing the normalized anisotropy error

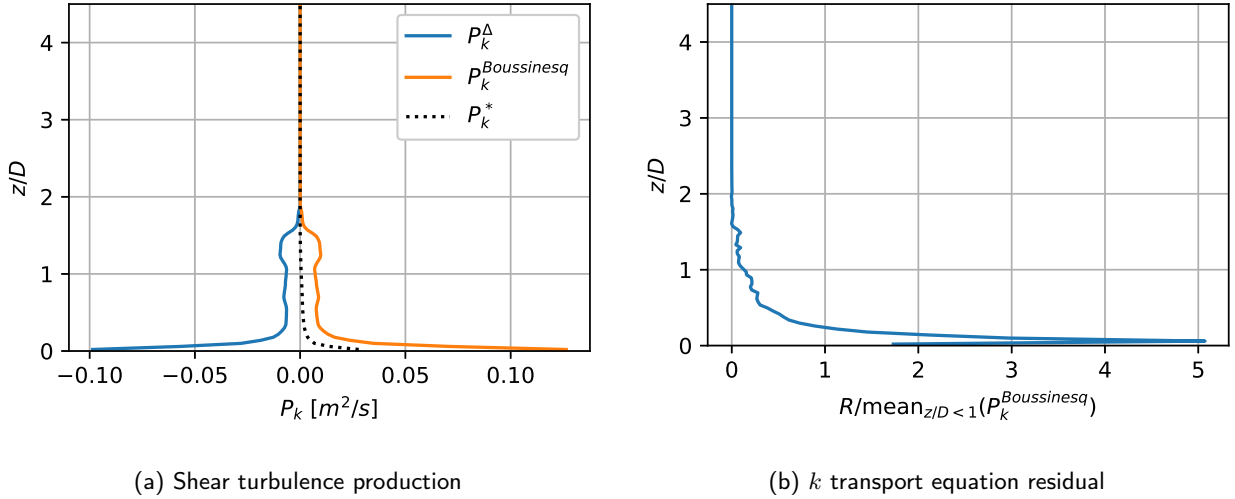


Figure 6.5: Frozen-RANS results for the CBL precursor case

## 6.3 Convective Boundary Layer

### 6.3.1 $k - \epsilon$ Model-Form Errors

fig. 6.10 shows the components of the normalized anisotropy error. As was the case for the NBL and SBL cases, the Boussinesq hypothesis fails in predicting the 11, 22, 33 and 12 components. Additionally, the corrections for the 13 and 23 components are large, particularly around the strong capping inversion. The effect of the anisotropy correction on the shear production of turbulence is visualized in fig. 6.11a. As expected from the anisotropy results, the correction is large primarily at the wall and in the capping inversion. In the capping inversion, the Boussinesq model produces mechanical turbulence, whereas none is produced if the anisotropy is corrected for. At the wall, Boussinesq under-predicts turbulence production. Figure 6.11b shows a mostly negative transport equation residual below the capping inversion with a strong positive very close to the wall. The positive might be a result of the high wall turbulence kinetic energy produced by the SGS model, as discussed in section 5.2.

Figure 6.12a shows the shear production error  $P_k^\Delta$  for the successor case. As was the case in the neutral case, the standard  $k - \epsilon$  model suffers from an overproduction of mechanical turbulence around the rotor. The value of  $P_k^\Delta$  is large at the wall, as was already seen in fig. 6.11a. Figure 6.12b shows contours of the transport equation residual  $R$  in the turbine wake region. Large levels of noise is observed with no clear structure. The noise magnitude seems



(a) Shear turbulence production correction



(b)  $k$  transport equation residual

Figure 6.6: Contours of frozen-RANS corrections for SBL wind turbine flow, plotted at  $-1 \leq x/D \leq 9$  relative to the turbine

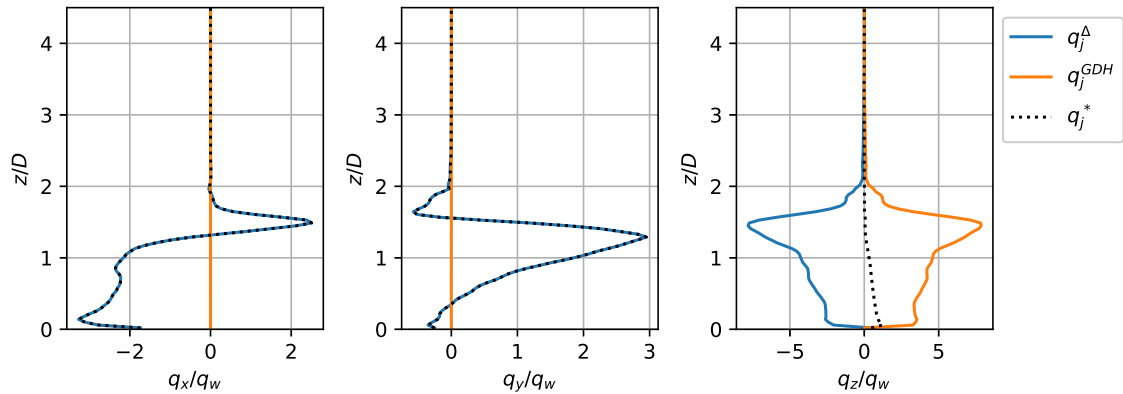
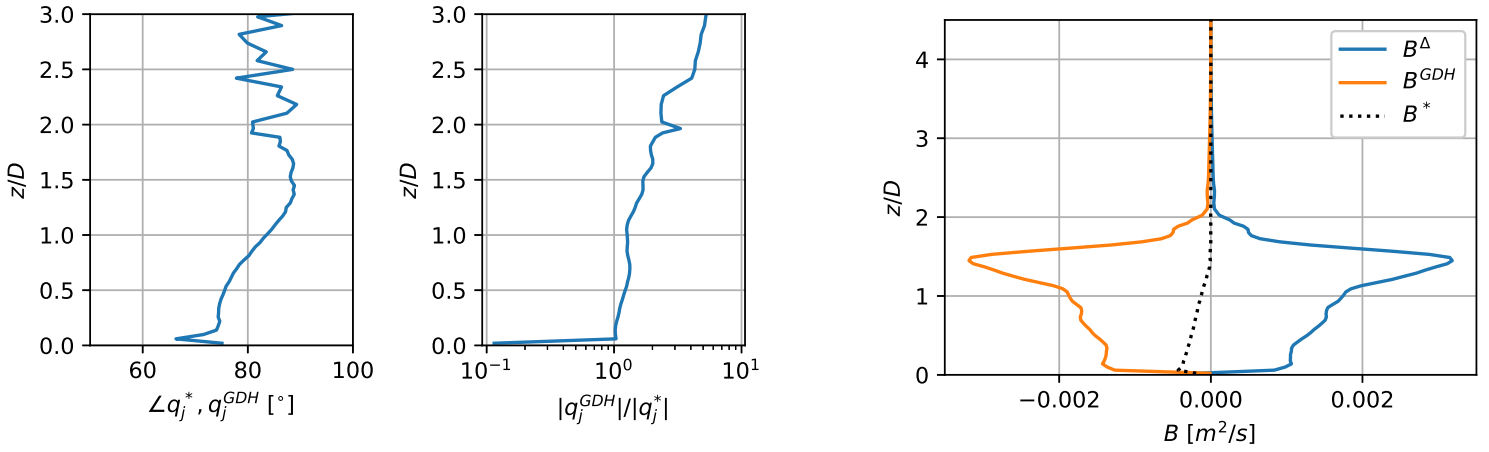


Figure 6.7: Frozen-RANS results for the SBL free-stream flow showing the turbulent heat flux error

to increase considerably in the upper part of the turbine wake. The noise is likely a artefact of oscillations in the time-averaged LES data. Convective boundary layer simulations were performed using a Crank-Nicholson parameter of 0.8 instead of 0.9, with the purpose of preventing such oscillations. Based on these contours, using even lower values is warranted.

### 6.3.2 Gradient-Diffusion Hypothesis Error

The turbulent heat flux errors are shown in fig. 6.13 together with the LES value and the value from the Gradient-Diffusion Hypothesis (GDH) model. Due to the strong vertical temperature gradient in the capping inversion, the GDH model predicts a negative vertical heat flux which is barely present in LES. At the lower wall, the GDH model predicts values much lower than the LES values. In the  $x$  and  $y$  components of the heat flux, the GDH fails to



(a) Angle error (left) and magnitude error (right) of the Gradient-Diffusion Hypothesis model

(b) Effect on buoyant turbulence production

Figure 6.8: Frozen-RANS results for the SBL free-stream flow showing various effects of the turbulence heat flux error

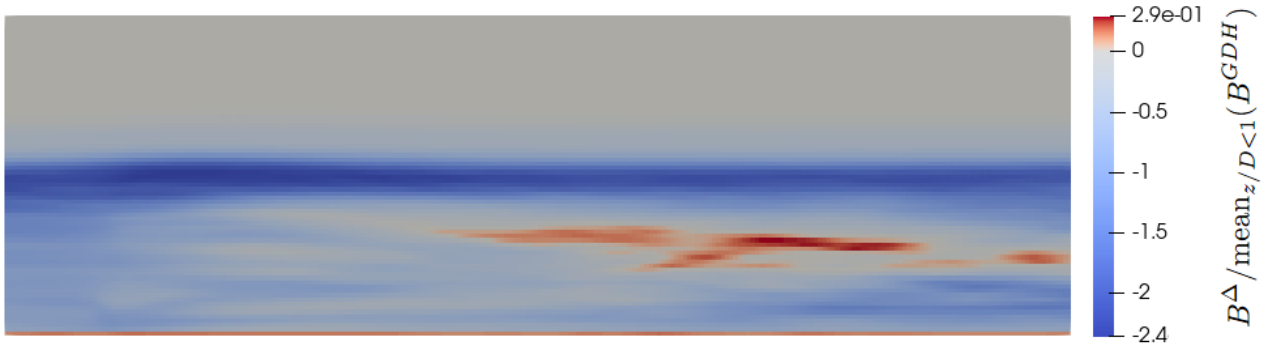


Figure 6.9: Frozen-RANS results for the SBL wind turbine flow showing buoyant turbulence production error, plotted at  $-1 \leq x/D \leq 9$  relative to the turbine

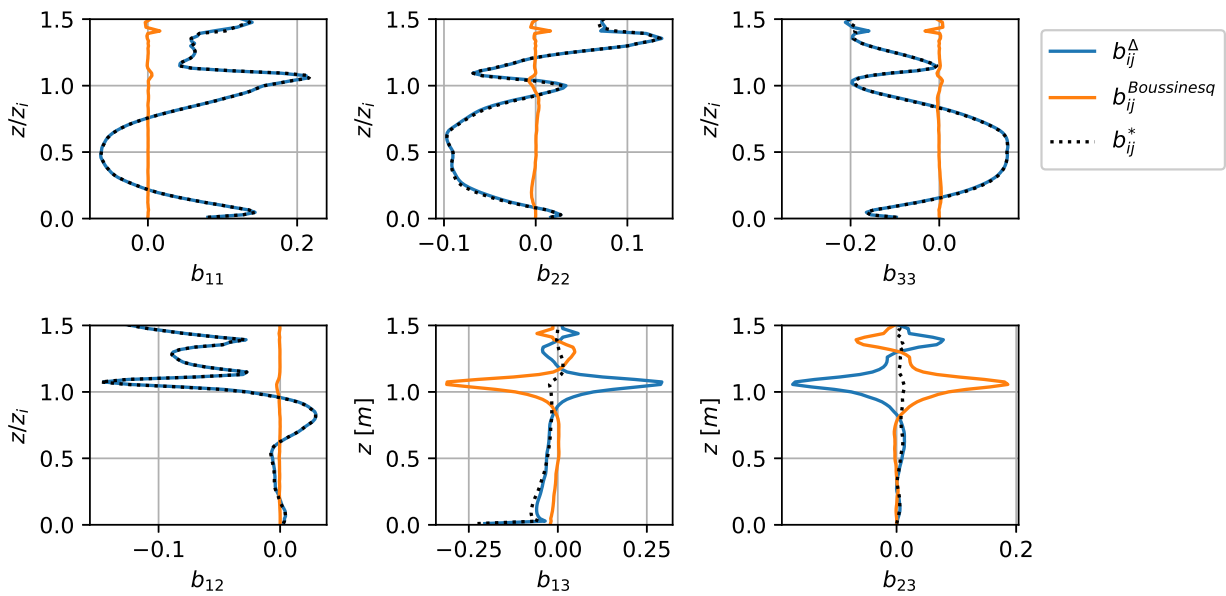


Figure 6.10: Frozen-RANS results for the CBL precursor case showing the normalized anisotropy error

produce any non-zero values since the temperature gradient does not have non-zero wall-parallel components. The angle difference between the GDH and LES heat flux, together with the ratio of magnitude, is shown in fig. 6.14a.

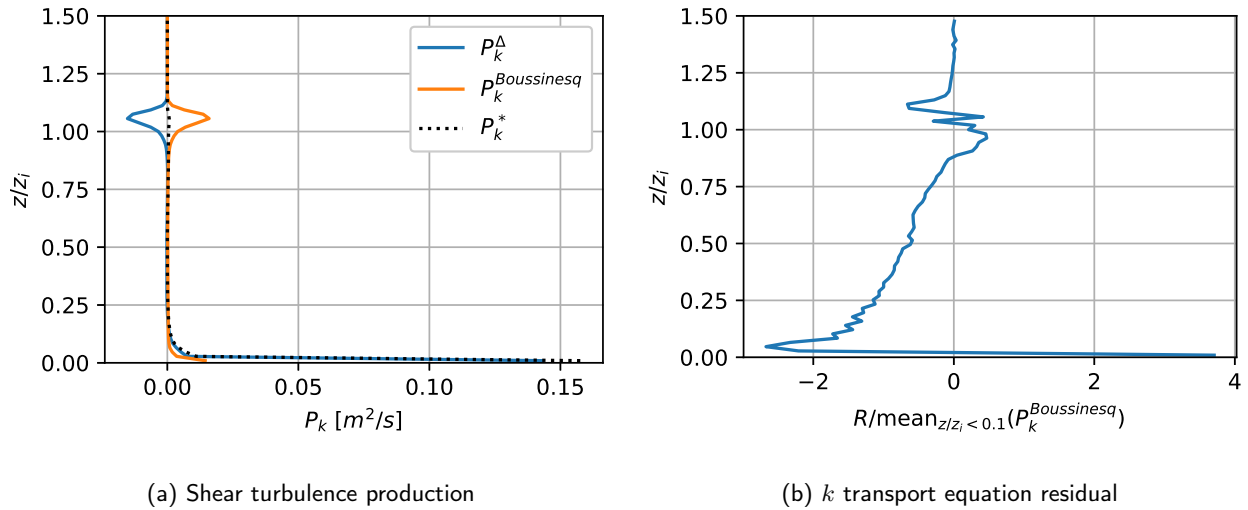


Figure 6.11: Frozen-RANS results for the CBL precursor case

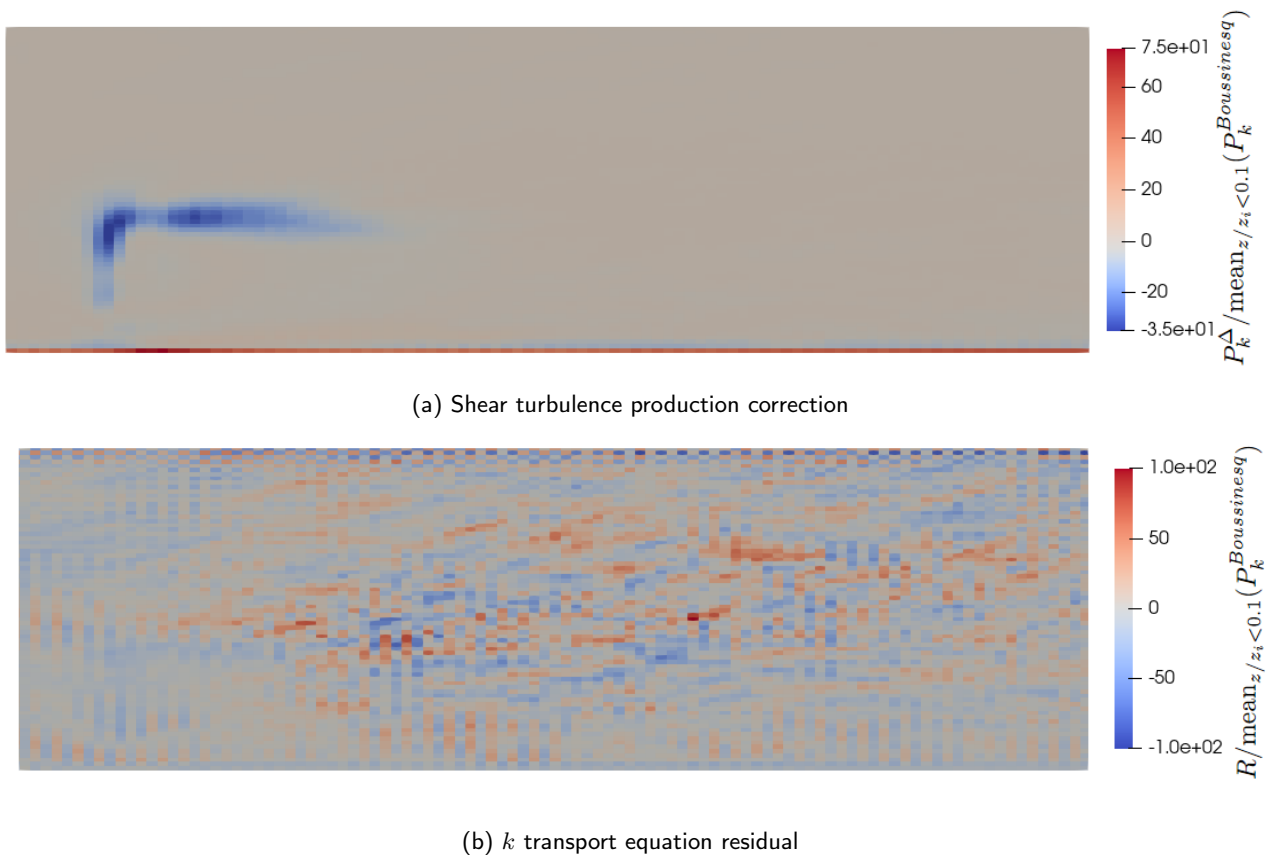


Figure 6.12: Contours of frozen-RANS corrections for CBL wind turbine flow, plotted at  $-1 \leq x/D \leq 9$  relative to the turbine

In the lower part of the boundary layer, the angle error is the lowest with values below  $50^\circ$  since there is a vertical temperature gradient. However, in the absence of this vertical gradient, and in the capping inversion above, the angle error becomes extremely large. It can be concluded that the gradient diffusion hypothesis is an extremely poor model for predicting the turbulent heat flux direction. The magnitude of the GDH heat flux is much lower than the LES value inside the boundary layer and varies greatly as function of height. This suggests that the constant turbulent Prandtl number is inadequate when combined with the gradient-diffusion hypothesis. Figure 6.14b shows the effect of the heat flux error on the buoyant production of turbulence. Due its definition, buoyant turbulence production shows largely the same patterns as the vertical component of the heat flux. GDH predicts high buoyancy production in the capping inversion, while this is barely the case in the LES model. Furthermore, GDH severely under-predicts buoyancy production in the lower part of the boundary layer.

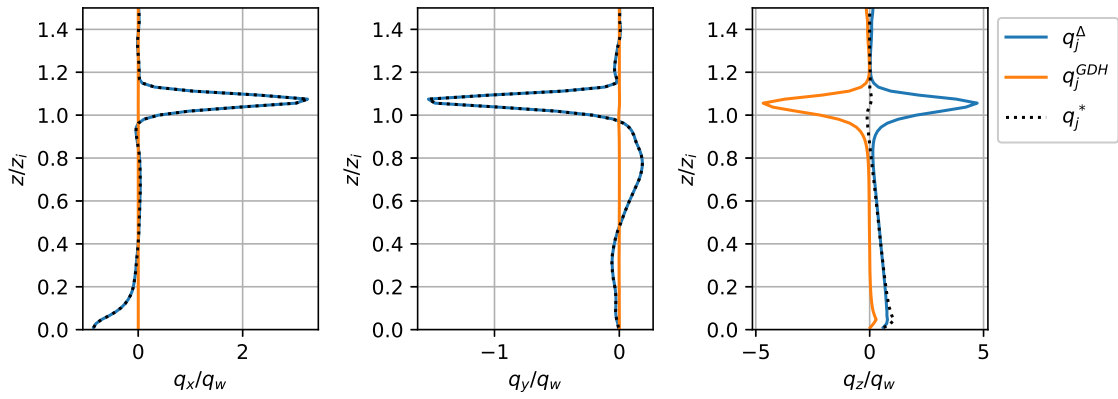
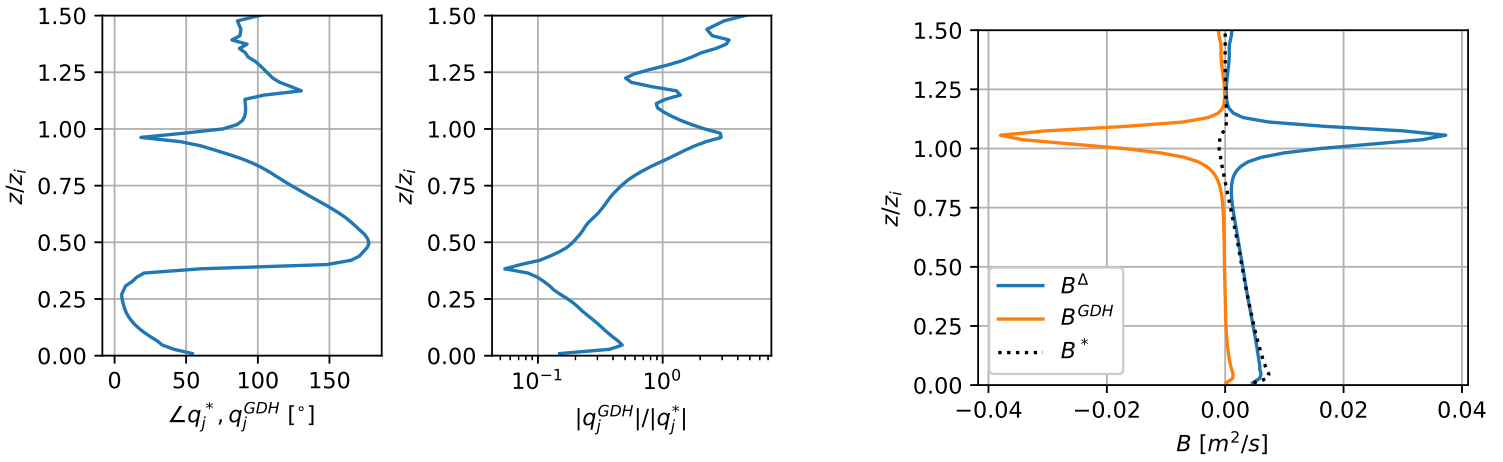


Figure 6.13: Frozen-RANS results for the CBL precursor case showing the turbulent heat flux error



(a) Angle error (left) and magnitude error (right) of the Gradient-Diffusion Hypothesis model

(b) Effect on buoyant turbulence production

Figure 6.14: Frozen-RANS results showing various effects of the turbulence heat flux error, plotted at  $-1 \leq x/D \leq 9$  relative to the turbine

Contour plots of the buoyancy production correction are shown in fig. 6.15. The value increases slightly in the upper region of the wind turbine wake as was also the case in the stable boundary layer wind turbine wake. Additionally, small negative values are observed right above the wall. This pattern is not seen in the free-stream solution shown in fig. 6.14b. Besides the presence of the turbine, the likely reason for this discrepancy is that the successor simulation uses a much finer mesh resolution of  $\Delta_z = 5 \text{ m}$  around the wind turbine compared to the  $\Delta_z = 20 \text{ m}$  of the precursor simulation.

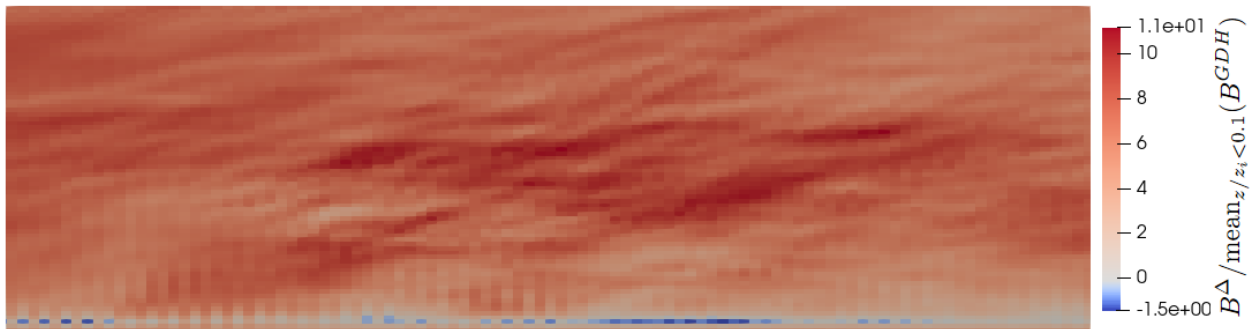


Figure 6.15: Frozen-RANS results for the CBL successor case showing buoyant turbulence production error

# Corrected RANS

In this chapter, the corrections to the baseline turbulence model are inserted dynamically into the RANS simulation to obtain corrected RANS solutions. The results are compared to results obtained by the baseline uncorrected  $k - \epsilon$  model and to time-averaged LES results. For all three stability cases, a distinction is made between the free-stream flow and the successor flow.

## 7.1 Neutral Boundary Layer

### 7.1.1 Free-Stream Flow

The velocity components are plotted in fig. 7.1a. Both the baseline model and the corrected model agree well with the reference. For the turbulent kinetic energy, shown in fig. 7.1b, the corrected model matches the reference. The baseline model has a slightly lower TKE in the lower part of the boundary layer.

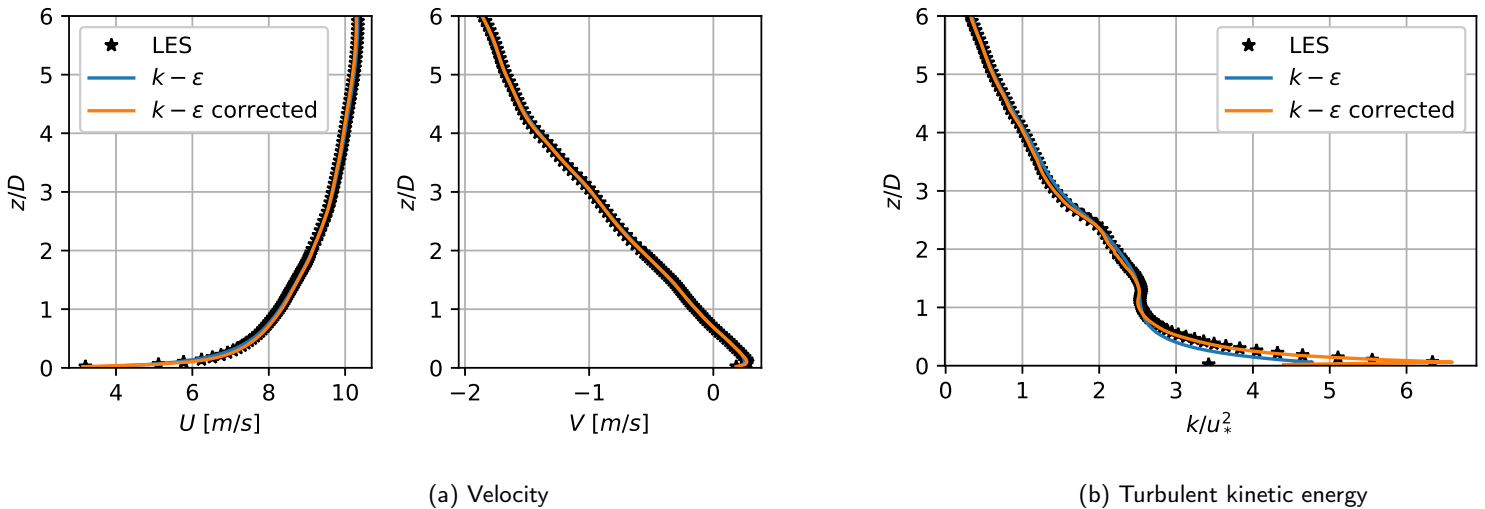


Figure 7.1: Free-stream CBL corrected RANS profiles compared to the baseline and to LES

The Reynolds stress components are shown in fig. 7.2. The corrected model shows near-perfect agreement with LES for each component. The baseline model only produces an adequate match for the  $xz$  component. The  $xx$ ,  $yy$  and  $zz$  have the same values since in the definition of the Reynolds stress, shown in eq. (7.1), the strain rate tensor only has non-zero  $xz$  and  $yz$  components.

$$\overline{u'_i u'_j} = \frac{2}{3} k \delta_{ij} - 2\nu_t S_{ij} \quad (7.1)$$

### 7.1.2 Wind Turbine Flow

Figure 7.3 shows wall-normal wake velocity deficit in the top set of plots and lateral wake velocity deficit in the bottom set. Results are shown 2, 5 and 9 diameters  $D$  downstream of the wind turbine. The thin black lines indicate the rotor center and the upper and lower or north and south edge of the wind turbine rotor. The corrected model shows

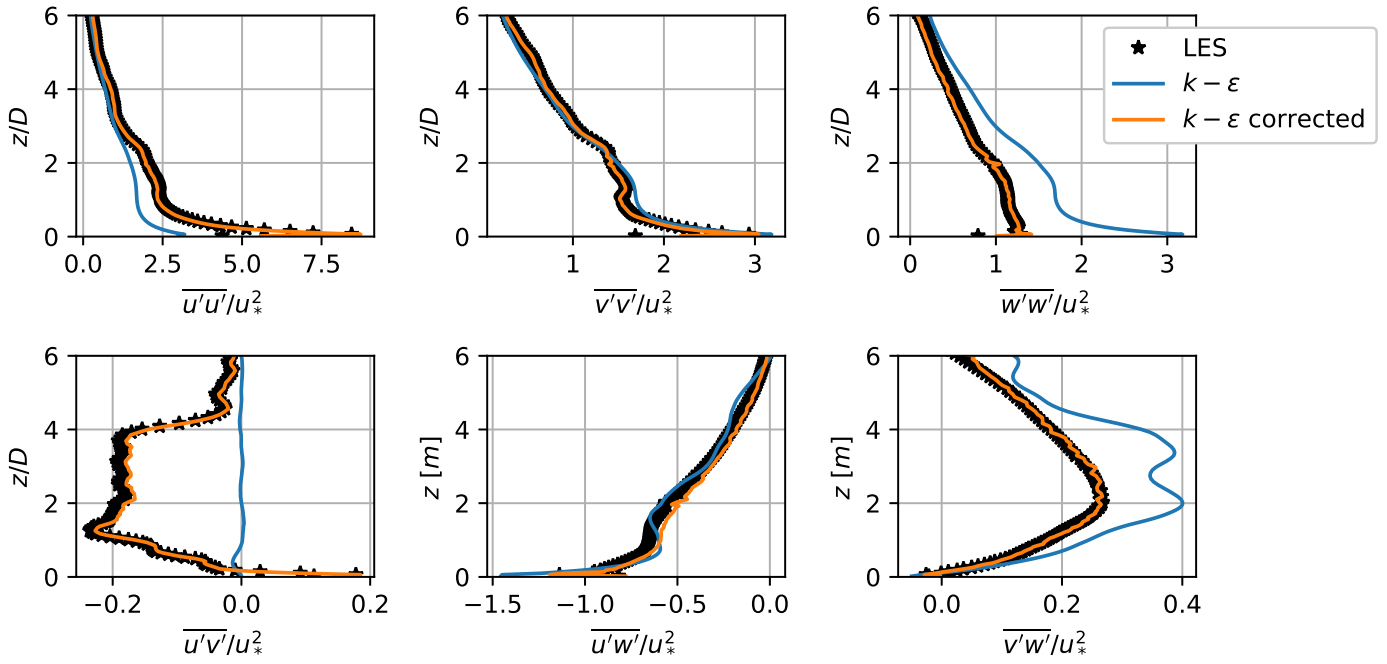


Figure 7.2: Corrected RANS Reynolds stress results for the free-stream NBL case

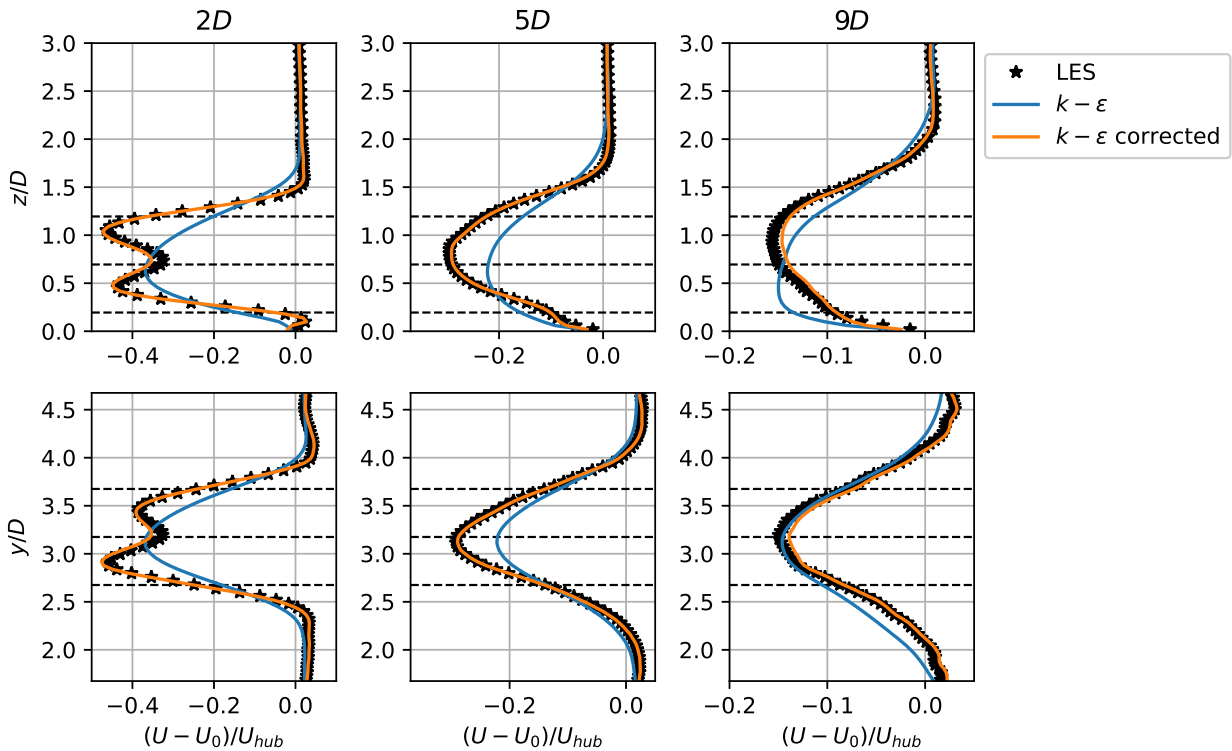


Figure 7.3: Corrected RANS wake velocity deficit profiles for the NBL case

good agreement at all stations and adequately handles the shortcomings of the baseline model, which produces a lower wake velocity deficit in the near wake. Interestingly, at  $9D$  downstream of the turbine, both the baseline and corrected model produce a correct velocity deficit magnitude, but it is only the corrected model that produces profiles with the correct shape.

The wake turbulent kinetic energy profiles are shown in ???. The corrected model shows near-perfect agreement with the reference. In the near wake, the turbulent kinetic energy of the baseline model is much larger throughout the height and width around the turbine. The overproduction of mechanical turbulence was observed in fig. 6.3a as a very

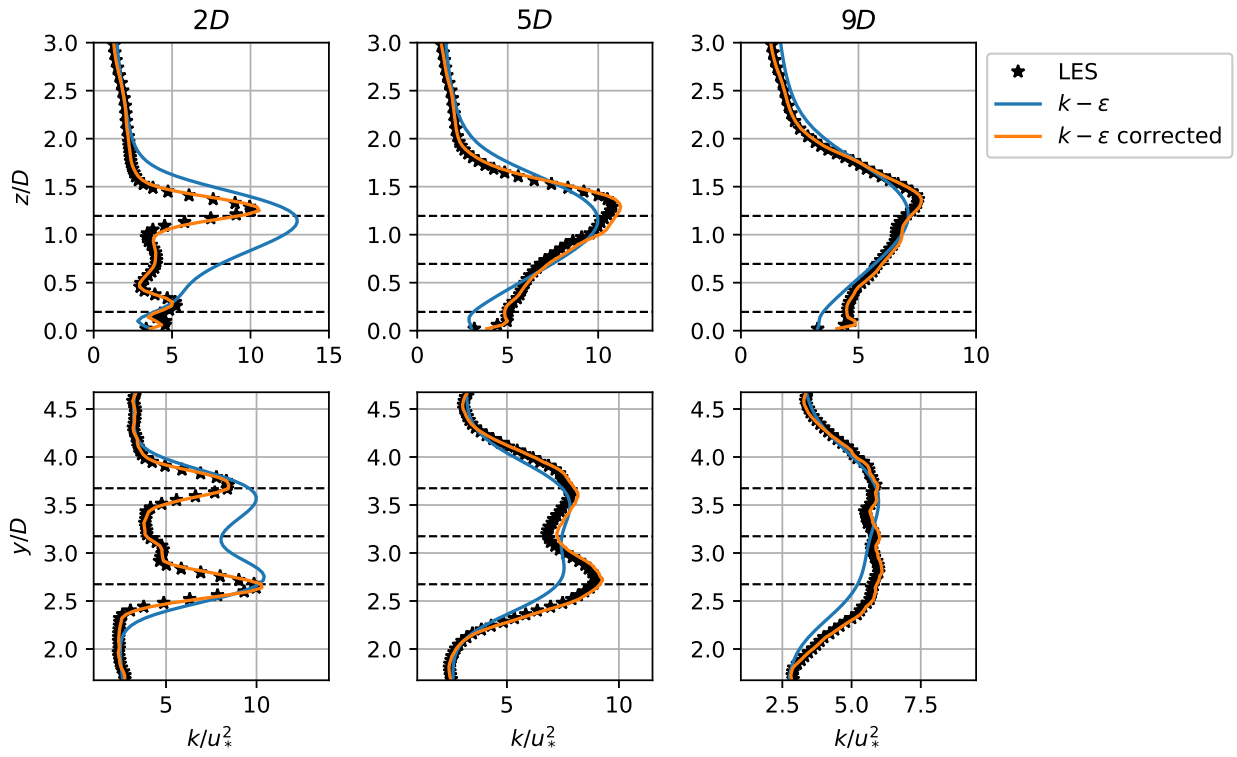


Figure 7.4: Corrected RANS horizontal wake turbulent kinetic energy profiles for the NBL case

local effect;  $P_k^\Delta$  was negative only around the wind turbine rotor and at the upper part of the near wake. As such, both the TKE and the velocity show large discrepancies with the reference in the near wake.

## 7.2 Stable Boundary Layer

In this section, three different methods of inserting the frozen-RANS obtained corrections are tested. The first method is inserting the full set of corrections:  $b_{ij}^\Delta$ ,  $R$  and  $q_j^\Delta$ . In the second method, a simplification is made in the correction to the turbulent heat flux; only the wall-normal component  $q_3^\Delta$  is injected instead of the full vector correction. In the third method, the turbulent heat flux is not corrected at all.

### 7.2.1 Free-Stream Flow

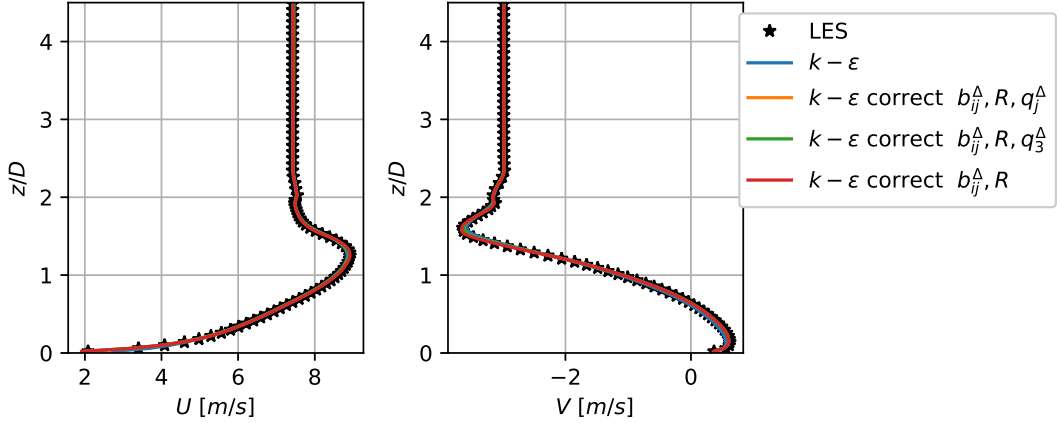


Figure 7.5: Corrected RANS velocity results for the free-stream SBL case

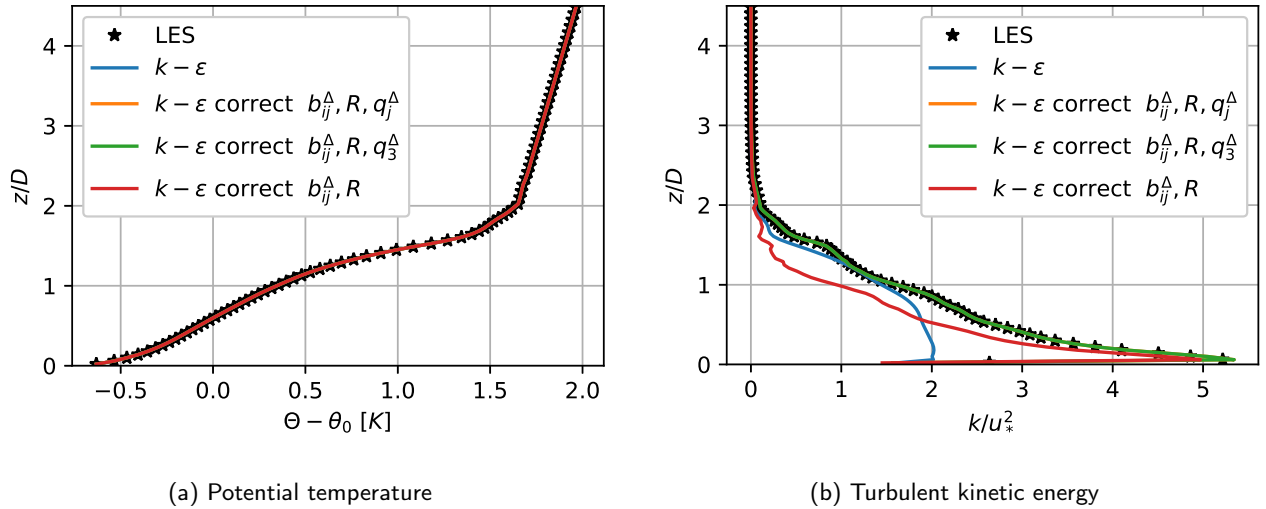


Figure 7.6: Free-stream SBL corrected RANS profiles compared to the baseline and to LES

The corrected  $k - \epsilon$  model results for free-stream velocity are shown in fig. 7.5. All models agree well with the reference values, even the baseline  $k - \epsilon$  model. Even though the baseline models shows discrepancies with LES for the momentum fluxes, it appears that the profiles do not evolve much due to the short stream-wise length of the precursor domain. Similarly, the potential temperature, shown in fig. 7.6a, does not evolve regardless of heat flux discrepancies. Figure 7.6b shows how the baseline model has a lower peak TKE in the lower part of the boundary layer. As is the case with Reynolds stress, shown in fig. 7.7, both models 'correct  $b_{ij}^\Delta, R, q_j^\Delta$ ' and 'correct  $b_{ij}^\Delta, R, q_3^\Delta$ ' agree perfectly with the reference. The model that does not correct for the heat flux shows a lower TKE in the upper region of the stable boundary layer as well as discrepancies in the Reynolds stress. The lower TKE is explained by the larger values of buoyant destruction due to the larger heat flux magnitude values seen in fig. 7.8. In the same figure, only the model with the full corrections reproduces all heat flux components accurately. As expected, the models 'correct  $b_{ij}^\Delta, R, q_3^\Delta$ ' and 'correct  $b_{ij}^\Delta, R$ ' do not produce any non-zero value of wall-parallel heat flux due to their definition. It can be concluded that a scalar correction to the wall-normal heat flux is sufficient for obtaining accurate velocity, TKE and Reynolds stress results, at least for the free-stream flow.

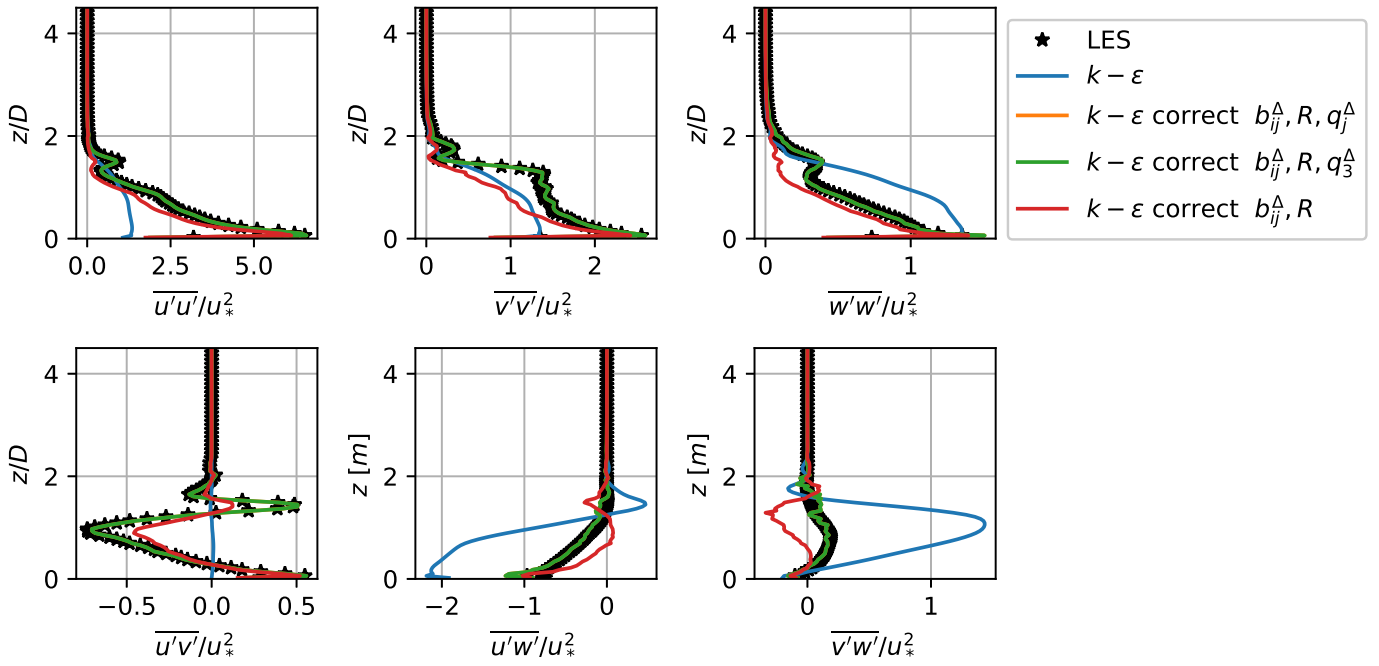


Figure 7.7: Corrected RANS Reynolds stress results for the free-stream SBL case

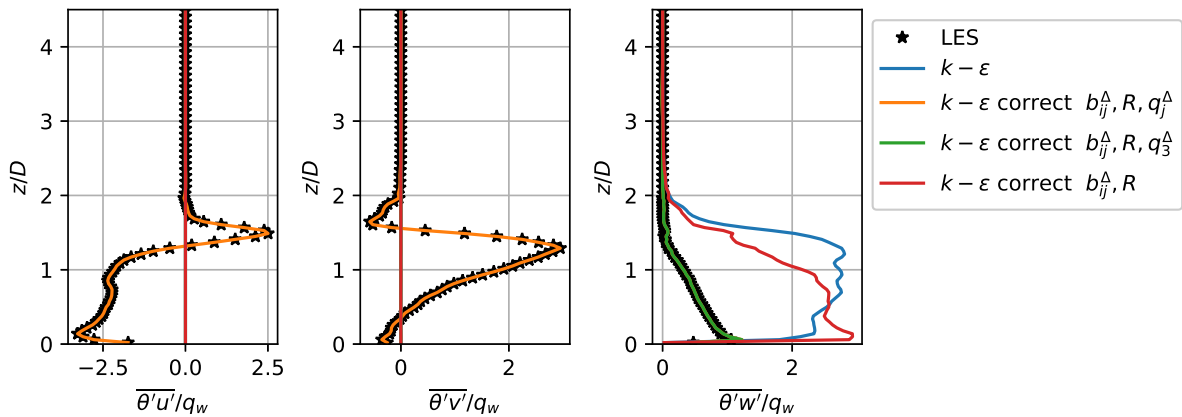


Figure 7.8: Corrected RANS turbulent heat flux results for the free-stream SBL case

## 7.2.2 Wind Turbine Flow

Wake velocity deficit profiles are shown in fig. 7.9. All corrected models show generally good agreement with the reference, with the models that included the heat flux correction showing slightly better agreement. The RANS models show a small discrepancy with the LES values at and right above the wall in the far wake. Interestingly, this pattern was not at all observed for the neutral case. A further discussion on the matter is provided in section 7.6. The baseline model produces an adequate wake velocity deficit magnitude, but only in the very near wake. In the far-wake, the velocity deficit is over-predicted by the baseline model due to a severely under-predicted turbulent kinetic energy in all regions of the wake, as is seen in fig. 7.10. The corrected modules that include the heat flux correction show perfect TKE agreement, while the agreement is good but slightly worse for the corrected model that does not include a heat flux correction. Similar patterns are seen for the  $xz$  component of the Reynolds stress, shown in fig. 7.11. Although the heat flux corrections are by no means negligible, the main driver for velocity, kinetic energy and Reynolds stress improvements is the correction to the normalized Reynolds stress anisotropy and the transport equation Residual.

The wake potential temperature profiles in fig. 7.12 are shown to be insensitive to the choice of model. As was the case for the free-stream flow, the errors of the baseline model do not accumulate noticeably over the span-wise length of the domain. Since some spatial variation is observed, convective and diffusive transport seems to dominate the turbulent transport of the potential temperature.

The wall-normal heat flux profiles are shown in fig. 7.13. The baseline  $k-\epsilon$  model fails to produce accurate heat flux

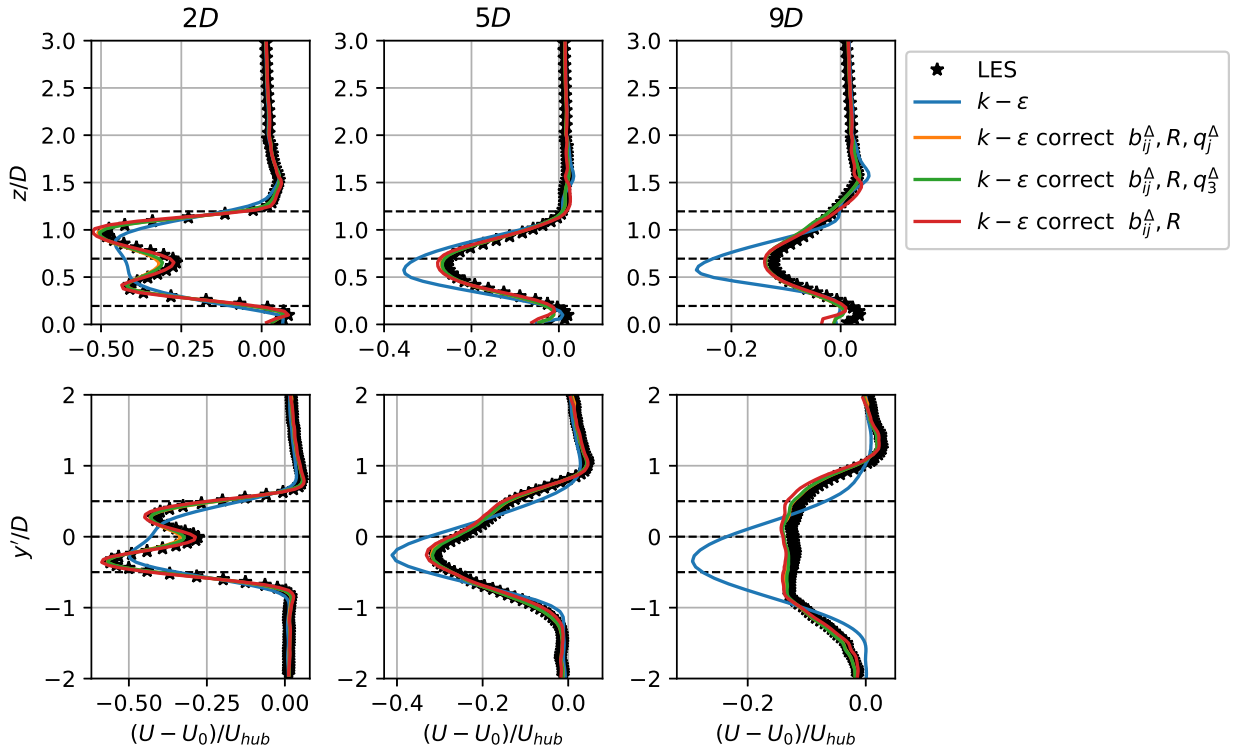


Figure 7.9: Corrected RANS wake velocity deficit profiles for the SBL case

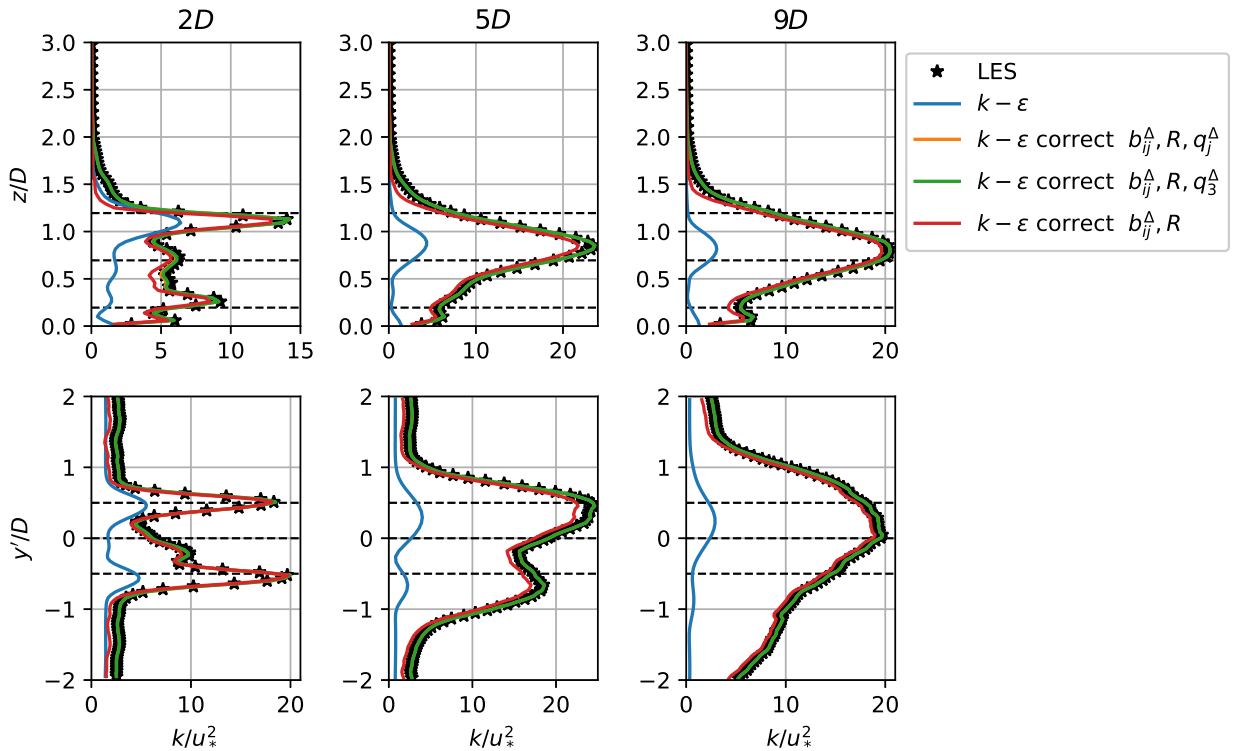


Figure 7.10: Corrected RANS wake turbulent kinetic energy profiles for the SBL case

results at all stations. The models that include the heat flux correction show perfect agreement. The model that excludes the heat flux correction only shows large discrepancies in the near wake, resulting in buoyancy destruction values that are larger than the reference LES. This leads to the slightly lower TKE observed in fig. 7.10 and the slightly higher wake deficit observed in fig. 7.9.

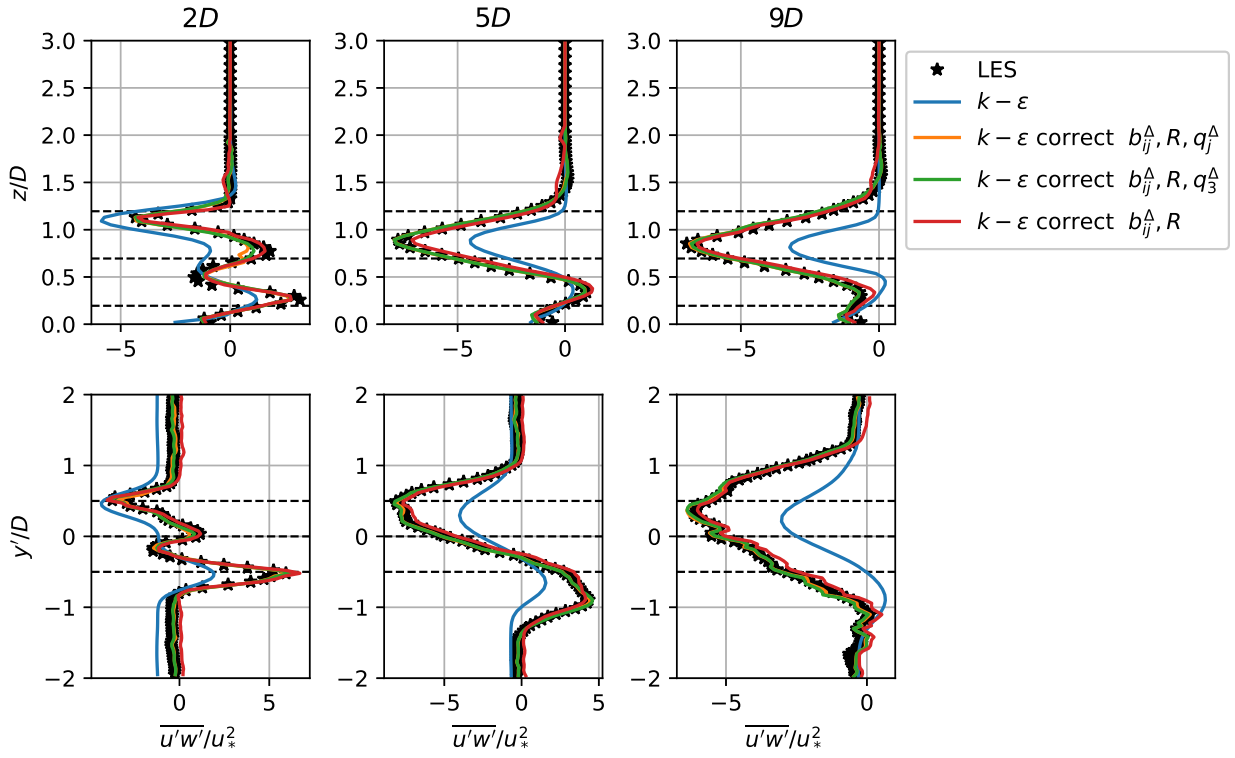


Figure 7.11: Corrected RANS wake Reynolds stress  $xz$ -component profiles for the SBL case

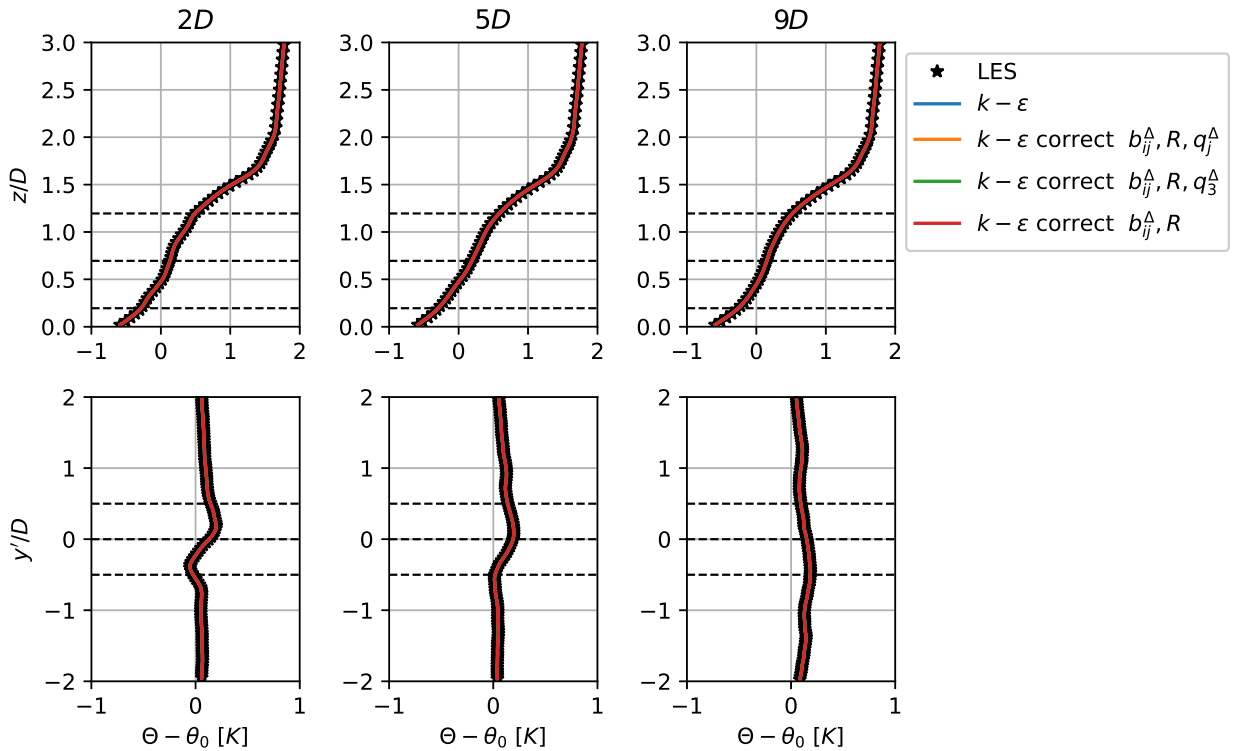


Figure 7.12: Corrected RANS wake potential temperature profiles for the SBL case

### 7.3 Convective Boundary Layer

In this section, a distinction is made between corrected  $k-\epsilon$  cases depending on where in the domain the model-form corrections are applied. To this extent, the blending functions  $F_b$  is set to 0 where the anisotropy corrections are not

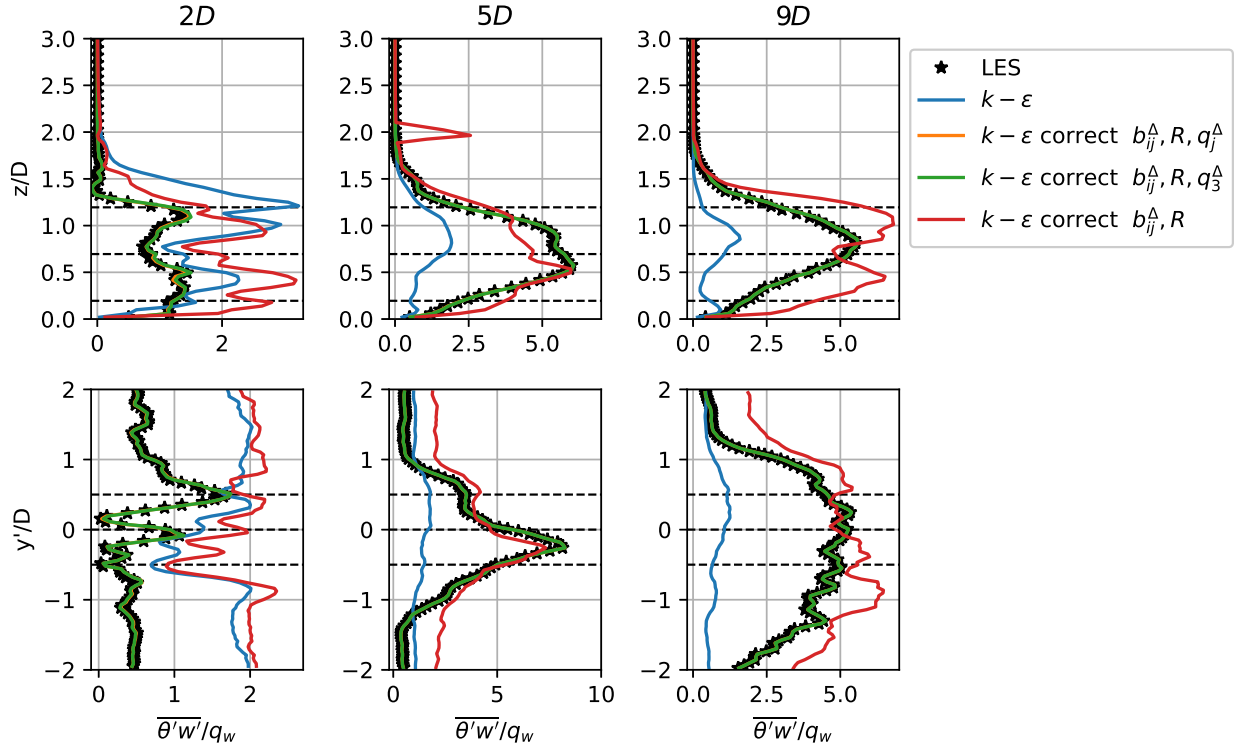


Figure 7.13: Corrected RANS wake wall-normal heat flux profiles for the SBL case

applied. Equation (4.24) shows how the corrections from the frozen case are applied to the RANS simulations. The equation is repeated here.

$$\begin{aligned}\tilde{R} &= \gamma_R F_R R \\ \tilde{b}_{ij}^{\Delta} &= \gamma_b F_b b_{ij}^{\Delta} \\ \tilde{q}_j^{\Delta} &= \gamma_q F_q q_j^{\Delta}\end{aligned}$$

As with the other stability cases, all blending functions are set to 0 within 30  $m$  of the upper wall. For the case labelled ' $k - \epsilon$  corr.  $b_{ij}^{\Delta}$  20  $m$ ', the term  $F_b = 0$  below  $z = 20$   $m$ . Similarly, ' $k - \epsilon$  corr.  $b_{ij}^{\Delta}$  10  $m$ ' indicates  $F_b = 0$  for  $z < 10$   $m$ . For the case labelled ' $k - \epsilon$  corrected', all corrections are applied until the lower wall.

### 7.3.1 Free-Stream Flow

The velocity profiles for the free-stream CBL case are shown in fig. 7.14. Corrected case  $b_{ij}^{\Delta}$  20  $m$  and the baseline case both match the reference. The standard corrected case, however, shows a sharp discontinuity at the wall. Since turning off the anisotropy correction at the wall improves the results, the issue is likely a cascading effect of the nonphysical total stress tensor at the wall in the CBL case.

The discontinuity observed in the velocity profile is also observed in the kinetic energy and Reynolds stress profiles, shown in fig. 7.15b and fig. 7.16. Not applying the anisotropy correction below  $z = 20$   $m$  does improve the profiles, but does not provide a perfect match. In particular, the turbulent kinetic energy and the  $xx$ ,  $yy$  and  $xz$  components of the Reynolds stress show lower near-wall values. Not applying the corrections locally seems to result in the respective variables closer matching the baseline RANS values. Both corrected models show good agreements for the vertical heat flux in fig. 7.17, The standard corrected model shows slightly higher at the peak than the reference LES.

The potential temperature distribution is shown in fig. 7.15a. In a domain of this size, the temperature is insensitive to the model chosen as the errors do not accumulate sufficiently to influence the temperature within the distance from the inflow plane to the outflow plane. The effect of the scalar heat flux correction to the potential temperature transport equation would likely be more evident if the domain was several kilometers long.

### 7.3.2 Wind Turbine Flow

Figure 7.18 shows the velocity deficit profiles in the wake at 2D, 5D and 9D downstream of the rotor plane. The baseline  $k - \epsilon$  model shows a reasonable near wake agreement but a much lower wake recovery rate. The corrected

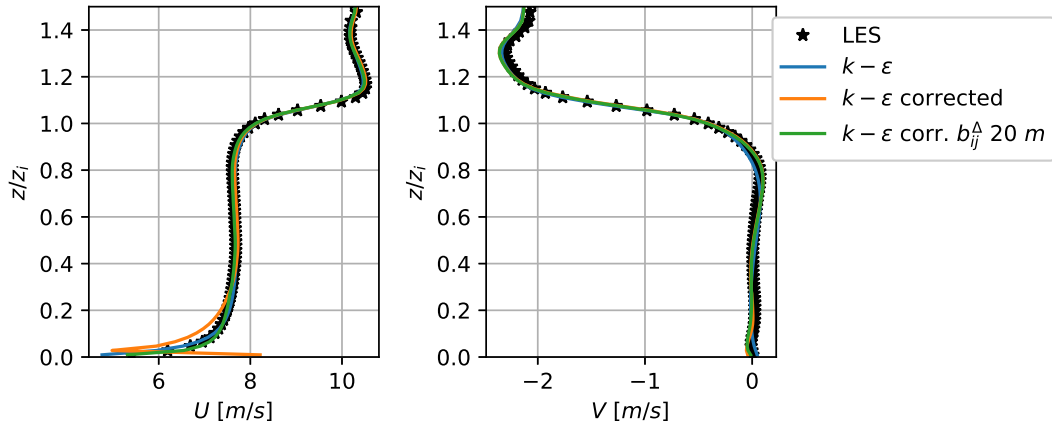


Figure 7.14: Corrected RANS velocity results for the free-stream CBL case

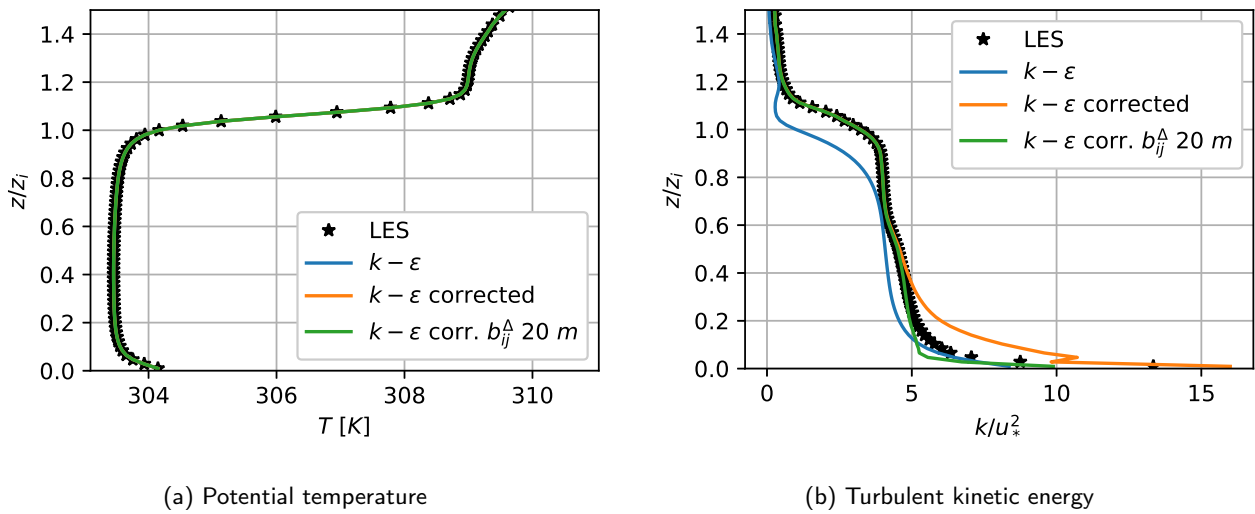


Figure 7.15: Free-stream CBL corrected RANS profiles compared to the baseline and to LES

models show agreement away from the wall but sharp discontinuities close to the wall, particularly at  $5D$  and  $9D$ . Unlike for the free-stream flow, moving up the application region for  $b_{ij}^{\Delta}$  does not improve the solution quality. It instead results in the profiles sharply transitioning to, and even overshooting, the baseline  $k - \epsilon$  value. In the lateral velocity deficit profiles, all corrected RANS models show some disagreement with the LES reference on the south end. In the middle of the domain, however, the match with LES is much closer and constitutes a significant improvement over the baseline model.

The TKE profiles are plotted in fig. 7.19. The baseline model shows an under-prediction in TKE in the near wake and above the wake. The turbulence under-prediction is the primary driver for the slow wake recovery observed in the velocity deficit profiles. The corrected RANS models all show better agreement with the LES reference away from the wall. At the wall, the values significantly exceed the LES value, including for the baseline RANS case. Particularly at  $2D$ , the wall TKE value for the standard  $k - \epsilon$  corrected model has a considerable magnitude. The pattern is similar to the pattern observed for the corrected RANS free-stream wall TKE in fig. 7.15b, although there the agreement with the LES reference was better. It seems that introducing the anisotropy correction further away from the wall does not improve the TKE predictions, since the baseline RANS model performs rather poorly at the wall as well. In the lateral TKE profiles, shown in ??, the corrected RANS discrepancies grow larger towards the south end.

The wall-normal turbulent heat flux is plotted in fig. 7.21. In the wake profiles, the effect of the turbine is hardly visible. Only a small change in flux is observed at the  $2D$  station for the GDH flux. As was the case with the free-stream flow, the baseline severely under-predicts wall-normal heat flux, resulting in lower buoyancy production, lower wake TKE and lower wake recovery. At the wall, there is some discrepancy between the corrected RANS heat flux and the reference heat flux. As the potential temperature profiles, shown in fig. 7.22, agree well with the reference, and turbulent Prandtl number is constant across models, the observed discrepancy is a product of a discrepancy in

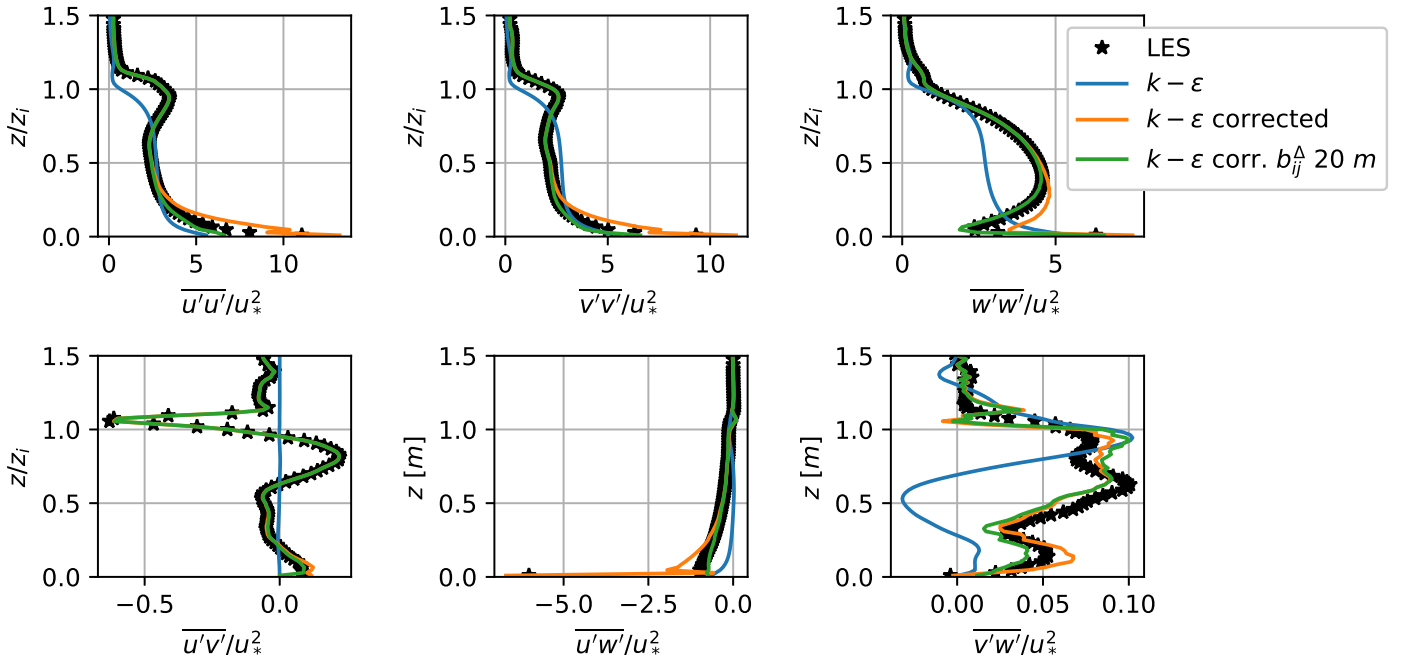


Figure 7.16: Corrected RANS Reynolds stress results for the free-stream CBL case

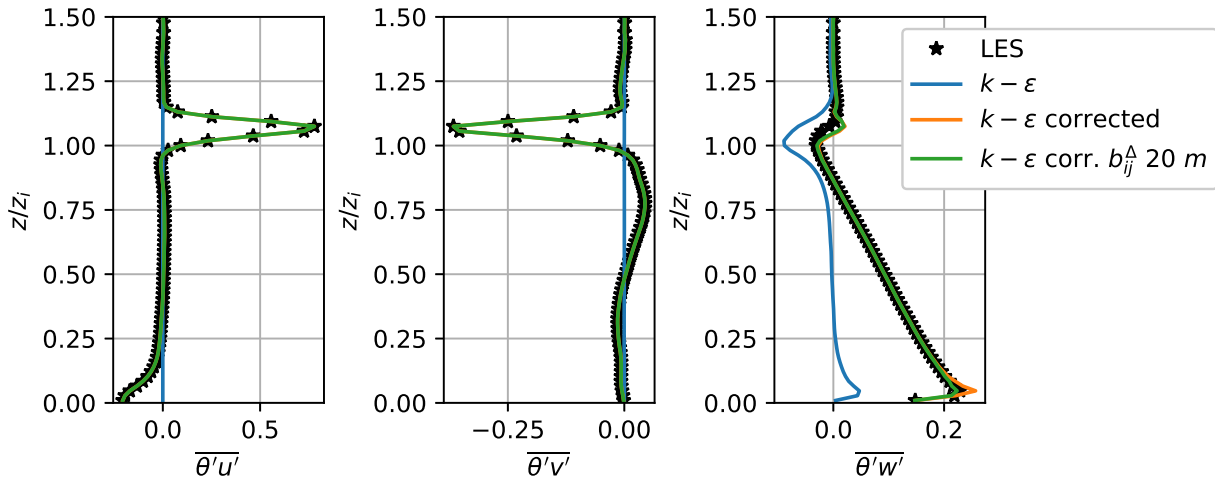


Figure 7.17: Corrected RANS turbulent heat flux results for the free-stream CBL case

the eddy viscosity  $\nu_t$  between the frozen-RANS and the dynamic corrected RANS.

$$q_j = q_j^{GDH} + q_j^\Delta = -\frac{\nu_t}{Pr_t} \frac{\partial \Theta}{\partial x_j} + q_j^\Delta$$

In fig. 7.23 the dynamic RANS eddy viscosity is compared to the eddy viscosity obtained from frozen-RANS. It does appear to be slightly lower than the reference value, but not to the same extent or with the same shape as the difference seen in fig. 7.22. Some other effects, possibly related to the wall velocity and kinetic energy mismatch, might be at play.

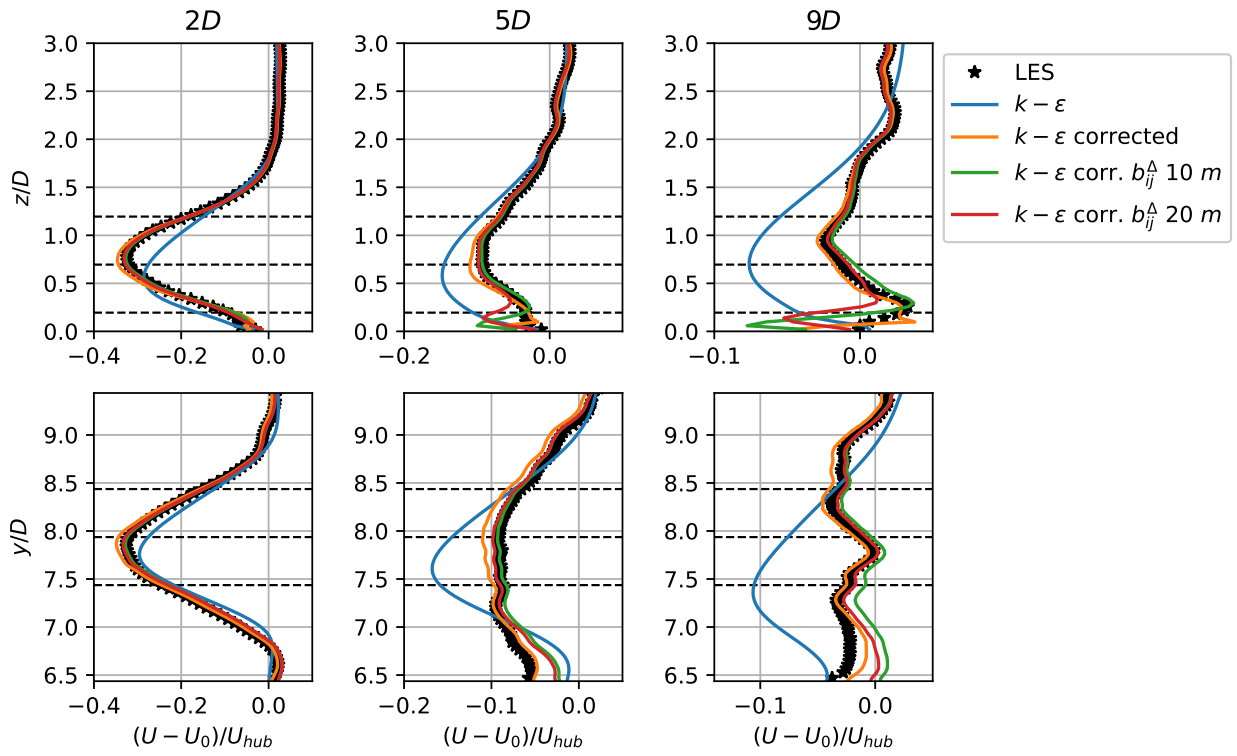


Figure 7.18: Corrected RANS wake velocity deficit profiles for the CBL case

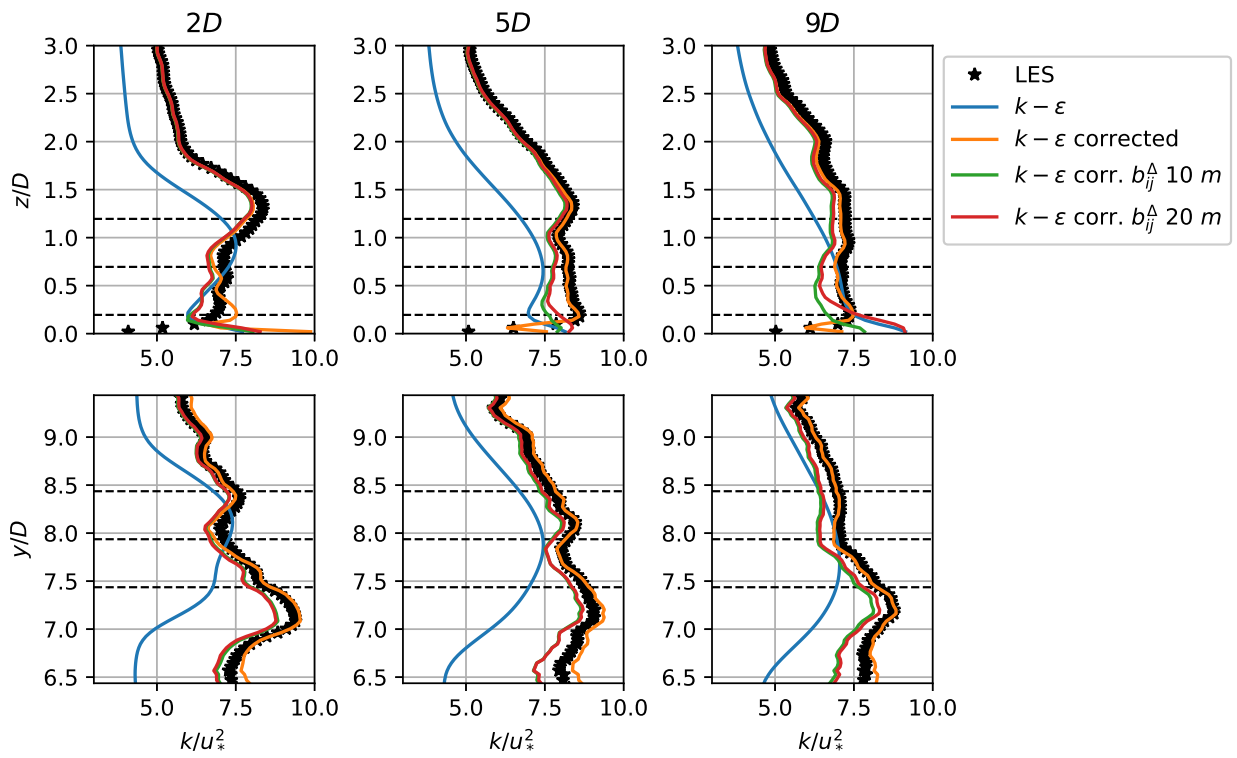


Figure 7.19: Corrected RANS wake turbulent kinetic energy profiles for the CBL case

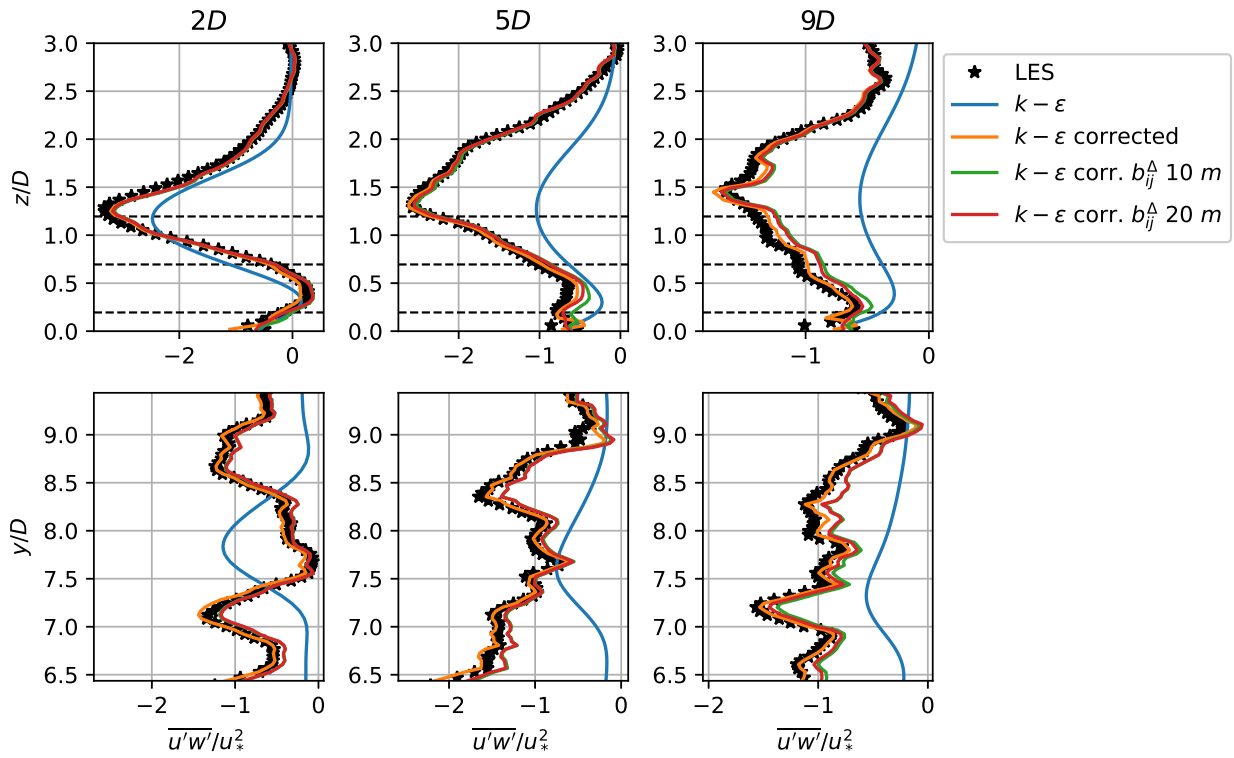


Figure 7.20: Corrected RANS wake Reynolds stress  $xz$ -component profiles for the CBL case

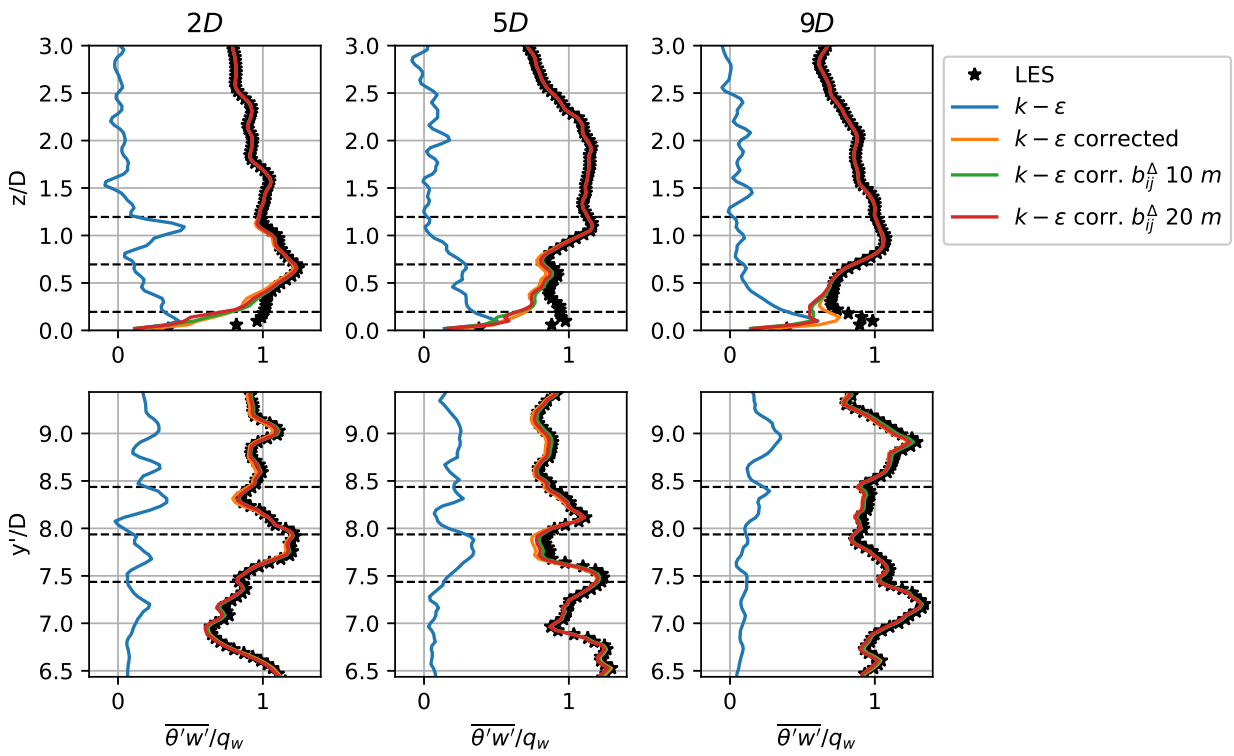


Figure 7.21: Corrected RANS wake wall-normal turbulent heat flux profiles for the CBL case

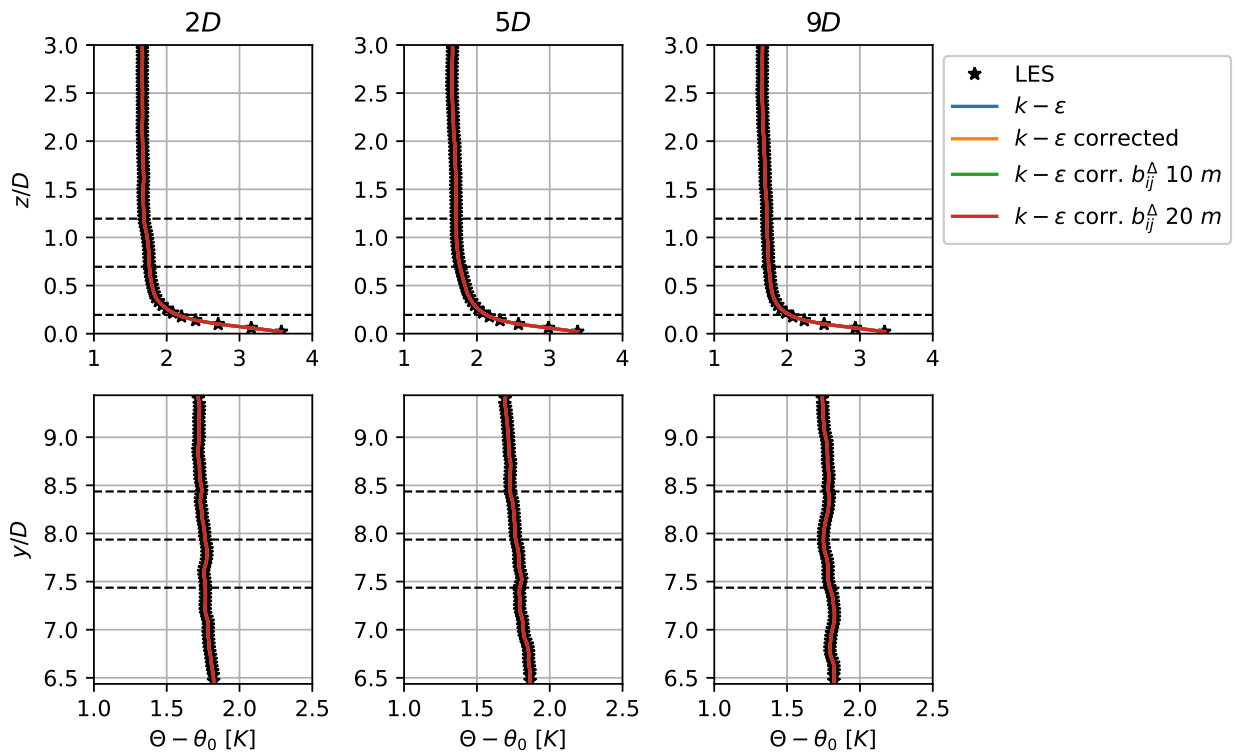


Figure 7.22: Corrected RANS wake potential temperature profiles for the CBL case

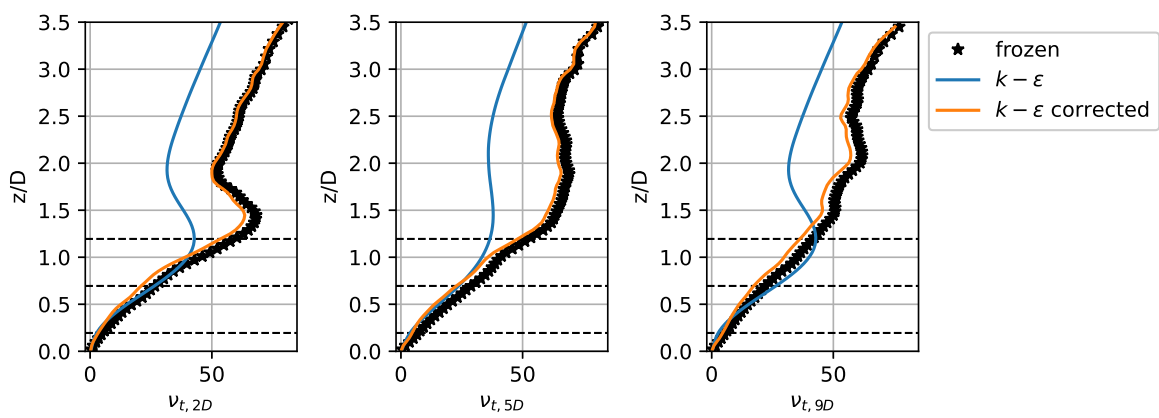


Figure 7.23: Corrected RANS wake eddy viscosity for the CBL case, compared to the frozen case eddy viscosity

## 7.4 Averaging Period Effect

This section presents corrected RANS results for the convective case with a one-hour averaging period and a 5-hour averaging period. Only solutions at stations  $5D$  and  $9D$  downstream of the rotor plane are shown as the errors were largest here. Additionally, the turbulent time scales in the far-wake are greater than in the near-wake.

The wake velocity deficit profiles are shown in fig. 7.24. Not surprisingly, the wall discontinuity persists for the longer averaging period. Additionally, the  $T_{avg} = 5 h$  profiles show similar discrepancies with the reference as the original profiles, the velocity deficit is over-predicted at  $5D$  and mismatches occur on the outside edge of the boundary layer in the span-wise direction.

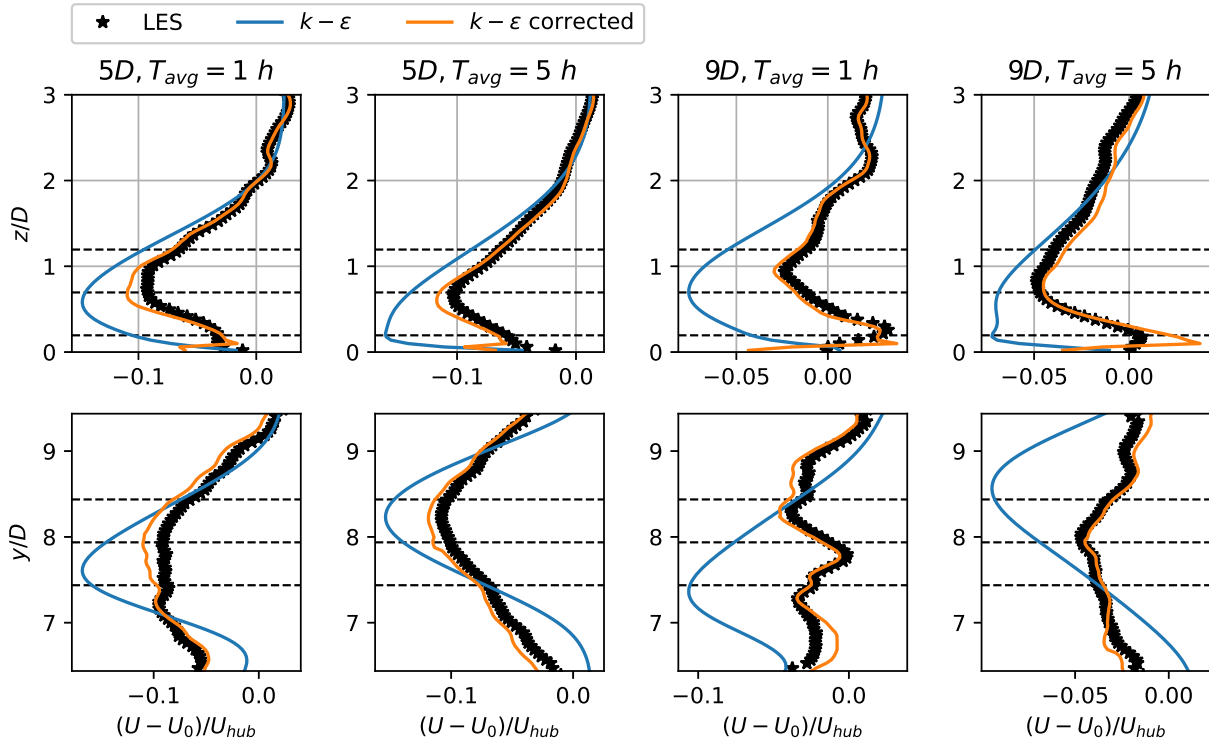


Figure 7.24: Corrected RANS wake velocity deficit profiles for the CBL case using a five-hour averaging period

Figure 7.25 shows the wake kinetic energy profiles. Now, a more drastic difference is observed with the original profiles; the kinetic energy is over-predicted by the corrected RANS model at and right below hub-height. The mismatch at the outer edge of the span-wise plots is also much greater with the larger averaging period.

For the wall-normal turbulent heat flux, shown in fig. 7.26, no difference in pattern is observed between the  $T_{avg} = 1 h$  and  $T_{avg} = 5 h$  profiles. The heat flux is still under-predicted compared to the reference.

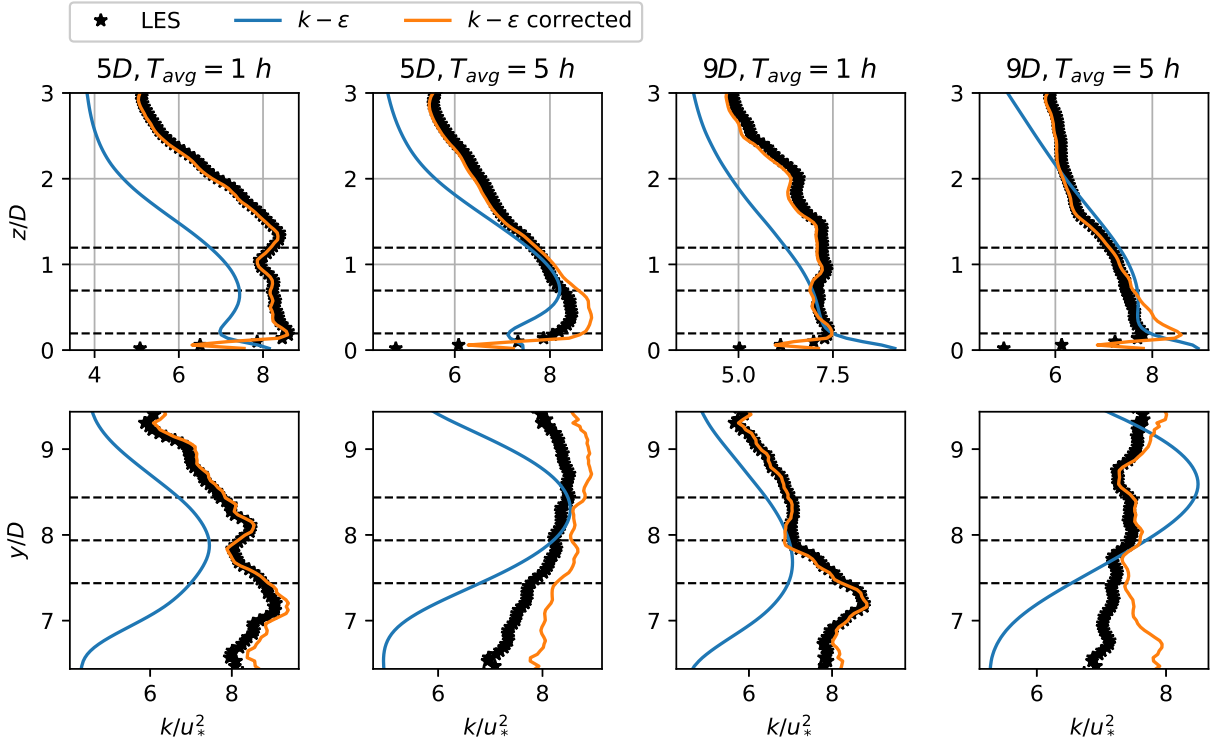


Figure 7.25: Corrected RANS wake turbulent kinetic energy profiles for the CBL case using a five-hour averaging period

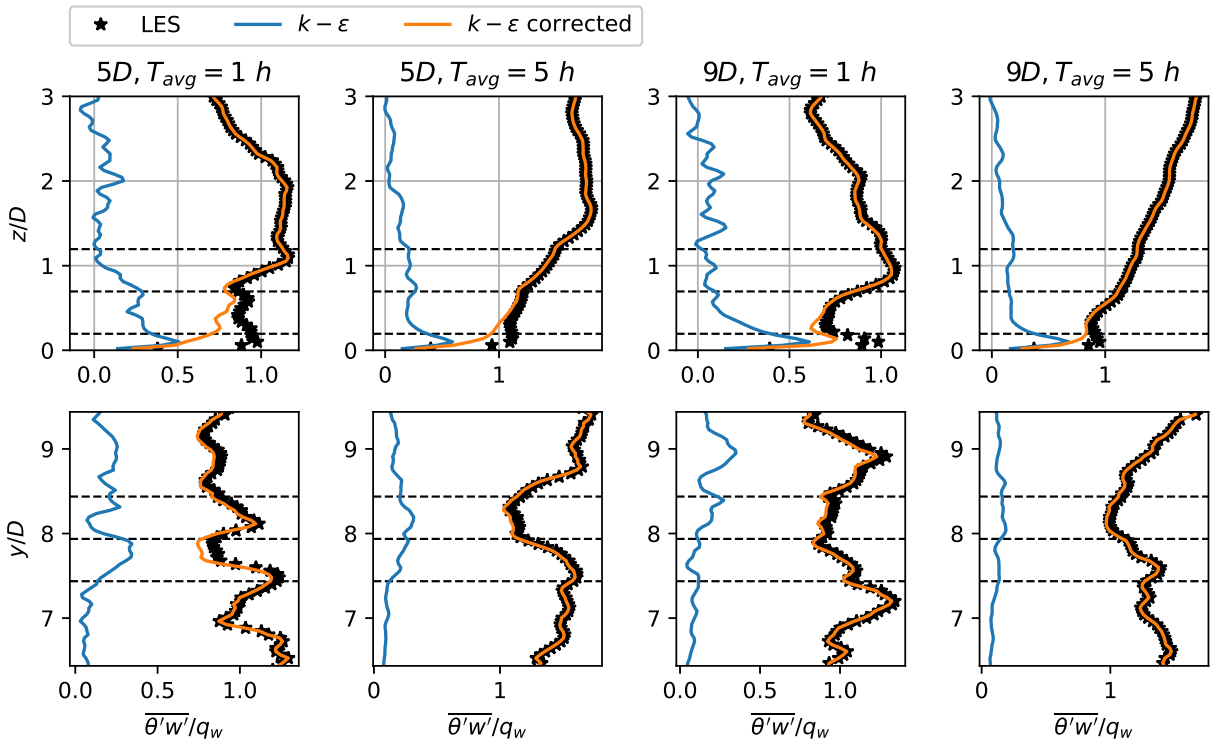


Figure 7.26: Corrected RANS wake wall-normal turbulent heat flux profiles for the CBL case using a five-hour averaging period

## 7.5 Computational Cost

In order to estimate the computational cost of the corrected RANS simulations, RANS convergence is first assessed by plotting the residual history for the neutral case in fig. 7.27. The figure shows the difference between instantly applied corrections, gradually applied corrections over a hundred iterations and the baseline RANS model. The gradual introduction of corrections is achieved by increasing the relaxation term  $\gamma$  in eq. (4.24) from zero to one. Surprisingly, the residual analysis shows that the corrected models' convergence much better than the baseline model, at least for the neutral case. The corrected simulations reach a residual level of  $10^{-3}$  within 250 iterations, while the baseline simulation only does so after 800 iterations. This indicates that the injection of corrections results in a system that is satisfied easier by the governing and model equations. Towards the end of the simulation, the baseline simulation residual convergence rate seems to be closer to corrected cases.

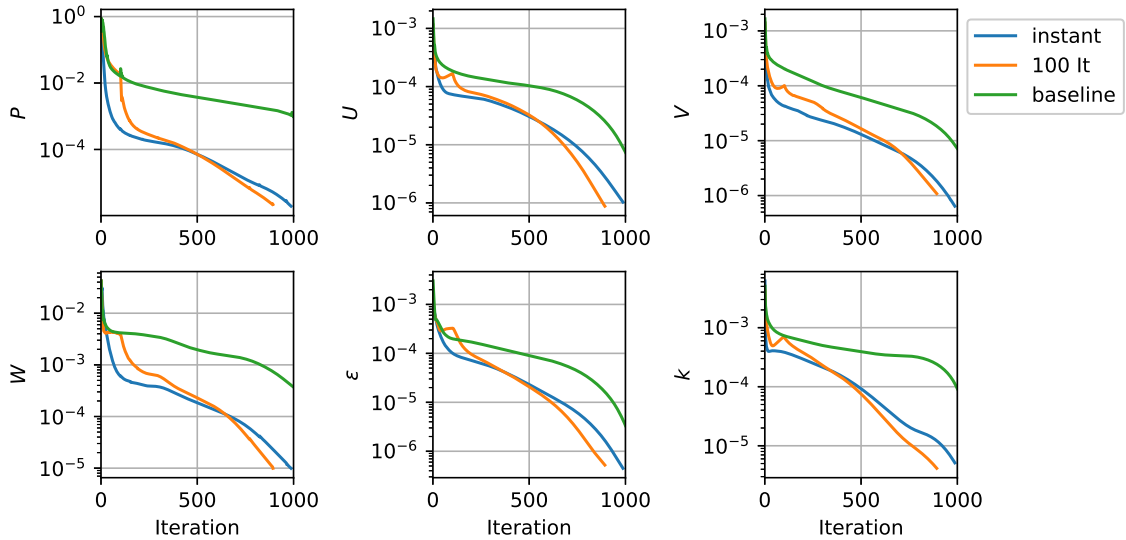


Figure 7.27: NBL case RANS residuals for the corrections applied right from simulation start (instant), gradually over 100 iterations (100 It) and for the baseline  $k - \epsilon$  model (baseline)

The computational cost, measured by the number by core-time (total wall clock-time multiplied with the number of cores), is shown in table 7.1. When considering these results of computational cost, one also needs to take into account the number of cores used to run the simulation. The communication between different cores for computations during parallel processing results in extra overhead that increases the computation cost. As a result, computations run on fewer cores are inherently more efficient although they take longer to run in terms of wall clock-time. The question of parallel processing efficiency and computational cost is incredibly complex and depends not only on the software that is executed but also on the hardware. The results presented in table 7.1 should be interpreted with this in mind.

As expected, the corrected RANS models are able to leverage the computational cost decrease of RANS compared to LES. In terms of computations performed, the extra terms hardly add any work to the models. In fact, the corrected RANS models even show a minor speed-up compared to the baseline RANS models due to quicker convergence. The computational cost of predicting average wake profiles with the new RANS models comes in at only 2 – 5% of the LES cost.

Table 7.1: Computational cost for the various models, measured by wall-clock time and core-time

Model type		NBL	SBL	CBL
LES	Cores	32	100	32
	Wall clock-time [h]	29	12	24
	Core-time [h]	930	1179	767
RANS baseline	Cores	40	80	24
	Wall clock-time [h]	0.91	0.25	1.7
	Core-time [h]	36	20	40
RANS corrected	Cores	40	72	24
	Wall clock-time [h]	0.76	0.28	1.4
	Core-time [h]	31	20	34

## 7.6 Discussion

### SBL velocity mismatch and wall shear stress

In fig. 7.9, a velocity mismatch was observed at the wall in the far wake. The effect could be caused by the following two reasons. Firstly, there might be some discrepancy between the RANS wall stress boundary condition and the LES wall stress boundary condition that is not addressed. The RANS model coefficient  $C_\mu$  is determined from planar and temporal average of  $u_*^{LES}$  and  $k_{wall}^{LES}$ , as described in section 4.2.6. Then, during the RANS simulation, the fixed  $C_\mu$  and the spatially varying  $k_{wall}^{RANS}$  are used to determine the spatially varying  $u_*^{LES}$ , which in turn is used to determine the local RANS wall stress. This local RANS wall stress is not guaranteed to be consistent with the local LES stress, since information was lost in the spatial averaging of  $u_*^{LES}$  and  $k_{wall}^{LES}$ . Perhaps, a solution to the discrepancy would be to assign a spatially varying  $C_\mu$  based on the local LES wall kinetic energy and friction velocity. However, in fig. 7.10 it was observed that the fixed  $C_\mu$  leads to corrected RANS profiles with a perfect kinetic energy match, even at the wall. It might, therefore, be beneficial to keep this fixed  $C_\mu$  formulation for the entire internal field, and only allow it to vary spatially at the lower boundary field. The second possible reason for the discrepancy is the nonphysical velocity boundary condition `velocityABLWallFunction` used in the LES formulation. It was discussed in section 5.1 that the use of this boundary condition is preferred to avoid nonphysical wall SGS stresses. However, the custom boundary condition's change on the velocity profile might affect the frozen-RANS solution and, consequently, the corrected RANS solutions in ways that are not properly understood. In any case, a more formal investigation is required to determine the cause of this issue, especially considering it is not present at all for the neutral case. Besides, fixing the wall stress LES issue, it is crucial to compare the fields of the LES and RANS wall stresses for both the neutral and the stable case.

### Scalar correction to the wall-normal turbulent heat flux

In chapter 6, it was shown that the gradient diffusion hypothesis is an extremely poor model for predicting the direction of the turbulent heat flux. The difference in angle with the LES heat flux was consistently larger than  $70^\circ$  throughout both stratified boundary layers. Additionally, it was shown that the constant turbulent Prandtl number assumption is clearly violated in both cases. This would lead one to believe a full vector correction to the turbulent heat flux is necessary for accurate RANS results. This is true if CFD users are interested in knowing the direction of the heat flux, or if they would like to know the accurate transport of some other passive scalar that is modelled by the gradient diffusion hypothesis. However, in most analyses such as these, knowing the value of wall-parallel turbulent heat fluxes is unnecessary. The stable boundary layer corrected RANS analysis showed that, in this case, using a single scalar correction for only the wall-normal component of the heat flux is perfectly reasonable. The velocity, potential temperature and turbulence quantities were all predicted with equal near-perfect accuracy as when the full vector correction was used.

Only the scalar correction is necessary for the following reasons. For the domain sizes considered, potential temperature transport is almost completely governed by the convective term. Turbulent diffusion term, which is much larger than molecular diffusion, plays a negligible effect on the potential temperature distribution. For both the stable and convective boundary layer wind turbine flow, the baseline  $k - \epsilon$  GDH model predicted the potential temperature distribution equally well as the corrected models and perfectly matched the LES reference. When much larger domain sizes, on the order of tens of kilometers, are considered the turbulent heat flux error might accumulate and lead to a mismatch in potential temperature far downstream of the inflow boundary. Secondly, the stream-wise and span-wise components of the turbulent heat flux correction  $q_j^\Delta$  do not affect the level of buoyant turbulent production, at least if the gravitational vector is aligned with the  $z$  axis. As such, only a correct wall-normal turbulent heat flux affects the turbulent production, which in turn affects the velocity distribution.

### The effect of averaging period

It was shown in section 5.5 that the LES successor profiles in the far-wake of the convective boundary layer got smoother when the length of the averaging window was increased. This shows that a one-hour averaging window is not sufficient in the convective boundary layer. One would expect that this leads to discrepancies when attempting to match corrected RANS profiles to the reference LES. However, it was shown in section 7.4 that using a larger averaging period did not lead to improved solutions for the convective boundary layer corrected RANS profiles. In fact, the solution quality decreased for the turbulent kinetic energy profiles.

This unexpected result might be caused by the changing state of stratified boundary layers over time. When heat is added to the convective boundary layer, the flow state slowly changes over time. This was seen as a slow but steady drift in time-averaged profiles. This effect is not limited to this theoretical work. The actual atmospheric boundary layer is never completely steady. Even when if the geostrophic wind velocity is kept fixed in a theoretical exercise, the diurnal cycle would still result in a constantly changing state. At best, the realistic atmospheric boundary layers are quasi-steady, as is the case for the statistically stationary convective and stable boundary layers studied in the present

thesis. This inherent unsteadiness of the ABL presents a problem for the present RANS and frozen-RANS analysis. Ideally, when comparing RANS against LES, the LES time averages are long so that the obtained profiles are smooth and no longer change when the averaging window is made any greater. However, for such long averaging windows, there is a non-zero bias in the profiles due to the changing state. The effect of this bias is smallest when using a very short time-averaging window.

The present analysis of averaging period on the RANS analysis does not show if there is some kind of satisfactory averaging window duration that produces the best results. It can even be said that the convective boundary layer results were not of high enough quality in any case, convolution the results. It would therefore be interesting to perform a similar analysis for the stable boundary layer. Due to limitations in time, this was no longer possible in this thesis.

Another solution to the problem of averaging period for stratified ABL LES might be to compute the total energy added to the domain at the lower boundary and subtract it evenly from the entire domain at every time step. This would mean it would be possible for the stratified boundary layer to reach a true steady-state enabling longer averaging periods. It is unsure, however, whether the specific flow features, such as the capping inversion and the low-level jet, would remain a part of the steady-state solution.

# Conclusions and Recommendation

The main objective of this thesis was to contribute to data-driven turbulence model developments, and the understanding of turbulence, for wind turbine wake flows. The contributions of the work lie in several factors. Firstly, high fidelity LES reference data was generated and archived so that it may benefit other's research as well. Secondly, the effects of non-neutral atmospheric conditions as well as Coriolis force are considered. Finally, the frozen-RANS analysis is done for a representative industrial-scale wind turbine flow.

After the generation of LES reference data, the frozen-RANS framework was extended to include model-form error of the turbulent heat flux and its impact on other turbulence quantities. The model-form errors were then injected, as corrections, into RANS simulations and compared against the LES data and the baseline model. The results were analysed and discussed, with a focus on discrepancies between simulations and possible strategies to overcome these. Based on these analyses, conclusions are drawn in section 8.1 and recommendations for future work are given in section 8.2.

## 8.1 Conclusions

**RQ1: What are the model-form errors of the  $k - \epsilon$  and GDH model in stable and unstable wind turbine flows, and how do they differ from neutral wind turbine flows?**

Visualizing the model-form correction of the normalized anisotropy tensor shows that anisotropy in the atmospheric boundary layer is not reproduced by the baseline model. Only the  $xz$  and  $yz$  components have a non-zero strain rate. As such, these are the only components for which the baseline model produces a non-zero value. For the neutral free-stream ABL, the baseline model predicts these components reasonably well. But for the stratified cases, the predictions for these components show large discrepancies with LES, resulting in high values of the anisotropy correction for all components. For the neutral and stable boundary layer, the effect of the anisotropy on the shear production is turbulence is a correction for an overproduction at the wall by the baseline  $k - \epsilon$  model equations. For the convective case, the anisotropy results in a correction for an under-production of shear turbulence at the wall. Additionally, the over-production of shear turbulence in the strong capping inversion is corrected for. When considering the wind turbine, the anisotropy corrects for an over-production of turbulence in the near wake for all stability cases.

The residual to the  $k$  transport equations seems to be the most dependant on atmospheric stability. For the free-stream, the correction adds to the transport equation at the wall, while it is negative for the convective case in the entire boundary layer depth. For the turbine wake in the stable case, the residual shows a very clear structure as it has large positive values at the upper edge of the far wake and low negative values at the rotor plane. For the neutral boundary layer wake, the residual moderate noise levels while the signal is completely dominated by large values of noise for the convective case. Numerical instabilities in the large-eddy simulation are the likely cause for this noise.

The turbulent heat flux correction, and the angle between the modelled and the reference heat flux, show that the gradient-diffusion hypothesis completely fails to produce accurate heat flux direction and magnitude. For the stable case, the correction accounts for a negative wall-normal heat flux that is too large in magnitude in the free-stream boundary layer, resulting in too much buoyant destruction by the baseline model. In the wake, the heat flux correction corrects for too little buoyant destruction. For the convective case, the heat flux correction corrects for too little buoyant production in the boundary layer and in the wind turbine wake but corrects for an extreme over-destruction of turbulence in the capping inversion.

**RQ2: What are the considerations injecting the model-form corrections into the RANS equations during simulation?**

There are a few considerations when injecting the static frozen-RANS corrections to dynamic RANS solvers. Firstly, the corrections can be applied to various parts of the simulation domain by multiplying them with a blending term  $F$  before injecting. In both the present RANS simulations and those done in Steiner, Dwight, and Viré [5], it was found that using the blending function to turn off the corrections at the upper wall is necessary for the correct RANS simulations to converge. Generally speaking, the model-form corrections should be applied throughout the rest of the domain, so until and including the first wall-normal cell. In the present convective boundary layer LES, the use of the one equation Deardoff model with this SOWFA-6 setup produces an erroneous SGS stress tensor and kinetic energy at the lower wall. Excluding the anisotropy correction from this near-wall region improved the corrected RANS results for the free-stream case compared to fully including all corrections, demonstrating another use for the blending function. It is always preferred, though, to use reference data that is of the best possible quality, particularly at the lower wall, since this region is hard but important to model.

Before injecting them into the RANS system, the corrections are also multiplied with the relaxation term so that they can be gradually introduced. Neutral case results indicate that gradual injection results in slightly faster convergence than immediate full injection.

**RQ3: What is the accuracy and the computational demand of the corrected RANS models compared to the baseline RANS model and the LES model?**

For the free-stream flow, the baseline models provide satisfactory velocity and potential temperature predictions for all stability cases. The stream-wise lengths of the domains are not long enough for the error in the baseline turbulence to accumulate and effect the solution. The effect of the corrections become noticeable when observing the secondary statistics; the turbulent kinetic energy, Reynolds stress, and the turbulent heat flux. In all cases the baseline models show an under-prediction of ambient turbulence. For the neutral and stable cases, the corrected RANS turbulence kinetic energy and Reynolds stress accuracy are close to perfect. The corrected RANS heat flux for the stable free-stream boundary layer also shows near perfect agreement. For the convective case, the corrected RANS profiles improve significantly but show some wall wall discrepancies. The issue is improved slightly by excluding the anisotropy correction below a certain height close to the wall. In general, the corrected RANS models provide accurate solutions for the complex flow features not typically handled well in RANS; the low level jet in the stable atmosphere and the capping inversion in the convective atmosphere.

With the inclusion of the wind turbine, the flow complexity increases significantly. The baseline model velocity predictions in the wake show large discrepancies with the reference data. For the neutral case, the near-wake wake velocity discrepancy is largest while the opposite is true for both stratified boundary layers. For the neutral case, the injection of the model-form corrections completely fix the well documented  $k - \epsilon$  limitation of an overproduction of kinetic energy in the near wake, resulting in near perfect velocity and turbulent statistics.

For the stable case, the corrected RANS results also show impressive accuracy. In every statistic, the match is excellent, with the exception of a slightly lower wall velocity in the far-wake. It was discussed that the most likely reasons are an inconsistency between the RANS and LES wall stress formulations and the possibly non-physical LES velocity boundary condition.

For the unstable case, the velocity and TKE prediction accuracy is extremely poor at the lower wall, particularly in the far-wake. The most likely reason for this is the nonphysical wall SGS stresses observed in the LES. When the anisotropy correction is excluded in the near wall region, the quantities tend to the values produced the baseline RANS simulations. Since these did not match the reference either, the prediction quality at the wall is not improved with this strategy. Away from the wall, above the lower tip of the wind turbine, the corrected RANS velocity and TKE do agree better with the LES reference, showing that there is indeed merit to the approach if high-quality reference data is used. The corrected RANS heat flux profiles on the other hand show good agreement with the reference. Since the heat flux affects the turbulence production, and the TKE affects the velocity, the heat flux correction contributes considerably to the improvements observed in the velocity profiles away from the wall.

**RQ4: How does the computational cost of the corrected RANS model compare to the baseline and LES models?**

For all stability cases, the computational cost of the corrected RANS models is shown to be slightly lower

than that of the baseline model. It is computationally inexpensive to introduce a static field into the model equations. Additionally, the addition of the corrections seems to result in a system which better satisfies the governing and model equations, resulting in quicker convergence. The computational cost of the corrected RANS model presents only 2%-5% of the cost of the LES model. When the model-form corrections are regressed in terms of flow-features known in RANS, the computational cost would go up slightly depending on the complexity of the regression model. Still, it is expected that the methodology would remain cost-competitive with standard RANS models.

#### **RQ5: How is the frozen-RANS framework best extended to stable and convective atmospheric conditions?**

When attempting to correct the GDH model for the turbulent heat flux, one can either correct the wall-normal heat flux, or the entire vector. The former option, which could be enforced as a variable turbulent Prandtl, presents a much more simple solution. The latter option, on the other hand, is much more general. A full vector correction would improve both the error in the heat flux magnitude and direction, both of which were shown to be extreme in the stratified boundary layers. However, it was shown that, if the user is not interested in the direction of the flux or the wall-parallel components, the scalar correction to the wall-normal heat flux is sufficient. Over the stream-wise domain lengths considered, the wall-parallel components do not at all improve the modelled quantities. Instead, only the wall-normal heat flux component drives the buoyant production of turbulence. In the stable boundary layer results, it was shown that only injecting the wall-normal heat flux correction results in predictions equally accurate as the predictions obtained with the full vector heat flux correction, at least for the velocity, temperature and turbulence quantities. The implications of a scalar correction to the wall-normal heat flux being sufficient for most cases are considerable. Not only is simplicity generally favourable, but regressing a model for a scalar correction would constitute a much easier modelling challenge than regressing the full vector correction. The result is only true for flat-terrain wind turbine flows in domains that are not too long.

Returning the main objective to contribute to the understanding of turbulence in non-neutral wind turbine flows, the analyses in this thesis have shown that the gradient-diffusion hypothesis for the turbulent heat flux is violated, and that some kind of heat flux correction is necessary for non-neutral atmospheric conditions. However, a scalar correction such as a variable turbulent Prandtl number model is shown to be sufficient for accurate wake velocity and turbulence predictions. The work has shown that the current frozen-RANS framework can be successfully applied to non-neutral atmospheres and to industrial scale wind turbines. Provided that high quality reference data is available, LES quality solutions can be obtained a computational cost of that is two orders of magnitude lower.

## **8.2 Recommendations**

The first and most important recommendation in future work is to produce reference LES data that is of higher quality. In the current setup, use of the velocity boundary condition `velocityABLWallFunction` is necessary to avoid high SGS stresses at the wall. This comes at the cost of a slightly lower, non-physical, wall velocity which does not agree with the log-law. In the unstable case, the condition could not be used, and the no slip condition had to be used instead, resulting in non-physically high wall stresses. Preferably, wall damping functions are applied to limit the SGS viscosity so that the no slip condition can be used, as is customary for wall-modelled LES. Alternatively, an SGS model with a dynamic procedure could also be used.

Furthermore, high degrees of roughness and structure in time averaged wake profiles show that the convective LES case has not been averaged for long enough. The averaging period of 1  $h$  or roughly five flow-throughs was increased to 5  $h$  but the results, although smoothed, did not improve for the corrected RANS analyses. A more thorough investigation is required into the possibility of modelling the inherently unsteady atmospheric boundary layer with steady-state techniques like RANS.

As concluded, only a scalar turbulent heat flux correction is required for the accurate modelling of the non-neutral boundary layer under the condition that the terrain is flat and the stream-wise length of the domain is not too long. What constitutes as too long remains an open question, and it is not a trivial one since off-shore wind farms are getting larger and larger. It is recommended that future work is dedicated to quantifying a limit for when the scalar correction is sufficient.

Splitting up the applied corrections into a free-stream term and turbine specific term can be useful for turning off either one of the two locally. Furthermore, it is useful when applying machine learning algorithms to learn improved models. It is more appropriate to have a separate model for only the free-stream and a separate model for only turbines corrections. This would also help in getting physical insight from the models, as it is easier to interpret model terms that are only derived for one specific purpose.

# Bibliography

- [1] A. Nghiem and I. Pineda, "Wind energy in europe: Scenarios for 2030," WindEurope, Tech. Rep., 2017. [Online]. Available: <https://windeurope.org/data-and-analysis/product/wind-energy-in-europe-scenarios-for-2030/>.
- [2] G. Svensson, A. A. M. Holtslag, V. Kumar, T. Mauritsen, G. J. Steeneveld, W. M. Angevine, E. Bazile, A. Beljaars, E. I. F. De Bruijn, A. Cheng, *et al.*, "Evaluation of the diurnal cycle in the atmospheric boundary layer over land as represented by a variety of single-column models: The second gabl's experiment," *Boundary-Layer Meteorology*, vol. 140, no. 2, pp. 177–206, 2011.
- [3] K. S. Hansen, R. J. Barthelmie, L. E. Jensen, and A. Sommer, "The impact of turbulence intensity and atmospheric stability on power deficits due to wind turbine wakes at horns rev wind farm," *Wind Energy*, vol. 15, no. 1, pp. 183–196, 2012. DOI: <https://doi.org/10.1002/we.512>. eprint: <https://onlinelibrary.wiley.com/doi/pdf/10.1002/we.512>. [Online]. Available: <https://onlinelibrary.wiley.com/doi/abs/10.1002/we.512>.
- [4] R. J. Barthelmie and L. E. Jensen, "Evaluation of wind farm efficiency and wind turbine wakes at the nysted offshore wind farm," *Wind Energy*, vol. 13, no. 6, pp. 573–586, 2010. DOI: <https://doi.org/10.1002/we.408>. eprint: <https://onlinelibrary.wiley.com/doi/pdf/10.1002/we.408>. [Online]. Available: <https://onlinelibrary.wiley.com/doi/abs/10.1002/we.408>.
- [5] J. Steiner, R. P. Dwight, and A. Viré, "Data-driven turbulence modeling for wind turbine wakes under neutral conditions," 2020, Submitted for publication.
- [6] D. C. Wilcox, *Turbulence Modelling for CFD (Third Edition)*. 2006.
- [7] S. B. Pope, *Turbulent Flows*. Cambridge University Press, 2000. DOI: 10.1017/CB09780511840531.
- [8] B. Sanderse, S. P. van der Pijl, and B. Koren, "Review of computational fluid dynamics for wind turbine wake aerodynamics," *Wind Energy*, vol. 14, no. 7, pp. 799–819, 2011. DOI: <https://doi.org/10.1002/we.458>. eprint: <https://onlinelibrary.wiley.com/doi/pdf/10.1002/we.458>. [Online]. Available: <https://onlinelibrary.wiley.com/doi/abs/10.1002/we.458>.
- [9] M. P. van der Laan, N. N. Sørensen, P.-E. M. Réthoré, J. Mann, M. C. Kelly, N. Troldborg, J. G. Schepers, and E. Machefaux, "An improved k- $\epsilon$  model applied to a wind turbine wake in atmospheric turbulence," *Wind Energy*, vol. 18, no. 5, pp. 889–907, 2015. DOI: <https://doi.org/10.1002/we.1736>. eprint: <https://onlinelibrary.wiley.com/doi/pdf/10.1002/we.1736>. [Online]. Available: <https://onlinelibrary.wiley.com/doi/abs/10.1002/we.1736>.
- [10] J. Ling, A. Kurzwski, and J. Templeton, "Reynolds averaged turbulence modelling using deep neural networks with embedded invariance," *Journal of Fluid Mechanics*, vol. 807, pp. 155–166, 2016.
- [11] J. Weatheritt and R. D. Sandberg, "A novel evolutionary algorithm applied to algebraic modifications of the rans stress-strain relationship," *Journal of Computational Physics*, vol. 325, pp. 22–37, 2016, ISSN: 0021-9991. DOI: <https://doi.org/10.1016/j.jcp.2016.08.015>. [Online]. Available: <http://www.sciencedirect.com/science/article/pii/S0021999116303643>.
- [12] J. Weatheritt and R. D. Sandberg, "The development of algebraic stress models using a novel evolutionary algorithm," *International Journal of Heat and Fluid Flow*, vol. 68, pp. 298–318, 2017, ISSN: 0142-727X. DOI: <https://doi.org/10.1016/j.ijheatfluidflow.2017.09.017>. [Online]. Available: <http://www.sciencedirect.com/science/article/pii/S0142727X17303223>.
- [13] M. Schmelzer, R. P. Dwight, and P. Cinnella, "Discovery of algebraic reynolds-stress models using sparse symbolic regression," *Flow, Turbulence and Combustion*, no. 104, pp. 579–603, 2020, <https://doi.org/10.1007/s10494-019-00089-x>.

- [14] K. Duraisamy, G. Iaccarino, and H. Xiao, "Turbulence modeling in the age of data," *Annual Review of Fluid Mechanics*, vol. 51, no. 1, pp. 357–377, 2019. DOI: 10.1146/annurev-fluid-010518-040547. eprint: <https://doi.org/10.1146/annurev-fluid-010518-040547>. [Online]. Available: <https://doi.org/10.1146/annurev-fluid-010518-040547>.
- [15] J. Weatheritt, Y. Zhao, R. D. Sandberg, S. Mizukami, and K. Tanimoto, "Data-driven scalar-flux model development with application to jet in cross flow," *International Journal of Heat and Mass Transfer*, vol. 147, p. 118931, 2020, ISSN: 0017-9310. DOI: [url{https://doi.org/10.1016/j.ijheatmasstransfer.2019.118931}](https://doi.org/10.1016/j.ijheatmasstransfer.2019.118931). [Online]. Available: [%5Curl%7Bhttp://www.sciencedirect.com/science/article/pii/S0017931019329187%7D](https://www.sciencedirect.com/science/article/pii/S0017931019329187).
- [16] P. M. Milani, J. Ling, and J. K. Eaton, "Turbulent scalar flux in inclined jets in crossflow: Counter gradient transport and deep learning modelling," *arXiv preprint arXiv:2001.04600*, 2020.
- [17] E. Machefaux, G. C. Larsen, T. Koblitz, N. Troldborg, M. C. Kelly, A. Chougule, K. S. Hansen, and J. S. Rodrigo, "An experimental and numerical study of the atmospheric stability impact on wind turbine wakes," *Wind Energy*, vol. 19, no. 10, pp. 1785–1805, 2016. DOI: <https://doi.org/10.1002/we.1950>. eprint: <https://onlinelibrary.wiley.com/doi/pdf/10.1002/we.1950>. [Online]. Available: <https://onlinelibrary.wiley.com/doi/abs/10.1002/we.1950>.
- [18] Xie S. and C. L. Archer, "A numerical study of wind-turbine wakes for three atmospheric stability conditions," *Boundary-Layer Meteorol*, no. 165, pp. 87–112, 2017, DOI 10.1007/s10546-017-0259-9.
- [19] N. S. Ghaisas, C. L. Archer, Xie Shengbai, Wu Sicheng, and E. Maguire, "Evaluation of layout and atmospheric stability effects in wind farms using large-eddy simulation," *Wind Energy*, vol. 20, no. 7, pp. 1227–1240, 2017.
- [20] R. Stull, *Practical Meteorology: An Algebra-based Survey of Atmospheric Science*. University of British Columbia, 2017.
- [21] A. Peña, S.-E. Gryning, and J. Mann, "On the length-scale of the wind profile," *Quarterly Journal of the Royal Meteorological Society*, vol. 136, no. 653, pp. 2119–2131, 2010.
- [22] J. P. Pandolfo, "Wind and temperature profiles for constant-flux boundary layers in lapse conditions with a variable eddy conductivity to eddy viscosity ratio," *Journal of the Atmospheric Sciences*, vol. 23, no. 5, pp. 495–502, 1966.
- [23] M. P. van der Laan, M. C. Kelly, and N. N. Sørensen, "A new k-epsilon model consistent with monin-obukhov similarity theory," *Wind Energy*, vol. 20, no. 3, pp. 479–489, 2017. DOI: <https://doi.org/10.1002/we.2017>. eprint: <https://onlinelibrary.wiley.com/doi/pdf/10.1002/we.2017>. [Online]. Available: <https://onlinelibrary.wiley.com/doi/abs/10.1002/we.2017>.
- [24] A. J. Dyer, "A review of flux-profile relationships," *Boundary-Layer Meteorology*, vol. 7, no. 3, pp. 363–372, 1974.
- [25] J. A. Businger, J. C. Wyngaard, Y. Izumi, and E. F. Bradley, "Flux-profile relationships in the atmospheric surface layer," *Journal of the atmospheric Sciences*, vol. 28, no. 2, pp. 181–189, 1971.
- [26] F. Porté-Agel, Y.-T. Wu, H. Lu, and R. J. Conzemius, "Large-eddy simulation of atmospheric boundary layer flow through wind turbines and wind farms," *Journal of Wind Engineering and Industrial Aerodynamics*, vol. 99, no. 4, pp. 154–168, 2011, The Fifth International Symposium on Computational Wind Engineering, ISSN: 0167-6105. DOI: <https://doi.org/10.1016/j.jweia.2011.01.011>. [Online]. Available: <http://www.sciencedirect.com/science/article/pii/S0167610511000134>.
- [27] A. Crespo, J. Hernandez, and S. Frandsen, "Survey of modelling methods for wind turbine wakes and wind farms," *Wind Energy: An International Journal for Progress and Applications in Wind Power Conversion Technology*, vol. 2, no. 1, pp. 1–24, 1999.
- [28] F. Porté-Agel, M. Bastankhah, and S. Shamsoddin, "Wind-turbine and wind-farm flows: A review," *Boundary-Layer Meteorology*, vol. 174, no. 1, pp. 1–59, 2020.
- [29] L. P. Chamorro and F. Porté-Agel, "A wind-tunnel investigation of wind-turbine wakes: Boundary-layer turbulence effects," *Boundary-layer meteorology*, vol. 132, no. 1, pp. 129–149, 2009.
- [30] M. Magnusson and A.-S. Smedman, "Influence of atmospheric stability on wind turbine wakes," *Wind Engineering*, pp. 139–152, 1994.
- [31] R. W. Baker and S. N. Walker, "Wake measurements behind a large horizontal axis wind turbine generator," *Solar Energy*, vol. 33, no. 1, pp. 5–12, 1984.
- [32] J. Smagorinsky, "General circulation experiments with the primitive equations: I. the basic experiment," *Monthly Weather Review*, vol. 91, no. 3, pp. 99–164, 1Mar. 1963. DOI: 10.1175/1520-0493(1963)091<0099:GCEWTP>2.3.CO;2. [Online]. Available: [https://journals.ametsoc.org/view/journals/mwre/91/3/1520-0493\\_1963\\_091\\_0099\\_gcewtp\\_2\\_3\\_co\\_2.xml](https://journals.ametsoc.org/view/journals/mwre/91/3/1520-0493_1963_091_0099_gcewtp_2_3_co_2.xml).

- [33] M. Germano, U. Piomelli, P. Moin, and W. H. Cabot, "A dynamic subgrid-scale eddy viscosity model," *Physics of Fluids A: Fluid Dynamics*, vol. 3, no. 7, pp. 1760–1765, 1991.
- [34] F. Nicoud and F. Ducros, "Subgrid-scale stress modelling based on the square of the velocity gradient tensor," *Flow, turbulence and Combustion*, vol. 62, no. 3, pp. 183–200, 1999.
- [35] H. Sarlak, "Large eddy simulation of turbulent flows in wind energy," *PhD thesis Technical University of Denmark*, 2014.
- [36] J. Boussinesq, "Essai sur la théorie des eaux courantes," *Impr. nationale (Paris)*, 1877.
- [37] F. G. Schmitt, "About boussinesq's turbulent viscosity hypothesis: Historical remarks and a direct evaluation of its validity," *Comptes Rendus Mécanique*, vol. 335, no. 9, pp. 617–627, 2007, Joseph Boussinesq, a Scientist of bygone days and present times, ISSN: 1631-0721. DOI: <https://doi.org/10.1016/j.crme.2007.08.004>. [Online]. Available: <http://www.sciencedirect.com/science/article/pii/S1631072107001386>.
- [38] B. E. Launder and D. B. Spalding, "The numerical computation of turbulent flows," *Computer Methods in Applied Mechanics and Engineering*, vol. 3, no. 2, pp. 269–289, 1974, ISSN: 0045-7825. DOI: [https://doi.org/10.1016/0045-7825\(74\)90029-2](https://doi.org/10.1016/0045-7825(74)90029-2). [Online]. Available: <http://www.sciencedirect.com/science/article/pii/0045782574900292>.
- [39] A. El Kasmi and C. Masson, "An extended  $k-\epsilon$  model for turbulent flow through horizontal-axis wind turbines," *Journal of Wind Engineering and Industrial Aerodynamics*, vol. 96, no. 1, pp. 103–122, 2008, ISSN: 0167-6105. DOI: <https://doi.org/10.1016/j.jweia.2007.03.007>. [Online]. Available: <http://www.sciencedirect.com/science/article/pii/S0167610507000943>.
- [40] P.-E. M. Réthoré, "Wind turbine wake in atmospheric turbulence," English, Ph.D. dissertation, Oct. 2009, ISBN: 978-87-550-3785-4.
- [41] J. M. Prospathopoulos, E. S. Politis, K. G. Rados, and P. K. Chaviaropoulos, "Evaluation of the effects of turbulence model enhancements on wind turbine wake predictions," *Wind Energy*, vol. 14, no. 2, pp. 285–300, DOI: <https://doi.org/10.1002/we.419>. eprint: <https://www.onlinelibrary.wiley.com/doi/pdf/10.1002/we.419>. [Online]. Available: <https://www.onlinelibrary.wiley.com/doi/abs/10.1002/we.419>.
- [42] D. Cabezón, E. Migoya, and A. Crespo, "Comparison of turbulence models for the computational fluid dynamics simulation of wind turbine wakes in the atmospheric boundary layer," *Wind Energy*, vol. 14, no. 7, pp. 909–921, 2011. DOI: <https://doi.org/10.1002/we.516>. eprint: <https://onlinelibrary.wiley.com/doi/pdf/10.1002/we.516>. [Online]. Available: <https://onlinelibrary.wiley.com/doi/abs/10.1002/we.516>.
- [43] P. A. Durbin, "On the  $k-3$  stagnation point anomaly," *International Journal of Heat and Fluid Flow*, vol. 17, no. 1, pp. 89–90, 1996, ISSN: 0142-727X. DOI: [https://doi.org/10.1016/0142-727X\(95\)00073-Y](https://doi.org/10.1016/0142-727X(95)00073-Y). [Online]. Available: <http://www.sciencedirect.com/science/article/pii/0142727X9500073Y>.
- [44] D. D. Apsley and M. A. Leschziner, "A new low-reynolds-number nonlinear two-equation turbulence model for complex flows," *International Journal of Heat and Fluid Flow*, vol. 19, no. 3, pp. 209–222, 1998, ISSN: 0142-727X. DOI: [https://doi.org/10.1016/S0142-727X\(97\)10007-8](https://doi.org/10.1016/S0142-727X(97)10007-8). [Online]. Available: <http://www.sciencedirect.com/science/article/pii/S0142727X97100078>.
- [45] M. P. van der Laan and S. J. Andersen, "The turbulence scales of a wind turbine wake: A revisit of extended  $k$ -epsilon models," *Journal of Physics: Conference Series*, vol. 1037, p. 072001, Jun. 2018. DOI: 10.1088/1742-6596/1037/7/072001. [Online]. Available: <https://doi.org/10.1088/1742-6596/1037/7/072001>.
- [46] T.-H. Shih, W. W. Liou, A. Shabbir, Z. Yang, and J. Zhu, "A new  $k-\epsilon$  eddy viscosity model for high reynolds number turbulent flows," *Computers & fluids*, vol. 24, no. 3, pp. 227–238, 1995.
- [47] M. P. van der Laan, N. N. Sørensen, P.-E. Réthoré, J. Mann, M. C. Kelly, N. Troldborg, K. S. Hansen, and J. P. Murcia, "The  $k-\epsilon$ -fp model applied to wind farms," *Wind Energy*, vol. 18, no. 12, pp. 2065–2084, 2015. DOI: <https://doi.org/10.1002/we.1804>. eprint: <https://onlinelibrary.wiley.com/doi/pdf/10.1002/we.1804>. [Online]. Available: <https://onlinelibrary.wiley.com/doi/abs/10.1002/we.1804>.
- [48] F. Menter, "Zonal two equation  $k-w$  turbulence models for aerodynamic flows," in *23rd Fluid Dynamics, Plasmadynamics, and Lasers Conference*. DOI: 10.2514/6.1993-2906. eprint: <https://arc.aiaa.org/doi/pdf/10.2514/6.1993-2906>. [Online]. Available: <https://arc.aiaa.org/doi/abs/10.2514/6.1993-2906>.
- [49] "Models with scalar variables," in *Statistical Theory and Modeling for Turbulent Flows*. John Wiley & Sons, Ltd, 2010, ch. 6, pp. 109–154, ISBN: 9780470972076. DOI: <https://doi.org/10.1002/9780470972076.ch6>. eprint: <https://onlinelibrary.wiley.com/doi/pdf/10.1002/9780470972076.ch6>. [Online]. Available: <https://onlinelibrary.wiley.com/doi/abs/10.1002/9780470972076.ch6>.

- [50] E. G. A. Antonini, D. A. Romero, and C. H. Amon, "Analysis and Modifications of Turbulence Models for Wind Turbine Wake Simulations in Atmospheric Boundary Layers," *Journal of Solar Energy Engineering*, vol. 140, no. 3, Mar. 2018, 031007, ISSN: 0199-6231. DOI: 10.1115/1.4039377. eprint: <https://asmedigitalcollection.asme.org/solarenergyengineering/article-pdf/140/3/031007/6330434/sol\140\03\031007.pdf>. [Online]. Available: <https://doi.org/10.1115/1.4039377>.
- [51] —, "Improving cfd wind farm simulations incorporating wind direction uncertainty," *Renewable Energy*, vol. 133, pp. 1011–1023, 2019, ISSN: 0960-1481. DOI: <https://doi.org/10.1016/j.renene.2018.10.084>. [Online]. Available: <http://www.sciencedirect.com/science/article/pii/S0960148118312801>.
- [52] M. Shives and C. Crawford, "Adapted two-equation turbulence closures for actuator disk rans simulations of wind & tidal turbine wakes," *Renewable Energy*, vol. 92, pp. 273–292, 2016, ISSN: 0960-1481. DOI: <https://doi.org/10.1016/j.renene.2016.02.026>. [Online]. Available: <http://www.sciencedirect.com/science/article/pii/S0960148116301276>.
- [53] A. Hellsten and S. Wallin, "Explicit algebraic reynolds stress and non-linear eddy-viscosity models," *International Journal of Computational Fluid Dynamics*, vol. 23, no. 4, pp. 349–361, 2009. DOI: 10.1080/10618560902776828. eprint: <https://doi.org/10.1080/10618560902776828>. [Online]. Available: <https://doi.org/10.1080/10618560902776828>.
- [54] S. B. Pope, "A more general effective-viscosity hypothesis," *Journal of Fluid Mechanics*, vol. 72, no. 2, pp. 331–340, 1975. DOI: 10.1017/S0022112075003382.
- [55] M. P. van der Laan, N. N. Sørensen, P.-E. Réthoré, J. Mann, M. C. Kelly, and J. G. Schepers, "Nonlinear eddy viscosity models applied to wind turbine wakes," English, in *Proceedings of the 2013 International Conference on aerodynamics of Offshore Wind Energy Systems and wakes (ICOWES2013)*, International Conference on aerodynamics of Offshore Wind Energy Systems and wakes (ICOWES 2013), ICOWES ; Conference date: 17-06-2013 Through 19-06-2013, Technical University of Denmark, 2013, pp. 514–525.
- [56] D. B. Taulbee, "An improved algebraic reynolds stress model and corresponding nonlinear stress model," *Physics of Fluids A: Fluid Dynamics*, vol. 4, no. 11, pp. 2555–2561, 1992. DOI: 10.1063/1.858442. eprint: <https://doi.org/10.1063/1.858442>. [Online]. Available: <https://doi.org/10.1063/1.858442>.
- [57] A. Jimenez, A. Crespo, E. Migoya, and J. Garcia, "Advances in large-eddy simulation of a wind turbine wake," *Journal of Physics: Conference Series*, vol. 75, pp. 12–41, 2007, ISSN: 1742-6596. DOI: 10.1088/1742-6596/75/1/012041. [Online]. Available: <https://iopscience.iop.org/article/10.1088/1742-6596/75/1/012041>.
- [58] B. J. Daly and F. H. Harlow, "Transport equations in turbulence," *The Physics of Fluids*, vol. 13, no. 11, pp. 2634–2649, 1970.
- [59] K. Abe and K. Suga, "Towards the development of a reynolds-averaged algebraic turbulent scalar-flux model," *International Journal of Heat and Fluid Flow*, vol. 22, no. 1, pp. 19–29, 2001.
- [60] J. Ling, K. J. Ryan, J. Bodart, and J. K. Eaton, "Analysis of turbulent scalar flux models for a discrete hole film cooling flow," *Journal of Turbomachinery*, vol. 138, no. 1, 2016.
- [61] C. Alinot and C. Masson, "k- $\epsilon$  Model for the Atmospheric Boundary Layer Under Various Thermal Stratifications," *Journal of Solar Energy Engineering*, vol. 127, no. 4, pp. 438–443, Jun. 2005, ISSN: 0199-6231. DOI: 10.1115/1.2035704. eprint: <https://asmedigitalcollection.asme.org/solarenergyengineering/article-pdf/127/4/438/5728008/438\1.pdf>. [Online]. Available: <https://doi.org/10.1115/1.2035704>.
- [62] X. Han, D. Liu, C. Xu, W. Shen, L. Li, and F. Xue, "Monin-obukhov similarity theory for modeling of wind turbine wakes under atmospheric stable conditions: Breakdown and modifications," *Applied Sciences (Switzerland)*, vol. 9, no. 20, 2019, cited By 0. DOI: 10.3390/app9204256. [Online]. Available: <https://www.scopus.com/inward/record.uri?eid=2-s2.0-85074147973&doi=10.3390%5C%2Fapp9204256&partnerID=40&md5=83130eab237945ef1a61595cc9141e79>.
- [63] W. A. El-Askary, I. M. Sakr, A. M. AbdelSalam, and M. R. Abuhegazy, "Modeling of wind turbine wakes under thermally-stratified atmospheric boundary layer," *Journal of Wind Engineering and Industrial Aerodynamics*, vol. 160, pp. 1–15, 2017, ISSN: 0167-6105. DOI: <https://doi.org/10.1016/j.jweia.2016.11.001>. [Online]. Available: <http://www.sciencedirect.com/science/article/pii/S0167610516302409>.
- [64] L. Martínez Tossas, S. Leonardi, M. Churchfield, and P. Moriarty, "A comparison of actuator disk and actuator line wind turbine models and best practices for their use," Jan. 2012, ISBN: 978-1-60086-936-5. DOI: 10.2514/6.2012-900.
- [65] J. N. Sørensen and W. Z. Shen, "Numerical Modeling of Wind Turbine Wakes," *Journal of Fluids Engineering*, vol. 124, no. 2, pp. 393–399, May 2002, ISSN: 0098-2202. DOI: 10.1115/1.1471361. eprint: <https://asmedigitalcollection.asme.org/fluidsengineering/article-pdf/124/2/393/5678518/393\1.pdf>. [Online]. Available: <https://doi.org/10.1115/1.1471361>.

- [66] L. Martínez Tossas, S. Leonardi, M. Churchfield, and P. Moriarty, "A comparison of actuator disk and actuator line wind turbine models and best practices for their use," Jan. 2012, ISBN: 978-1-60086-936-5. DOI: 10.2514/6.2012-900.
- [67] R. Mikkelsen, "Actuator disc methods applied to wind turbines," English, Ph.D. dissertation, Jan. 2004, ISBN: 87-7475-296-0.
- [68] R. C. Aster, B. Borchers, and C. H. Thurber, *Parameter estimation and inverse problems*. Elsevier, 2018.
- [69] M. Emory, R. Pecnik, and G. Iaccarino, "Modeling structural uncertainties in reynolds-averaged computations of shock/boundary layer interactions," in *49th AIAA Aerospace Sciences Meeting including the New Horizons Forum and Aerospace Exposition*, 2011, p. 479.
- [70] J.-L. Wu, H. Xiao, R. Sun, and Q. Wang, "RANS equations with explicit data-driven reynolds stress closure can be ill-conditioned," *arXiv preprint arXiv:1803.05581*, 2018.
- [71] J.-X. Wang, J.-L. Wu, and H. Xiao, "Physics-informed machine learning approach for reconstructing reynolds stress modeling discrepancies based on DNS data," *Physical Review Fluids*, vol. 2, no. 3, p. 034603, 2017.
- [72] Y. LeCun, Y. Bengio, and G. Hinton, "Deep learning," *Nature*, vol. 521, no. 7553, pp. 436–444, 2015.
- [73] S. Parneix, D. Laurence, and P. Durbin, "A procedure for using DNS databases," 1998.
- [74] J. P. Huijting, R. P. Dwight, and M. Schmelzer, "Data-driven RANS closures for three-dimensional flows around bluff bodies," *arXiv preprint arXiv:2010.11831*, 2020.
- [75] Z. Hao and C. Górlé, "Quantifying turbulence model uncertainty in reynolds-averaged navier–stokes simulations of a pin-fin array. part 2: Scalar transport," *Computers Fluids*, vol. 209, p. 104642, 2020, ISSN: 0045-7930. DOI: <https://doi.org/10.1016/j.compfluid.2020.104642>. [Online]. Available: <http://www.sciencedirect.com/science/article/pii/S0045793020302140>.
- [76] P. M. Milani, J. Ling, G. Saez-Mischlich, J. Bodart, and J. K. Eaton, "A machine learning approach for determining the turbulent diffusivity in film cooling flows," *Journal of Turbomachinery*, vol. 140, no. 2, 2018.
- [77] R. D. Sandberg, R. Tan, J. Weatheritt, A. Ooi, A. Haghiri, V. Michelassi, and G. Laskowski, "Applying machine learnt explicit algebraic stress and scalar flux models to a fundamental trailing edge slot," *Journal of Turbomachinery*, vol. 140, no. 10, 2018.
- [78] R. J. Beare, M. K. Macvean, A. A. Holtslag, J. Cuxart, I. Esau, J.-C. Golaz, M. A. Jimenez, M. Khairoutdinov, B. Kosovic, D. Lewellen, *et al.*, "An intercomparison of large-eddy simulations of the stable boundary layer," *Boundary-Layer Meteorology*, vol. 118, no. 2, pp. 247–272, 2006.
- [79] M. Abkar and P. Moin, "Large-eddy simulation of thermally stratified atmospheric boundary-layer flow using a minimum dissipation model," *Boundary-layer meteorology*, vol. 165, no. 3, pp. 405–419, 2017.
- [80] J. W. Deardorff, "Stratocumulus-capped mixed layers derived from a three-dimensional model," *Boundary-Layer Meteorology*, vol. 18, no. 4, pp. 495–527, 1980.
- [81] C.-H. Moeng, "A large-eddy-simulation model for the study of planetary boundary-layer turbulence," *Journal of the Atmospheric Sciences*, vol. 41, no. 13, pp. 2052–2062, 1984.
- [82] C.-H. Moeng and J. C. Wyngaard, "Spectral analysis of large-eddy simulations of the convective boundary layer," *Journal of the Atmospheric Sciences*, vol. 45, no. 23, pp. 3573–3587, 1988.
- [83] M. Matthew J. Churchfield, S. Lee, J. Michalakes, and P. J. Moriarty, "A numerical study of the effects of atmospheric and wake turbulence on wind turbine dynamics," *Journal of Turbulence*, vol. 13, N14, 2012. DOI: 10.1080/14685248.2012.668191. eprint: <https://doi.org/10.1080/14685248.2012.668191>. [Online]. Available: <https://doi.org/10.1080/14685248.2012.668191>.
- [84] J. Jonkman, S. Butterfield, W. Musial, and G. Scott, "Definition of a 5-mw reference wind turbine for offshore system development," Feb. 2009. DOI: 10.2172/947422. [Online]. Available: <https://www.osti.gov/biblio/947422>.
- [85] C. L. Archer, S. Mirzaeisefat, and S. Lee, "Quantifying the sensitivity of wind farm performance to array layout options using large-eddy simulation," *Geophysical Research Letters*, vol. 40, no. 18, pp. 4963–4970, 2013. DOI: <https://doi.org/10.1002/grl.50911>. eprint: <https://agupubs.onlinelibrary.wiley.com/doi/pdf/10.1002/grl.50911>. [Online]. Available: <https://agupubs.onlinelibrary.wiley.com/doi/abs/10.1002/grl.50911>.
- [86] P. G. Duynkerke, "Application of the  $\epsilon$ - $\epsilon$  turbulence closure model to the neutral and stable atmospheric boundary layer," *Journal of Atmospheric Sciences*, vol. 45, no. 5, pp. 865–880, 1Mar. 1988. DOI: 10.1175/1520-0469(1988)045<0865:AOTTCM>2.0.CO;2. [Online]. Available: [https://journals.ametsoc.org/view/journals/atsc/45/5/1520-0469\\_1988\\_045\\_0865\\_aottcm\\_2\\_0\\_co\\_2.xml](https://journals.ametsoc.org/view/journals/atsc/45/5/1520-0469_1988_045_0865_aottcm_2_0_co_2.xml).

- [87] J. C. Wyngaard, "Modeling the planetary boundary layer—extension to the stable case," *Boundary-Layer Meteorology*, vol. 9, no. 4, pp. 441–460, 1975.
- [88] T. Koblitz, *CFD Modeling of Non-Neutral Atmospheric Boundary Layer Conditions*. DTU Wind Energy, 2013.
- [89] N. Sørensen, "General purpose flow solver applied to flow over hills," English, Published 2003, Ph.D. dissertation, 1995.
- [90] D. Li, "Turbulent prandtl number in the atmospheric boundary layer-where are we now?" *Atmospheric Research*, vol. 216, pp. 86–105, 2019.
- [91] D. H. Lenschow, J. C. Wyngaard, and W. T. Pennell, "Mean-field and second-moment budgets in a baroclinic, convective boundary layer," *Journal of Atmospheric Sciences*, vol. 37, no. 6, pp. 1313–1326, 1Jun. 1980. DOI: 10.1175/1520-0469(1980)037<1313:MFA SMB>2.0.CO;2. [Online]. Available: [https://journals.ametsoc.org/view/journals/atsc/37/6/1520-0469\\_1980\\_037\\_1313\\_mfasmb\\_2\\_0\\_co\\_2.xml](https://journals.ametsoc.org/view/journals/atsc/37/6/1520-0469_1980_037_1313_mfasmb_2_0_co_2.xml).

# Appendices

## LES Successor Results

## A.1 Neutral Boundary Layer Case

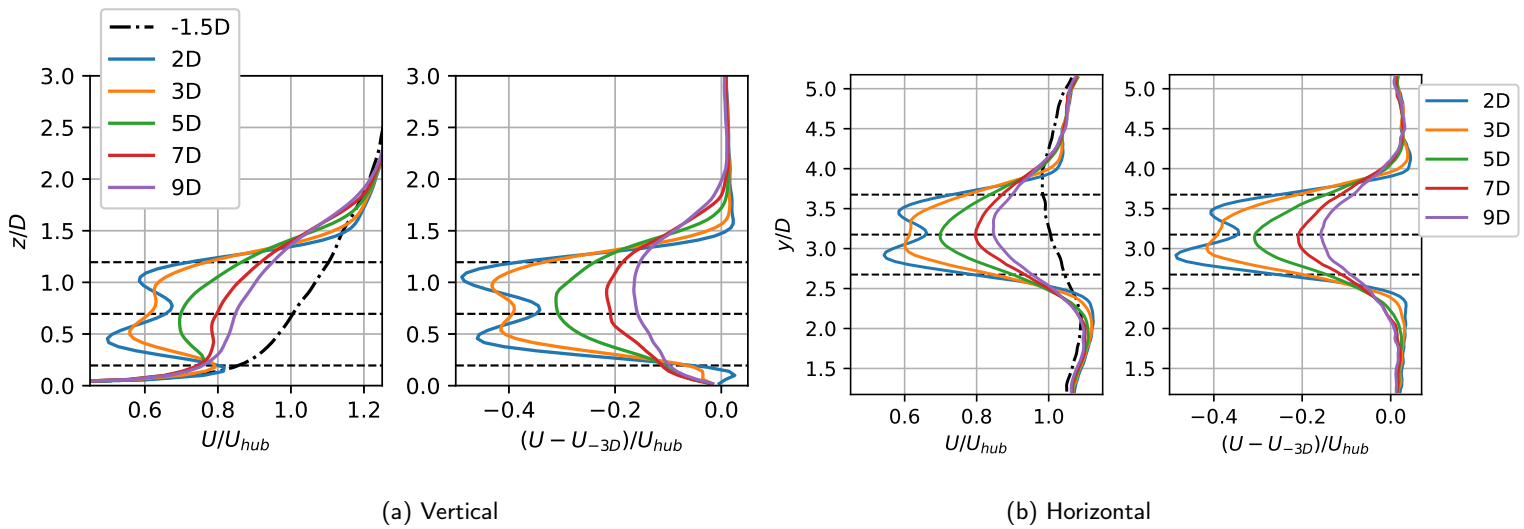


Figure A.1: Neutral boundary layer velocity and velocity deficit profiles in the wake

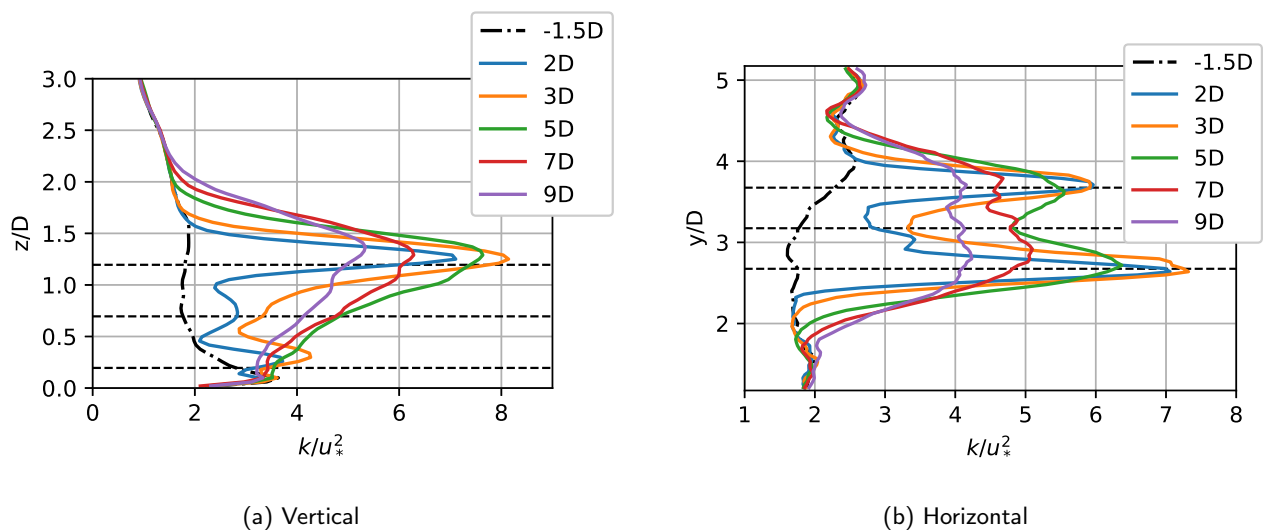


Figure A.2: Neutral boundary layer wake TKE profiles

## A.2 Stable Boundary Layer Case

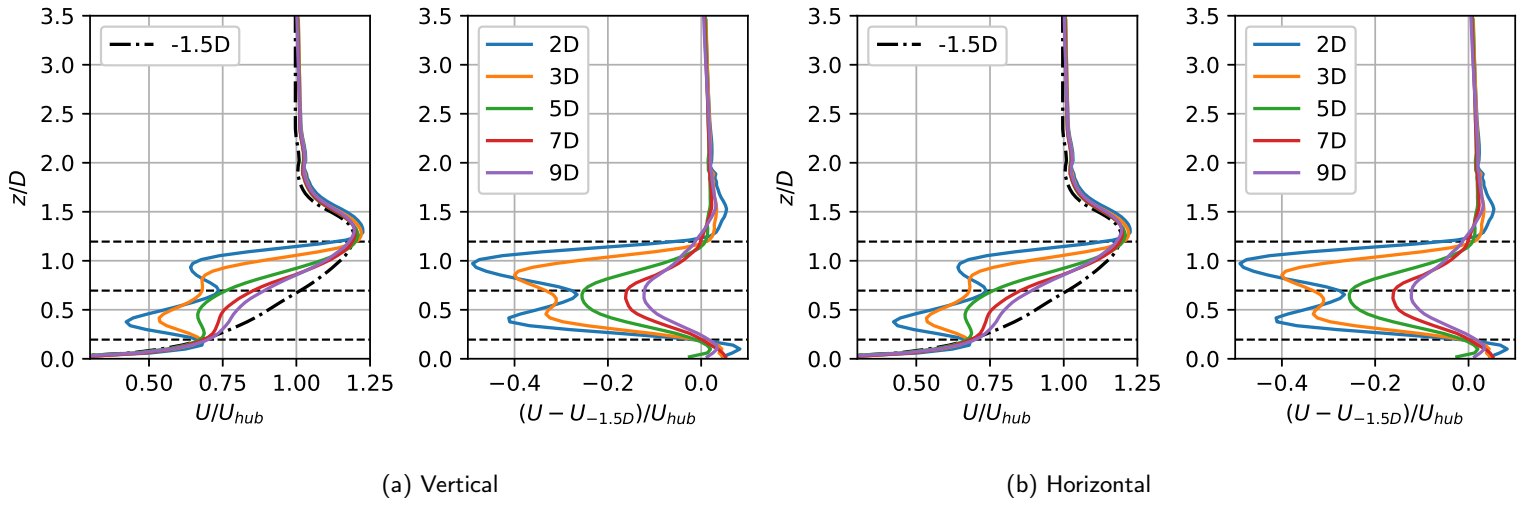


Figure A.3: Stable boundary layer velocity and velocity deficit profiles in the wake

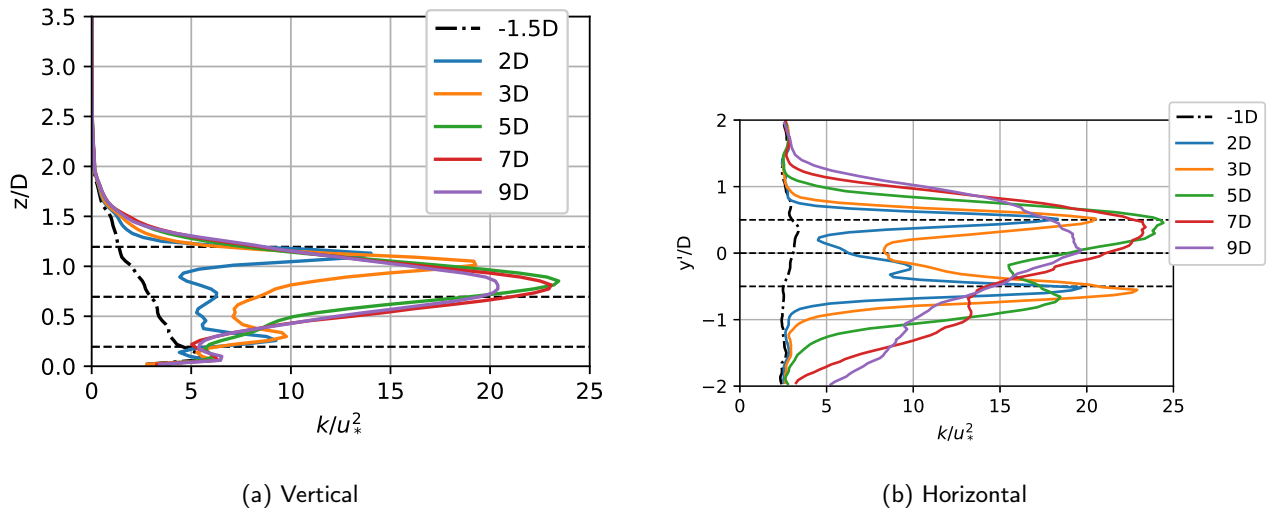


Figure A.4: Stable boundary layer wake TKE profiles

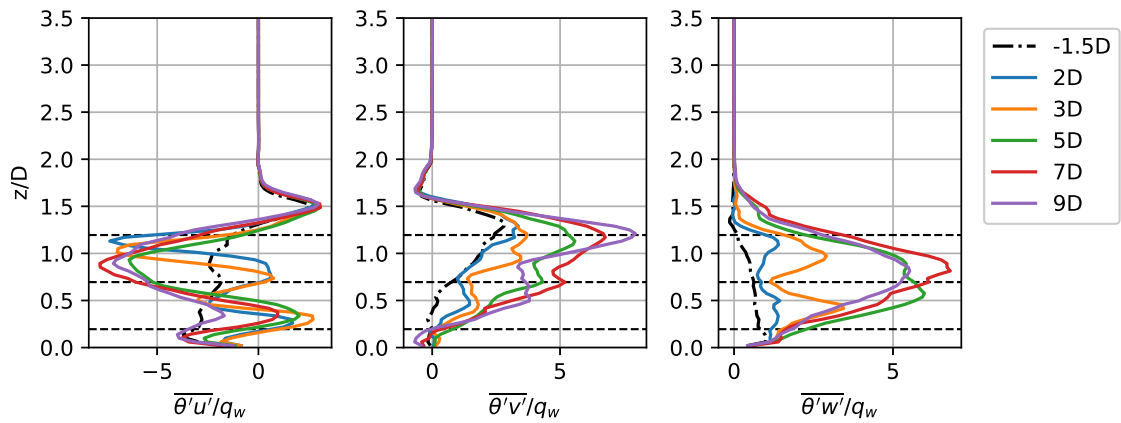


Figure A.5: Stable boundary layer vertical wake heat-flux profiles

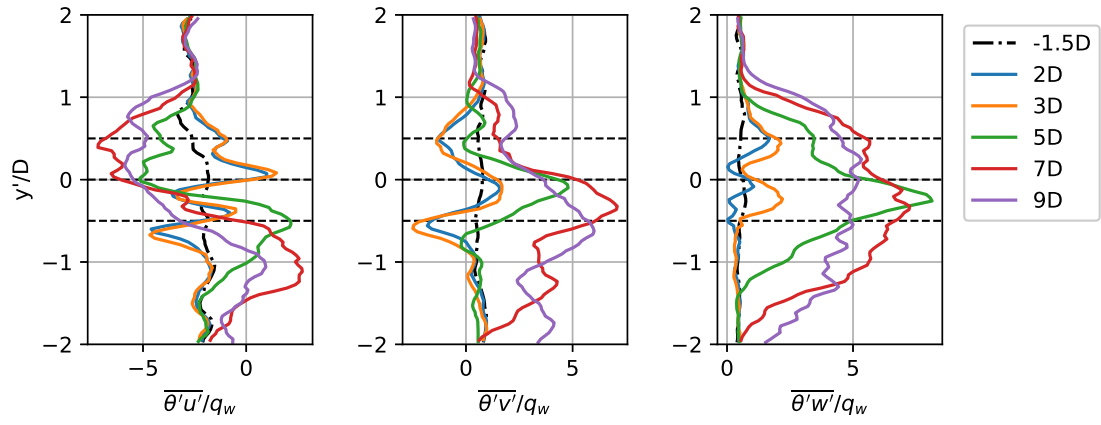


Figure A.6: Stable boundary layer horizontal wake heat-flux profiles

### A.3 Convective Boundary Layer Case

#### A.3.1 Averaging Period 1 Hour

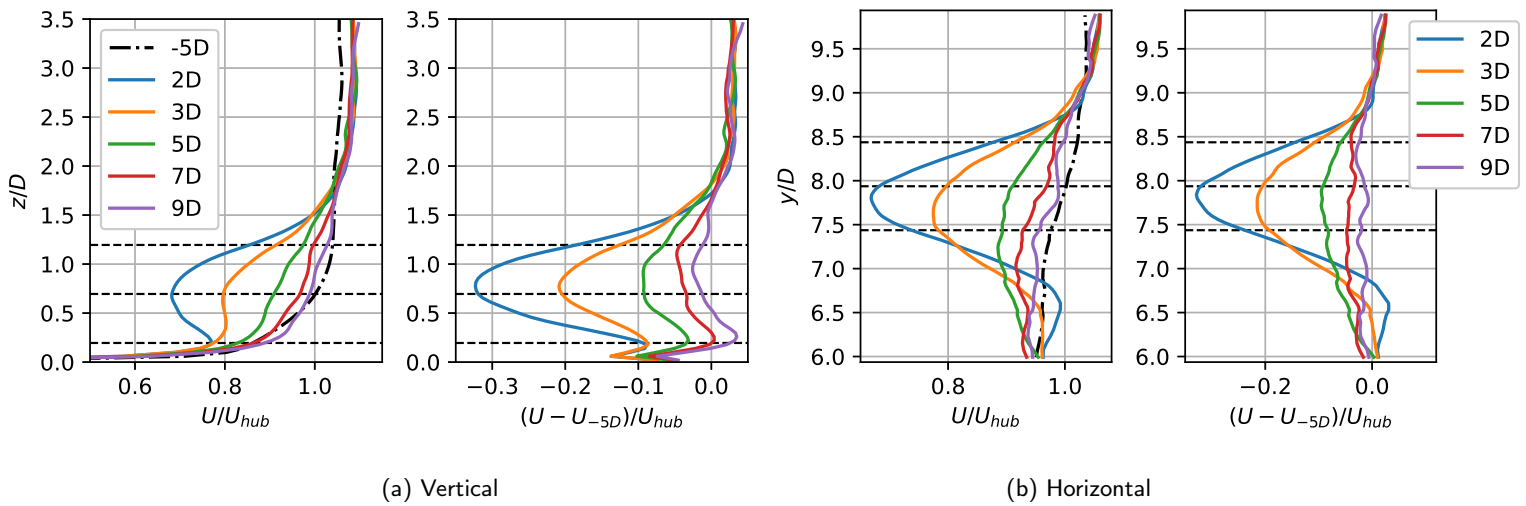


Figure A.7: Convective boundary layer velocity and velocity deficit profiles in the wake obtained with  $T_{avg} = 1 h$

#### A.3.2 Averaging Period 5 Hours

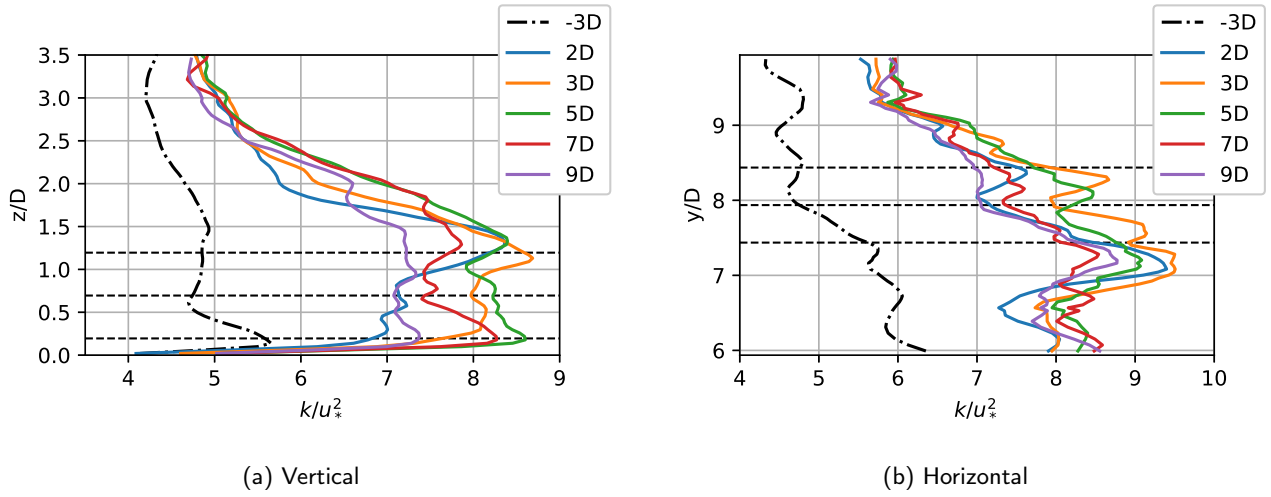


Figure A.8: Convective boundary layer wake TKE profiles obtained with  $T_{avg} = 1 h$

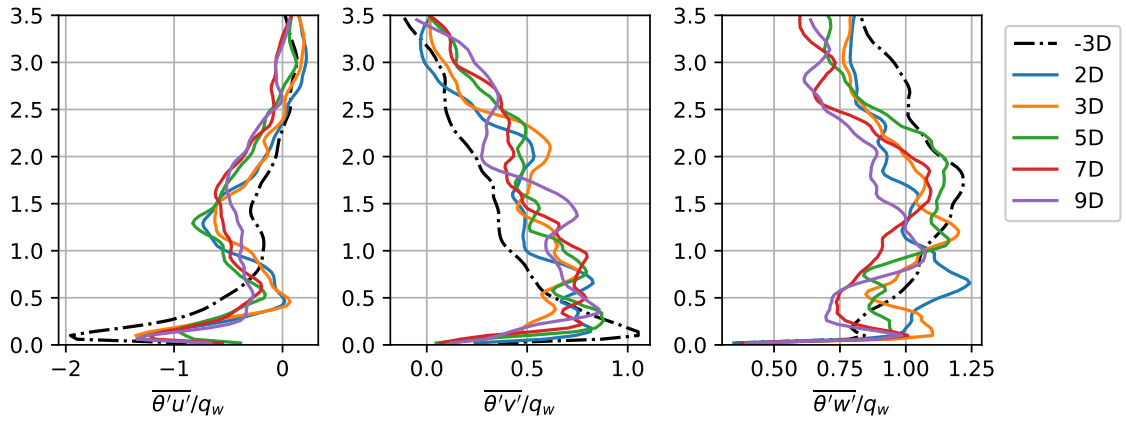


Figure A.9: Convective boundary layer vertical wake heat-flux profiles

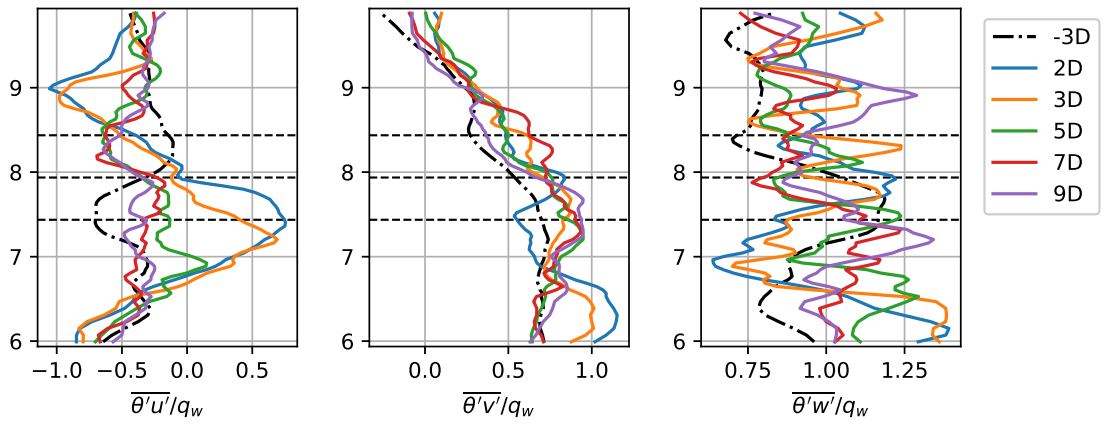


Figure A.10: Convective boundary layer horizontal wake heat-flux profiles obtained with  $T_{avg} = 1 h$

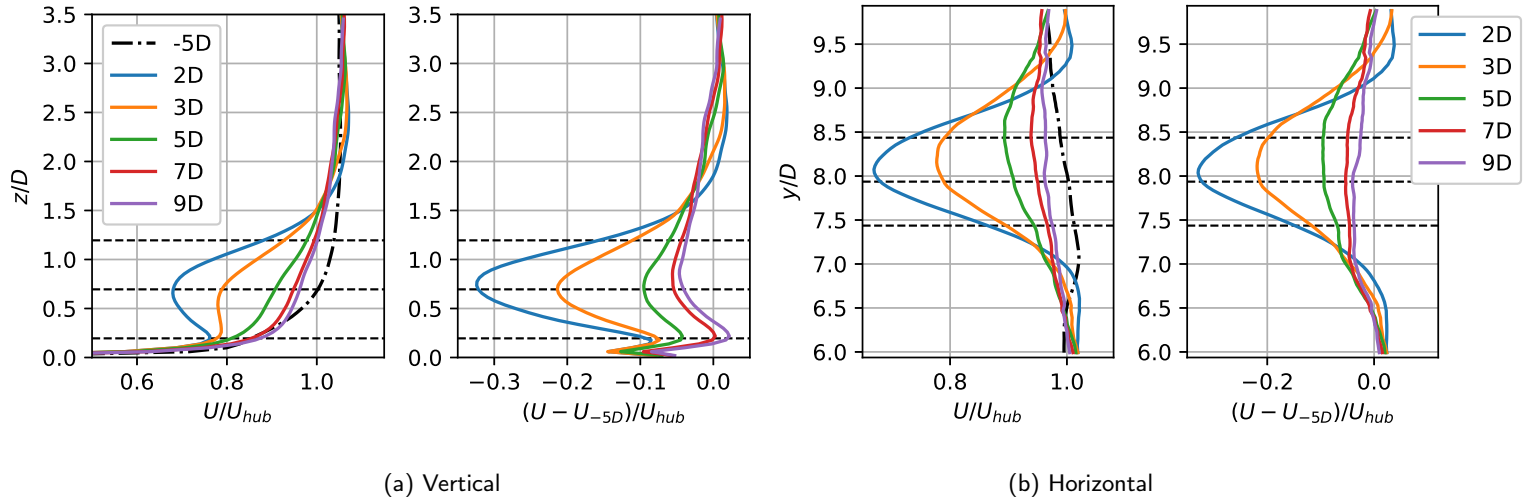


Figure A.11: Convective boundary layer velocity and velocity deficit profiles in the wake obtained with  $T_{avg} = 5 h$

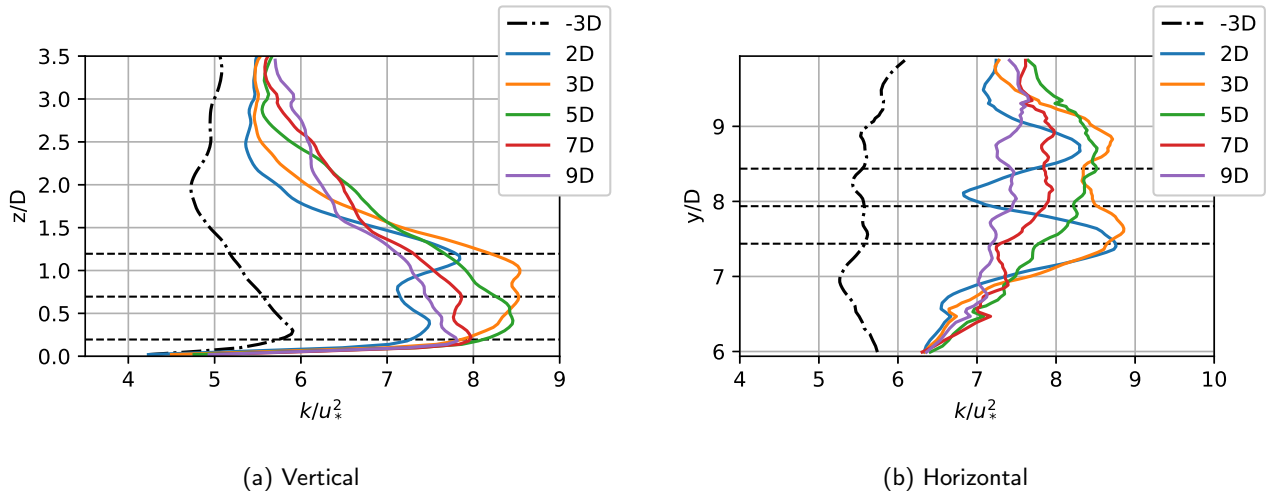


Figure A.12: Convective boundary layer wake TKE profiles obtained with  $T_{avg} = 5 h$

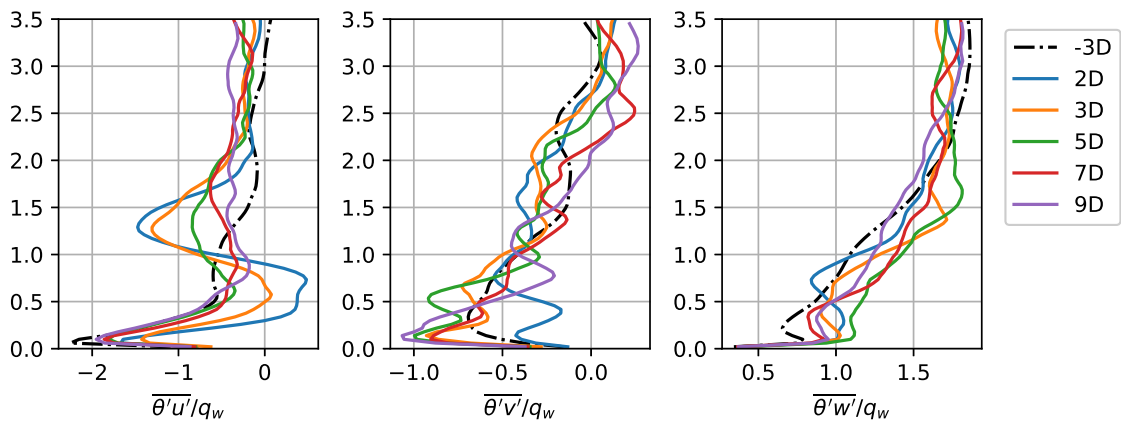


Figure A.13: Convective boundary layer vertical wake heat-flux profiles obtained with  $T_{avg} = 5 h$

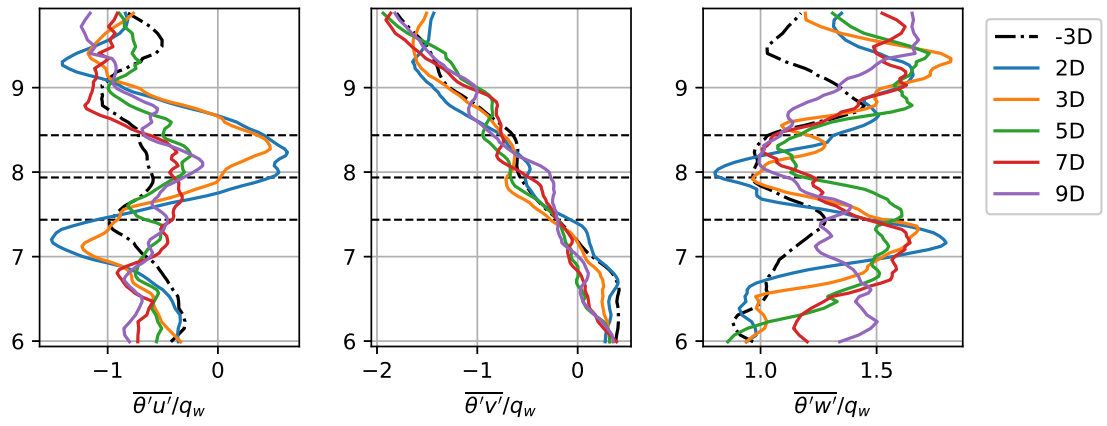


Figure A.14: Convective boundary layer horizontal wake heat-flux profiles obtained with  $T_{avg} = 5 h$